MEASUREMENT AND ANALYSIS OF ELECTRO-OPTICAL MATERIALS AND DEVICES

Parke Mathematical Laboratories, Inc.

J.A. Adamski, A.F. Armington, J.H. Bloom, D.R. Gabbe,
W. Higgins, R.S. Kennedy, J.D. Kierstead, R.A. Martin,
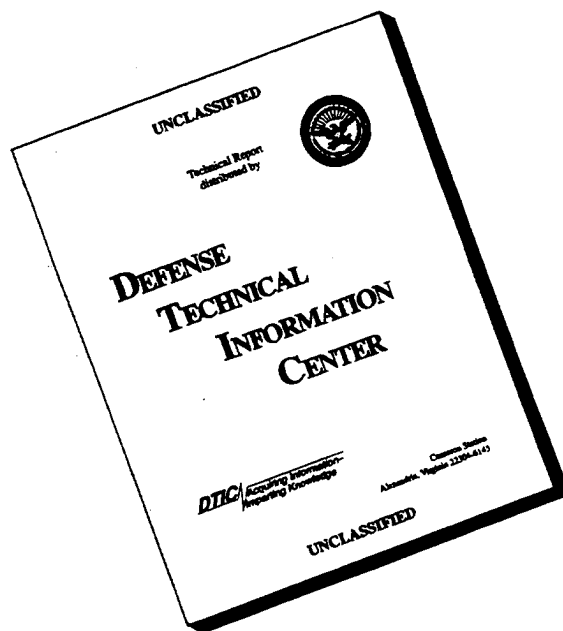T.G. Ryan, P.K. Tedrow, and A. Tripathi

19960807 058

Rome Laboratory
Air Force Materiel Command
Rome, New York

DISCLAIMER NOTICE

UNCLASSIFIED

Technical Report
distributed by

**DEFENSE
TECHNICAL
INFORMATION
CENTER**

DTIC Acquiring Information-
Imparting Knowledge

Cameron Station
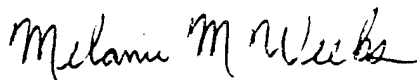Alexandria, Virginia 22304-6145

UNCLASSIFIED

THIS DOCUMENT IS BEST QUALITY AVAILABLE. THE COPY FURNISHED TO DTIC CONTAINED A SIGNIFICANT NUMBER OF PAGES WHICH DO NOT REPRODUCE LEGIBLY.

This report has been reviewed by the Rome Laboratory Public Affairs Office (PA) and is releasable to the National Technical Information Service (NTIS). At NTIS it will be releasable to the general public, including foreign nations.
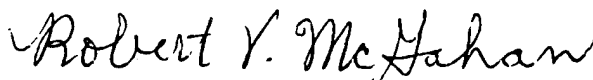
RL-TR-96-67 has been reviewed and is approved for publication.

APPROVED: *Melanie M Weeks*

  MELANIE M. WEEKS
  Project Engineer

FOR THE COMMANDER: *Robert V. McGahan*

  ROBERT V. MCGAHAN
  Director
  Electromagnetics & Reliability Directorate

REPORT DOCUMENTATION PAGE

1. AGENCY USE ONLY (Leave Blank)	2. REPORT DATE April 1996	3. REPORT TYPE AND DATES COVERED Final Jul 90 – Dec 94

4. TITLE AND SUBTITLE MEASUREMENT AND ANALYSIS OF ELECTRO-OPTICAL MATERIALS AND DEVICES	5. FUNDING NUMBERS C – F19628-90-C-0140 PE – 62702F PR – 4600 TA – 19 WU – 64
6. AUTHOR(S) J.A. Adamski, A.F. Armington, J.H. Bloom, D.R. Gabbe, W. Higgins, R.S. Kennedy, J.D. Kierstead, R.A. Martin, T.G. Ryan, P.K. Tedrow, and A. Tripathi	

7. PERFORMING ORGANIZATION NAME(S) AND ADDRESS(ES) Parke Mathematical Laboratories, Inc. 175 Cabot Street Lowell MA 01854	8. PERFORMING ORGANIZATION REPORT NUMBER N/A

9. SPONSORING/MONITORING AGENCY NAME(S) AND ADDRESS(ES) Rome Laboratory/ERED 80 Scott Rd Hanscom AFB MA 01731-2909	10. SPONSORING/MONITORING AGENCY REPORT NUMBER RL-TR-96-67

11. SUPPLEMENTARY NOTES

Rome Laboratory Project Engineer: Melanie M. Weeks/ERED/(617) 377-5122

12a. DISTRIBUTION/AVAILABILITY STATEMENT Approved for public release; distribution unlimited.	12b. DISTRIBUTION CODE

13. ABSTRACT (Maximum 200 words)

A description is given of the research and experimental work accomplished on the injection of phosphorus into an indium melt. Two crystal growing techniques were used to produce single crystals of InP. Three little used crystal growth techniques are discussed for growing nonlinear optical materials. Device processing techniques covering the use of an ultra high vacuum deposition system for evaporating a dielectric layer of silicon monoxide is described. Nonlinear materials have been studied for applications in optical computing and optical signal processing. Photorefractive and resonant nonlinear optical interactions have been studied, and are described regarding crystal fields in solids and collisions in vapors. Also, the nonlinear optical properties of an atomic beam were studied and researched. Work was completed regarding the redesign of a video board to shrink the entire electronics package for the B52 FLIR camera project. Details are given concerning equipment used in a research program to obtain zero reflection using a single or multi-layer coating of SiN on the surface of a GaAlAs side emitting laser diode.

14. SUBJECT TERMS Indium phosphide, Gel growth, Infrared detector, Electro-optic substrates, Single crystal, Optical signal processing, Silicides, Anti-reflective coating			15. NUMBER OF PAGES 186
			16. PRICE CODE

17. SECURITY CLASSIFICATION OF REPORT UNCLASSIFIED	18. SECURITY CLASSIFICATION OF THIS PAGE UNCLASSIFIED	19. SECURITY CLASSIFICATION OF ABSTRACT UNCLASSIFIED	20. LIMITATION OF ABSTRACT UL

TABLE OF CONTENTS

FORWARD

This report is the Final Scientific Report for Contract F19628-90-C-0140 covering the period of July 1, 1990 through December 30, 1994.

The following individuals have contributed to research results reported on this report.

Joseph A. Adamski	- Parke Mathematical Laboratories, Inc. (PML)
Alton F. Armington	- Consultant to PML
Jerome H. Bloom	- Consultant to PML
David R. Gabbe	- Consultant to PML
William Higgins	- Consultant to PML
Robert S. Kennedy	- Consultant to PML
John D. Kierstead	- Consultant to PML
Robert A. Martin	- Consultant to PML
Thomas G. Ryan	- Consultant to PML
Prabha Tedrow	- Consultant to PML
Alok Tripathi	- Consultant to PML

PREFACE

This work is composed of eleven sections. It provides a summary of work accomplished under the contract in several diverse areas of optical transmission and solid state material processing.

I.   A description is given of the research and experimental program on the injection of phosphorus into an indium melt to produce the compound InP. Details are given on a process to grow single crystals of this material in a one step process. The two phase process for the synthesis and single crystal growth of InP grown in a magentic field using both the Czochralski and Kyropoulos techniques is given.

II. Three little used crystal growth techniques were investigated for the growth of non-linear optical (NLO) materials which cannot be simply grown from the melt techniques. They were gel growth (borate materials), chemical vapor transportation (bismuth silicate and tantalate, barium borate, and KTN), and hydrothermal crystal growth (bismuth silicate and barium borate).

III. Device processing techniques covering the use of an ultra high vacuum deposition system for evaporating a dielectric layer of silicon is described. This section also includes a discussion on the use of an ion beam implanter for forming special buried layers on silicon devices. The extreme usefulness of a residual gas analyzer to determine gas species within the vacuum chamber is shown.

IV. Methods for repeatable in-situ phosphorus injection synthesis of indium phosphide melts that have a phosphorus content close to 50 mol% were developed. Crystal growth conditions were optimized to reduce the incidence of twinning. A new seeding technique was introduced to stabilize the initial crystal growth conditions.

V.   Experiments to improve the MLEK process performance for InP growth were made. Key parts of the crcystal growth system were upgraded to improve system performance. Experiments were made to synthesize $ZnGeP_2$ by the P injection process, and to grow $ZnGeP_2$ crystals by the CVT process.

VI. Communication security has been researched in fiber optic communication systems (IROCS) by ensuring that any undetected intrusion will deliver so little power to a potential intruder that no useful information can be extracted from it. Work during this time has been concerned with determining the user performance in intrusion resistance that can be achieved using the modulation/coding method.

VII. Photorefractive and resonant nonlinear interactions were studied. Resonant interactions are the most promising, but have been difficult to study in detail because of broadcasting mechanisms that are present in most materials; for example, crystal fields in solids and collisions in vapors. To eliminate the complications, the nonlinear optical properties of an atomic beam were studied and investigated.

VIII. Efforts during this time were devoted to the redesign of the B52 Camera video board. The redesign was planned as part of the next phase of the B52 FLIR camera project which is essentially a system shrink of the entire electronics package. The video board was redesigned to utilize fewer components to improve the performance and simplify packaging the board into a smaller space with a new form factor. A special effort was made to have a working prototype completed by the beginning of December, 1990 using the current board dimensions (form Factor) for implementation in the existing prototype camera.

IX. Research was accomplished to reduce reflection that occurs at the interface between two optical media. The object of this work was to obtain zero reflection using either a single or multi-layer coating on the surface of the GaAlAs side emitting laser diode. Details are given regarding the equipment used for this program along with problems that developed during experimentation.

X. Considerable progress was made in the device fabrication process in the area of semiconductor processing (Si and SiGe) to fabricate infrared detectors using Schottky and HIP technologies. New substrate holders and spin-drying chucks were designed and fabricated. Use of these new fixtures resulted in reducing the consumption of chemicals in the wafer cleaning process.

XI. The general subject of the program under this contract was that of development of new, or adapt existing technologies at RL/ERE's facilities for the oxidation, photolithography, mask layout, metal deposition (e.g. Pt, Ir), and characterization of Silicide/Si (e.g. PtSi and IrSi), and Si_xGe_{1-x}/Si based infrared detectors.

INTRODUCTION

Direct synthesis of phosphorus into indium to achieve stoichiometric melts of indium phosphide requires an understanding of the equilibrium vapor pressures of the various allotropic forms of phosphorus as well as a furnace designed to exploit the rate of reaction between indium and phosphorus. Experimental procedures were designed, developed, and accomplished in an attempt to control the red phosphorus being injected into the indium melt for in-situ synthesis and single crystal growth of InP. The phosphorus pressure inside the injector is controlled by the temperature at the coldest point, near the top of the injector. The rate of injection is controlled by the pressure difference between the ambient gas and the internal phosphorus pressure. If too rapid, the phosphorus will bubble out of the indium instead of reacting with the melt. If the pressure is too low, the injector will never achieve a stoichiometric compound.

We have measured the temperature inside the phosphorus injector under a variety of conditions, and compared our data to the extensive literature on phosphorus vapor pressure. We have optimized the injector process in order to reproducibly synthesize a stoichiometric InP melt.

During this reporting period, eighty (80) experimental runs were made to grow single crystals of InP. Of these, thirty seven (37) were phosphorus injected (in-situ) and thirty (30) were from previous injected charges that were either polycrystalline or twinned crystals. Also, in an attempt to grow semi-insulating indium phosphide, fourteen (14) runs were doped with iron (Fe).

As of 1 July 1991, all injections and crystal growth of InP was accomplished using redesigned components/furniture to grow 3" diameter crystals. No serious problems were encountered regarding performance of the system components. However, it was discovered that the pulling mechanism of the system was in need of repair. It was found that the upper and lower thrust bearings were worn, and the threaded bearing for the lead screw needed to be replaced. These worn parts caused the Teflon (used as a lubricant) on the lead screw to grind off due to misalignment of the pulling platform. This also caused vibrations in the pull shaft which contributed to our inability to grow single crystals. Since the puller has been repaired, several single crystals have been grown. Figure I-1 is a photograph of an InP crystal during growth which shows four pole symmetry that indicates the <100> crystallographic growth direction and is twin free. Also during this time, a newly designed phosphorus injector was fabricated and put into practice.

Three (3) excellent crystals were grown using previously phosphorus injected charges. Two (2) crystals were grown in the <100> direction and weighed 883 gms and 712 gms respectively. Both crystals were approximately 2.75 inches in diameter and 2.50 inches long. One crystal was grown in the <111> direction, weighed approximately 805 gms, was 2.75 inches in diameter by 2.75 inches long. Figure I-2 shows three twin-free <100> InP crystals grown by the MLEK technique.

Experiments were designed to develop a basic understanding of the thermal response of high pressure crystal growth experiments, and to measure temperature at several locations in the HP chamber under various process conditions, particularly before and during the in-situ synthesis of indium phosphide. Also, we are vacuum baking the red phosphorus to remove the water vapor that might be present.

Time was spent preparing manuscripts with tables, photographs, and graphs for presentations that were published and given at the Fourth International Conference on Indium Phosphide and Related Materials (Newport, RI). The title of the paper and oral presentation was "In-Situ Synthesis and Crystal Growth of InP." This conference was sponsored by the IEEE Lasers and Optic Society, and the IEEE Electron Device Society. A second manuscript with graphs, photographs, and tables was prepared and published in the Journal of Crystal Growth in October 1992. The title of the paper was "MLEK Crystal Growth of Large Diameter <100> Indium Phosphide." Also, an oral presentation (same title) was given at the 10th International Conference on Crystal Growth at the Sheraton Harbor Hotel in San Diego, CA. The authors of the two technical papers and oral presentations were Mr. David F. Bliss and Mr. Robert M. Hilton of RL/ERX and Mr. Joseph A. Adamski of Parke Mathematical Laboratories, Inc., Lowell, MA. The oral presentations were given by Mr. Joseph A. Adamski and Mr. David F. Bliss respectively.

All the work done during this period (29 June 1990 through 30 September 1992) was in close collaboration with Mr. David F. Bliss and Mr. Robert M. Hilton of RL/ERX.

EXPERIMENTAL

One of the goals in this in-situ synthesis/growth InP program is to achieve stoichiometric charges by injecting phosphorus into an indium melt and then growing single crystals from it. Temperature and overpressure are the main variables. Phosphorus must reach a critical temperature, the vapor pressure inside the injector has to be sufficient to overcome the N_2 pressure inside the furnace. If the vapor pressure inside the injector isn't high enough, the N_2 overpressure (600 psi) over the melt will force the liquid InP into the discharge tube, causing it to explode.

The injector is radiatively heated by the charged crucible, and the top and sides are insulated to prevent heat from radiating out. If the top of the injector is too cool, this will cause the phosphorus to condense, thus preventing the vapor from entering the liquid indium to form InP. To prevent phosphorus loss during injection/crystal growth, B_2O_3 is used as an encapsulate and the pressure inside the furnace is raised to 600 psi.

Injecting phosphorus into the indium has recently become routine. A few explosions have occurred but the InP crystals grown using this one step process have been of very good quality.

7

An experiment was conducted in an attempt to profile the temperature inside the injector using three thermocouples. A quartz crucible filled with InP from a previous run was used and encapsulated with the usual amount of B_2O_3. The injector was filled with a non-volatile oxide which was substituted for the red phosphorus. Figure I-3 is a schematic showing the placement of these thermocouples within the injector and sealed off from the phosphorus. The thermocouples were attached to a chart recorder. This enabled us to monitor the temperature of the phosphorus, thus we know the approximate phosphorus pressure. Previous to this, only one thermocouple was used (at the top) and the temperature at the bottom of the injector was unknown. The schematic also shows the position of the thermocouple well, quartz shield, insulation and the flow direction of the P_4 (gas) into the indium melt.

Figure I-4 shows the temperature profile of the injector at two different positions and Figure I-5 is a graph showing the rate of temperature rise inside the phosphorus injector. By raising the apparatus 2 cm above the crucible bottom, a new equilibrium was obtained.

Based on the preliminary data, it's rather apparent that the red phosphorus goes into solution (mp 600°C) at the bottom of the injector. This could cause a tremendous final pressure, creating bubbles in the InP melt, thus pushing these bubbles into the molten B_2O_3. Whenever bubbles are trapped in the B_2O_3, the InP crystals are prone to twining.

Now that we have a means of monitoring the injector temperature, it should be possible to control the pressure. This will prevent bubbles from forming in the B_2O_3 and pushing phosphorus vapors out of the melt. It is hoped that the charge will be stoichiometric (and possibly P-rich) and all grown crystals will be single. It is very important to achieve the one step in-situ synthesis/growth, as this technique yields pure materials and will produce inexpensive, high quality substrates for both optical and high speed devices. As stated by Inada and Fukuda[1], the reason for the high cost of InP substrates is that the crystals are usually grown by a "two step process".

Several InP in-situ crystals were grown (Bliss, et. al.[2]) using indium metal from three different suppliers. This was done to establish which vendors' material would produce the purest crystals. After growth, these crystals were sent to Northern Analytical Labs, Inc.[3] for characterization to establish the concentration of impurity elements. Figure I-6 is a bar graph that shows these impurity levels for eight different elements in atoms/cm^3.

[1]   T. Inada & T. Fukuda, Indium Phosphide: Crystal Growth and Characterization. Ed. Willardson, R.K., and Beer, A.C., Academic Press, NY. 1990, Chapter 3 pp 71-73.
[2]   Bliss, D.F., Hilton, R.M., Bachowski, S.S. and Adamski, J.A., MLEK Crystal Growth of (100) Indium Phosphide, Journal of Electronic Materials, Vol. 20, No. 12, 1991.
[3]   Northern Analytical Labs., Inc., 23 Depot Street, Merrimack, NH.

The Kyropoulos[4] method has been adapted to indium phosphide growth in the (100) direction making use of a magnetic field to increase the radial temperature gradient. The axial magnetic field also creates a more stable environment for crystal growth by reducing turbulence in the melt. Combining magnetic liquid encapsulated Kyropoulos (MLEK) with magnetic liquid encapsulated Czochralski[5] (MLEC), a crystal was grown with a flat top roughly two inches or larger in diameter, and then slowly pulled as a cylinder 60 mm in length. A top view of a (100) InP crystal grown by this technique is shown in Figure I-7. We have measured the aspect ratio of the solid-liquid interface from growth striations viewed with a near infrared imaging technique, and compared the dislocation density of this material with standard LEC grown InP (See Characterization Section).

A non-magnetic stainless steel chamber Figure I-8 contains the graphite hot zone, powered by an RF generator and coil. Outside the chamber a large torroidal magnet provides an axial magnetic field up to 4 kilo gauss at the center of the hot zone. Fused quartz crucibles are used to contain a 400-800 gram charge of indium. The indium is placed in the furnace along with 80 grams of dry boron oxide. The furnace is evacuated and pressurized with 600 psi N_2. Once melted, the injector is lowered through the B_2O_3 and the red phosphorous is allowed to discharge into the melt. A <100> seed 6 mm square is dipped into the melt. Seed rotation at 4 rpm and a 2000 gauss axial magnetic field is employed. A two inch flat crown is grown over a 60 minute period by increasing the water flow through the seed holder and decreasing the RF power; no pulling is employed during this initial period. A high intensity light shining through one of the furnace windows reflects an image of the crystal top to the CCD camera (Dage MTI). Twins are easily detected by viewing the reflected light off the flat crystal crown. When a twin is detected, the crystal is melted and a new crystal is grown. Viewing this specular surface, it is easier to detect twins than on the convex surface of LEC crystals. In this fashion twin free crystals can be repeatably grown. After the crown is formed the pull rate is set at 12 mm/hr and the crystal is pulled to completion.

Recently, a decision was made to grow three (3) inch diameter InP crystals. Considerable time was spent with Mr. David F. Bliss and Mr. Robert M. Hilton to scale up the apparatus so larger diameter crystals could be grown. The following components had to be redesigned to accomplish this mission:

(a) R.F. coil
(b) Heat shields
(c) Susceptor
(d) Crucible
(e) Injector
(f) Insulated Injector Dome

---

[4] Kryopoulos, S., Z. anorg. Chem. 154 (1926) 308.
[5] Czochralski, J.Z., Physik, Chem. (Leipzig) 92, 219 (1917).

In redesigning all the components, it was decided not to change the configuration of these parts used to grow the two (2) inch diameter InP crystals. After several weeks, the scale up was completed and all the components were installed in the crystal growing chamber.

After installation, previously grown InP pieces were etched in a Bromine/Methanol solution, put in a four (4) inch diameter quartz crucible and placed inside the furnace chamber. The InP charge weighed approximately 973 grams and 200 grams of B_2O_3 was placed on top as an encapsulant. The furnace chamber was closed and the system was under vacuum over night. The following day the chamber was pressurized using nitrogen. The R.F. generator was turned on and we proceeded to melt the B_2O_3 encapsulant and then InP. By increasing the size of the R.F. coil and the other furnace components, the generator had to be re-tuned as there was a mismatch with the load. Fortunately, we were able to tune the generator by changing the Grid control setting. In about one (1) hour, the B_2O_3 and the InP charge all went into solution and the system was turned off. The following day the charge was removed from the furnace chamber and examined. The InP pieces had completely gone into solution so it was decided to attempt to grow a crystal using this solid charge.

Two (2) crystals were grown. The first crystal grown was 2 7/8" diameter by 3" long and the second crystal (Figure I-9) which was Fe doped was 3" diameter by 2.625" long. This second crystal was approximately 95% single. Based on these early experiments, our scaled up components and the R.F. coil used to grow 3" diameter InP crystals was successful.

A new addition made to the crystal growing apparatus was to install a Video Camera on one of the viewing ports. Figure (I-8) shows the position of this apparatus which allows the crystal grower to view the progress of the growing crystal on a video monitor. This is an important safety feature that was needed for sometime, as the internal pressure in the crystal growing chamber varies anywhere from 500 to 600 psi during the growth process. Previous to this the crystal grower had to view the crystal growing by looking directly into the view port on the apparatus.

Time was spent with Mr. David F. Bliss and Mr. Robert M. Hilton of RL/ERX to design a new phosphorus injector/dome apparatus that will permit us to inject P into In and keep a quartz dome over the melt. Since using a dome over the melt, viewing the crystal during growth with 600 psi over pressure of N_2 gas has improved dramatically. Also, this dome appears to keep the B_2O_3 encapsulant hotter, therefore the viscosity is thinner. With the present injector configuration, we were unable to use the dome during injections because of dimensional restrictions inside the furnace chamber. With the new apparatus, the injector will use the pull shaft as a guide, which will keep it in the center of the furnace chamber.

The matching dome is placed inside the furnace, the injector rides down on the pull shaft and goes inside the dome. This dome stops the convection current caused

10

by the N$_2$ gas (600 psi) and keeps the B$_2$O$_3$ encapsulant/InP interface free of temperature fluctuations that can cause twinning during crystal growth.

When using the present injector, after the phosphorus injection is completed, it had to be pulled out of the melt and then turned to the side of the furnace chamber, thus, taking up space which interfered with the dome. Because of the lack of interior furnace space, it is not possible to see both components at the same time. The dome could only be used if we grow a crystal from a previously injected experiment.

A prototype apparatus was fabricated from Pyrex so that experiments, physical measurements, placement and design changes required could be studied before the apparatus was fabricated from quartz and tested in the high pressure furnace. For our first test, we injected 200 grams of phosphorus into 800 grams of indium which produced an InP single crystal approximately 3.0 inches in diameter by 2.75 inches long (850 grams).

Several experiments were completed using the new injector and dome but due to the poor workmanship in fabricating the injector, we could not complete the entire in-situ operation. The injection of phosphorus into the indium went well and was very rapid as expected. Because of thinned out areas in the quartz (from being blown), one injector exploded as it could not withstand the internal high phosphorus pressure. We are looking into having another glassblower fabricate this injector in hopes that it can be constructed properly and eliminate the thinned out walls of the assembly during fabrication. The newly designed injector needs a few minor changes, new graphite susceptors have been designed and fabricated. Also several experiments will be done using PBN crucibles in an attempt to grow higher purity InP single crystals.

A PBN crucible was used for the first time in an attempt to grow higher purity InP crystals. Phosphorus was injected into the molten indium using the RL/ERX standard injector. It is hoped that by using PBN, the silicon content in the grown crystal will be lower.

Three injection experiments were successful and <1-1-1> oriented seeds were used to initiate crystal growth. Of these three experiments, only one was successful in producing a crystal and was very near stoichiometry ($\approx$ 49^m/o P). The other two experiments did not produce a crystal as we had problems trying to establish a temperature gradient at the growth interface. Using PBN crucibles in place of quartz, presented a problem as PBN is more of an insulating material than quartz. Also, we studied the position of the crucible in the heat zone to establish where the proper location of the growth interface should be in regards to the thermal gradient. All indium charges using PBN crucibles were approximately 500 grams. Presently, we do not have any data regarding the purity of the InP crystals using PBN vs. Quartz.

Three experiments were run using quartz crucibles with an indium charge of approximately 800 grams. One run was completed using the standard RL/ERX injector

and a crystal approximately 3" in diameter was grown weighing 743 grams. The new injector was used for two other experiments and the injection of P into molten indium was successful. However, two experiments had to be aborted because we could not establish a proper temperature gradient at the melt interface. Because of the new injector design there is very little radial and vertical heat loss. We find that the melt is much hotter, therefore new temperature settings on our power supply and controller must be established. Also, the injection time is faster and the phosphorus does not diffuse into the indium fast enough. When this happens, a lot of smoke develops and we had to abort the second experiment. Our viewing ports were covered with soot and we could not see the melt and seed to initiate crystal growth.

No further experimental work was accomplished as several problems occurred. The first situation that we encountered was the furnace could not be operated for two (2) weeks because one of the pumps on the chilled water supply burned out. The second problem was that a water leak developed inside the crystal growing chamber. The furnace system was dismantled twice before we successfully re-welded a cracked seam at the bottom of the main crystal growth chamber.

A series of experiments were performed in order to develop a basic understanding of the thermal response of high pressure crystal growth equipment and to measure temperature at several locations in the HP chamber under various process conditions, particularly before and during the in-situ synthesis of indium-phosphide. During the first experiment, with a thermocouple probe attached to the cold seed shaft (Figure I-10) was dipped into the B_2O_3 encapsulated In melt, it was observed that a large temperature gradient existed across the B_2O_3 and melt layers, 200°C and 80°C temperature difference across 10 mm B_2O_3 and 25 mm In melt, respectively. This large temperature drop was caused by a strong convection current produced by the buoyant flows in the HPCG chamber. The cold N_2 gas was flowing downward along the cold seed shaft and the T/C probe. This run emphasized the need for isolating the primary gas flow (downward along the chamber wall) from the buoyant flow in the proximity of the melt and P-injector, by a quartz heat shield. Another important observation made during this run was that the temperature of the melt increased almost linearly with the power input to R.F. coil and about 10 minutes time was required for the melt temperature to stabilize for a step increase in supply voltage by 0.2kV.

During the later runs, thermocouples were placed at four different (Figure I-11) locations -- directly underneath the crucible bottom, at the P-injector tube tip, and at the injector top and bottom surfaces. A direct relationship between melt temperature and power input was reaffirmed. The heat shield reduced the strength of convective gas flows in the melt region, and the upward flow along the crucible was observed to be weaker. The flow strength, however, increased with the melt temperature. The thermocouple readings showed a strong radiation coupling between the melt and the injector bottom temperatures on the injector bottom and tube tip and a somewhat slower increase in temperature of the melt, it was evident that the radiation plays the most significant role in transferring energy from the melt to phosphorus for its vaporization.

12

A simple heat transfer model indicates that depending on its temperature, a 4" diameter melt surface looses 1.4 to 2 kW of energy of which only 10-25% is lost by convection to nitrogen gas. A strong impact of radiation was further observed during the run in which phosphorus vapor leaked out from the injector and produced a dark, thick cloud over the melt, thereby reducing the radiation loss substantially. The temperature of the melt increased by more than 300°C within minutes.

These experiments also indicated that the temperature of the top of the injector usually remains very low which is not desirable from in-situ synthesis consideration. Secondly, the nitrogen inside the phosphorus ampoule takes 20-25 minutes to expand and leak through the injection tube. This is primarily because there exists a large temperature difference between the top and bottom surfaces of the injector, and the gas in the injector receives most of the energy for its expansion by conduction which is a slow process. Evidently, the injector design needs to be modified such that more energy can reach its upper portion. This will also reduce condensation of P-vapor in the upper portion of the ampoule during the initial period of sublimination/boiling.

Another observation made during these runs was that the phosphorus vapor pressure build-up in the ampoule was very high when the injector tube was dipped into the indium melt for synthesis. This is mainly because the radiation view factor between the melt and the chamber (cold) wall decreases significantly when the injector is brought to its bottom most position, thereby increasing the heat transfer to phosphorus substantially. In fact, the injector may be receiving 0.5-0.8 kW of energy in its bottom position, compared to about 0.1 kW in its top position. A proper distribution of heat along the entire injector, a reduction in heat loss from the top of the injector and a fast transfer of P-vapor from its ampoule to the melt by providing two transfer tubes may help in producing desirable conditions for in-situ synthesis of indium phosphide. An injector was designed and fabricated utilizing two transfer tubes and found that it had no advantage over the single transfer tube design.

All experiments performed were in close collaboration with Mr. David F. Bliss and Mr. Robert M. Hilton of RL/ERX. Professor V. Prasad of the Department of Mechanical Engineering at Columbia University, New York (who spent several weeks at RL/ERX) was the main thrust behind these experiments. All the data that he and others have collected will be used to construct a theoretical model of the RL/ERX high pressure crystal grower which will give an insight to the physical changes that can be made to improve the in-situ procedure. When all this work has been completed and changes made to the crystal grower, it is anticipated that the in-situ process to produce high quality single crystals of InP will be routine. A technical paper to the Journal of Crystal Growth was published regarding this work.[6]

[6] V. Prasad[a], D.F. Bliss[b], J.A. Adamski[c] - "Thermal Characterization of the High Pressure Crystal Growth System for In-situ Synthesis and Growth of InP Crystals."
      a. Department of Mechanical Engineering, State Univ. of New York, Stony Brook, NY 11794
      b. U.S. Air Force, Rome Laboratory, Hanscom AFB, MA 01731
      c. Parke Mathematical Laboratories, Inc., 175 Cabot Street, Lowell, MA 01854
Journal of Crystal Growth 142 (1994) 21-30.

A series of eight (8) experiments were performed using the new phosphorus injector with the side transfer tube. Four experiments produced successful phosphorus injections into the molten indium, but some smoking occurred which hampered visibility and several crystals could not be grown. One run was aborted because the RF coil arched and the RF generator had to be turned off. Another run had to be shut down because the phosphorus injector exploded after injection. Two crystals were successfully grown.

INJECTION EXPERIMENT 7:15:92

Before melt down of the B_2O_3, the top cover of the HP furnace chamber was opened to install a quartz heat shield above the crucible. The indium was molten ($\approx$ 350°C) but the B_2O_3 had not melted. The top cover of the HP furnace was replaced and the furnace chamber was back-filled with N_2 gas to approximately 60 psi. After several minutes the N_2 was exhausted then the chamber was placed under vacuum. Again, after several minutes the process was repeated and the crystal growth chamber was pressurized to $\approx$ 400 psi. During this vacuum baking process, the RF generator was shut down.

The in-situ process started by turning the RF generator ON and by slowly increasing the power output melt down of the indium and B_2O_3 continued in the usual manner until the temperature of the indium was raised above the melting point of InP (1063°C). At this point, the phosphorus injector with the side transfer tube was lowered into the melt, crucible rotation started (0.1 rpm) and the injection of phosphorus vapor into the molten indium was in process. Injection was completed in about 28 minutes. During this time there were only two or three small puffs of smoke that occurred from the melt -- crucible rotation was increased (2.0 rpm) and the smoking ceased.

This injection experiment was the first completed that did not cause heavy phosphorus smoke. None of the sight windows were coated and the quartz heat shield above the crucible was clear. Because of the excellent visibility afforded us, we were able to dip the InP seed into the melt immediately after injection and a crystal was grown. Usually, one has to wait approximately one hour for the phosphorus coating to burn off the windows and heat shield. In some instances the coating is so thick that it never burns off and the experiment has to be aborted. At this time there is no clear understanding why this technique kept the windows and heat shield clean. We suspect that some impurities were evacuated from the In melt during baking, perhaps In_2O.

14

INJECTION EXPERIMENT 7:17:92

The vacuum baking process used in the previous experiment was repeated. Everything was going well -- we experienced some temperature problems with the injector, but by increasing the output of the RF generator we were able to complete the injection. Not long after the injector was pulled out of the melt an explosion occurred and the experiment had to be aborted -- no crystal was grown.

During clean-up (after the explosion) we observed that the crucible shaft had slipped approximately 7 inches out of the bottom of the furnace chamber. When this occurred -- the crucible support furniture dropped about 1 inch below its normal position in the RF coil. Because of the change in position of the crucible, the phosphorus injector was now 1 inch above the melt from its normal position. We noted that during the process, the injector temperature would drop and stall. The RF generator output was increased to compensate for this situation, but it was difficult to maintain a constant temperature rise which is crucial for successful injection.

When the injector was pulled from the melt, the temperature of the melt was about $1140^{\circ}C$ so the vapor pressure of the InP melt must have been over 27.5 atmosphere. Because of the high pressure of the melt -- the low phosphorus pressure in the injector, the liquid InP was pulled (capillary action) into the transfer tube of the injector and froze. Now, the internal phosphorus pressure in the injector was too great and this caused the explosion. The system had to be shut down -- no crystal was grown but we had a successful injection and the InP product will be used to grow a single crystal.

Since we increased the crucible diameter from 3 to 5 inches, we were not able to pull all the InP melt out of the crucible. When 50% of the melt was depleted, the growing crystal had to be pulled because the melt started to freeze under the growing crystal. A study was made to determine the cause of the melt freezing problem. A decision was made to re-design the insulation support package as shown in Figure I-12. The original insulation support package did not completely cover the bottom of the susceptor. By increasing the diameter of the insulation package to that of the susceptor, this solved the InP melt freezing problem. We are now able to pull nearly all of the melt out of the crucible except for about 25-30 g from a 1 Kg^+ charge.

THERMAL RESPONSE OF PHOSPHORUS INJECTOR

Experiments were conducted in order to examine the temperature response of the phosphorus injector with respect to its locations from the melt surface. A quartz ampoule was filled with red phosphorus to about 2/3 of its volume and the crucible contained the B_2O_3 encapsulated indium. Seven thermocouples (as shown in Figure I-13) were placed around and on the injector to measure temperatures at these different locations. These temperatures change significantly with the injector's distance from the melt surface. Indeed, the response of the thermocouples are very fast which confirms

our theory that the radiation plays a dominant role in heat loss from the melt surface even in a high pressure (600 psi) crystal growing furnace. At this time, all the data from this experiment has been collated and will be plotted.

SEMI-INSULATING InP

We have grown semi-insulating InP using iron as a dopant. We find a distribution coefficient, k_{eff} = 0.001. In the MLEK process the seed/tail variation of iron concentration is about 1:10. If the iron concentration in the crystal exceeds the solubility limit of 1E17 cm^{-3}, precipitates appear in the NIR images. It is desirable to grow semi-insulating InP with as little iron as possible, but enough to compensate the shallow donor impurities.

Adding the total shallow donor impurities from Figure I-6 gives a value for N_D of 2-3E15 cm^3. Hall measurements show the net free carrier concentration is 3-4E15 cm^3. In order to render this material semi-insulating, a deep acceptor level greater than 4E15 is required. But since all iron is not electrically active in InP, one expects that compensation of such crystals would require a total Fe concentration of 5E16 cm^3, which is close to the solubility limit for iron in the crystal.

In our experiments, however, iron doped crystals grown from either vendor B or C have produced consistently semi-insulating InP crystals even when the iron concentration is only 0.1 ppmw as shown in Figure I-14. Because these crystals are grown by a single step process with an applied magnetic field, they differ from commercial material. The in-situ process allows the use of high purity starting materials to make low iron-doped InP with semi-insulating properties.

CHARACTERIZATION

An InP crystal has been characterized to determine the influence of MLEK thermal environment on crystal shape and dislocation density. The crystal was cross-sectioned and prepared for NIR transmission analysis as described previously[7]. The solid-liquid interface shape is indicated by the striation pattern in Figure I-15. The crystal forms on an ellipsoid of rotation with an aspect ratio x/z = 1.6/1. The steep curvature near the flat top of the crystal indicates a steep radial gradient, caused in part by the applied magnetic field. This shape is more conducive to single crystal growth than a flat interface. Twinning is a common occurrence in LEC growth of (100) InP where the interface is much flatter.

The dislocation density was measured on an etched (100) wafer cut from a (100) InP MLEK boule. The etch pits as determined by micrographs indicate the dislocation density. A high dislocation density has been observed on commercial InP crystals

---

[7] Bachowski, S., et. al., Proceedings of the Second International Conference on InP and Related Materials (1990) p. 30.

grown by LEC[8] and the radial distribution varies by an order of magnitude. By comparison, MLEK material has a lower overall dislocation density and uniformity. Figure I-16 shows that for MLEK crystals the radial EPD distribution varies by a factor of two.

A decision has been made to which vendor indium will be purchased from to produce high quality single crystals of InP. Table 1 shows the Hall measurements made from indium received from three (3) different vendors. These indium ingots were used to grow InP crystals and crystal samples from the seed end and tail end were characterized. As shown in Table 1, vendor "C" indium produced the best crystal.

The magnetic field contours of the crystal growth furnace were mapped at half power using a Walker Scientific, Inc. MG-1D Gaussmeter (Figure I-17). A constant field strength was verified in a 6 inch wide by 10 inch high area centered on the melt crystal interface. Melt temperature was determined with chromal-alumel thermocouples enclosed in quartz sleeves inserted into the melt, in the absence of a crystal (Figure I-18). Measurements were made to establish axial temperature profiles at the center and half way to the crucible wall (Figure I-19). Time dependent temperature fluctuations with and without a magnetic field (Figure I-20) and the temperature at the melt center as a function of magnetic field (Figure I-21) were also measured.

CONCLUSION

Since its initial invention in 1926, Kyropoulos growth has succeeded in producing crystals not easily grown by other methods. Crystals which are prone to plastic deformation at high temperatures are naturally suited to this technique. We have demonstrated the MLEK technique for producing InP (100) crystals with uniform dislocation density. The flat top growth is shown to be favorable for twin-free growth of InP. The in-situ process reduces the potential for contamination as a result of reloading the charge material. Finally, magnetic stabilization of the melt aids in growth control; for shape control as well as impurity distribution control.

A uniquely designed phosphorus injector has been fabricated and tested. Successful injections were accomplished using this apparatus. Pyrolytic boron nitride crucibles were used for the first time and characterization data will be published later to establish the purity of the InP crystals.

Controlling the thermal geometry of the crystal growth environment makes it possible to grow (100) InP by the MLEK/MLEC process. There are several advantages for MLEK growth of twin-free InP crystals. (1) Uniform dislocation density, lower than for LEC material, (2) With the high purity in-situ process semi-insulating material with low iron content can be produced, (3) The process can be scaled up to 3-inch or larger diameter crystal growth.

---

[8] Quinlan, K.P., J. Electrochemical Society, 137, (1990) 1991.

Also, during this time (29 June 1990 through 30 September 1992) nine (9) technical papers were published in refereed journals and seven (7) technical presentations were presented at International Conferences. Five (5) invention disclosures have been filed and one (1) patent has been issued (#5,252,175-Oct. 12, 1993).
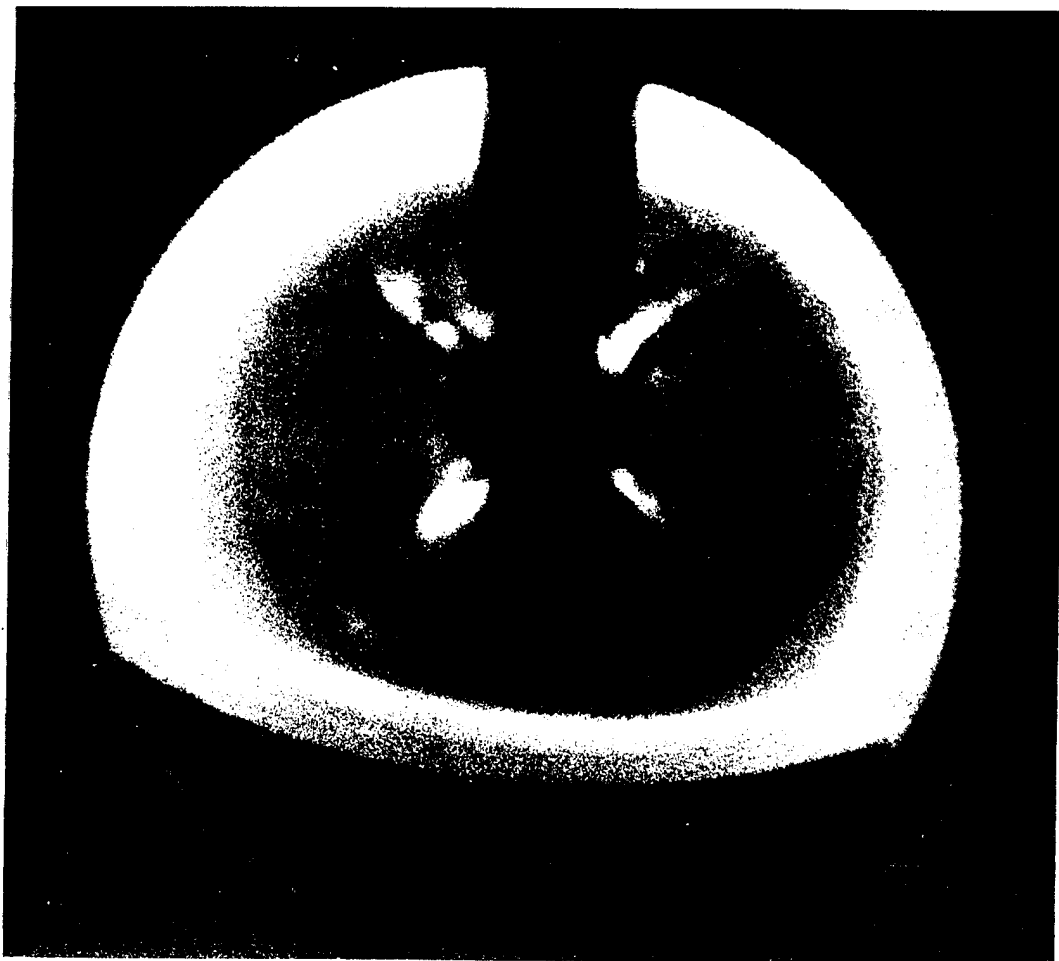
FIGURE I-1

FIGURE I-2

TYPE K
THERMOCOUPLES

THERMOCOUPLE
WELL

QUARTZ
SHIELD

INSULATION

QUARTZ
INJECTOR

P_4 (GAS)

RED
PHOSPHORUS

QUARTZ
CRUCIBLE
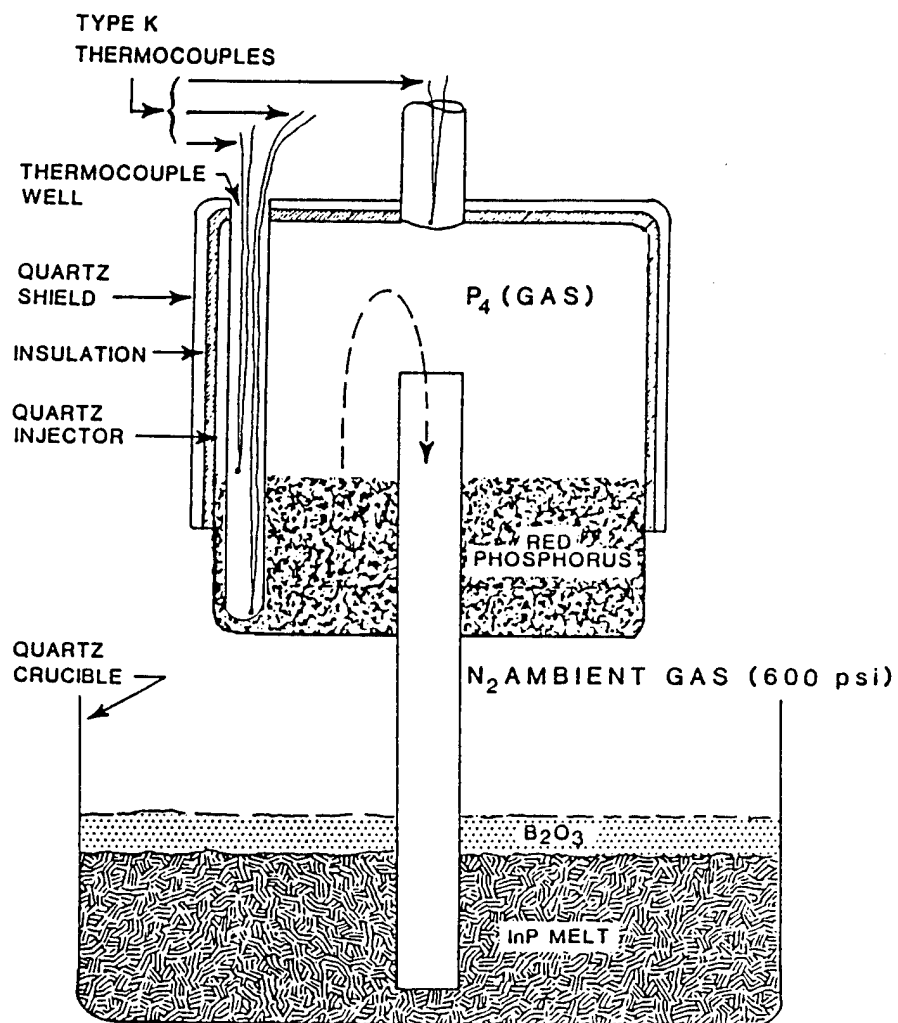
N_2 AMBIENT GAS (600 psi)

B_2O_3

InP MELT

FIGURE I-3

TEMPERATURE GRADIENT
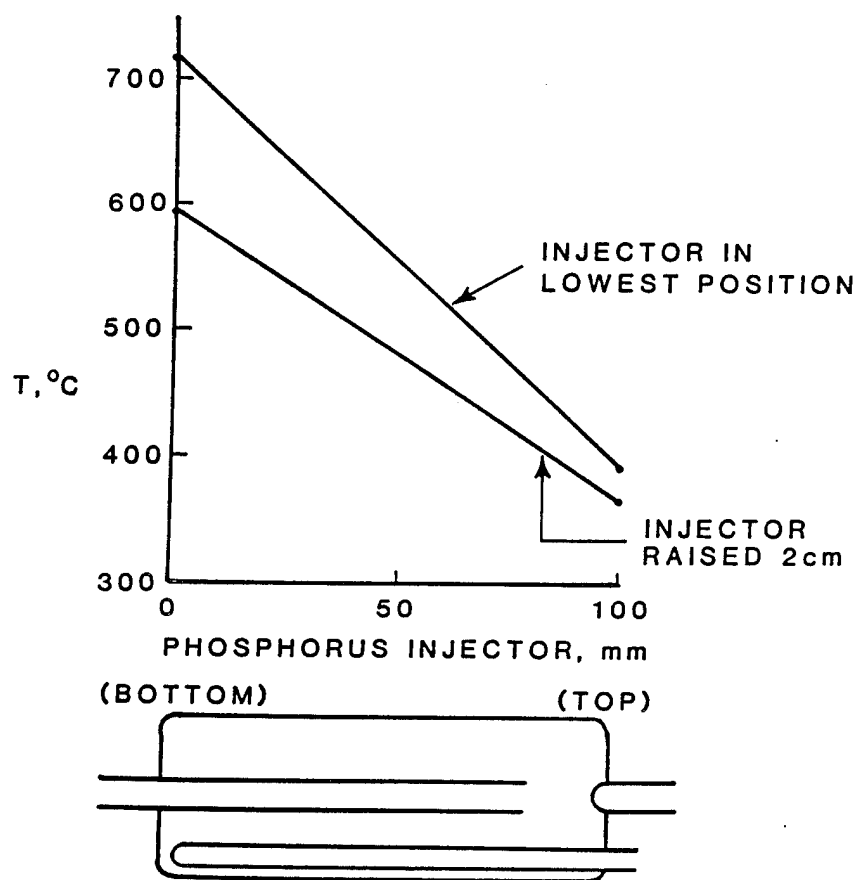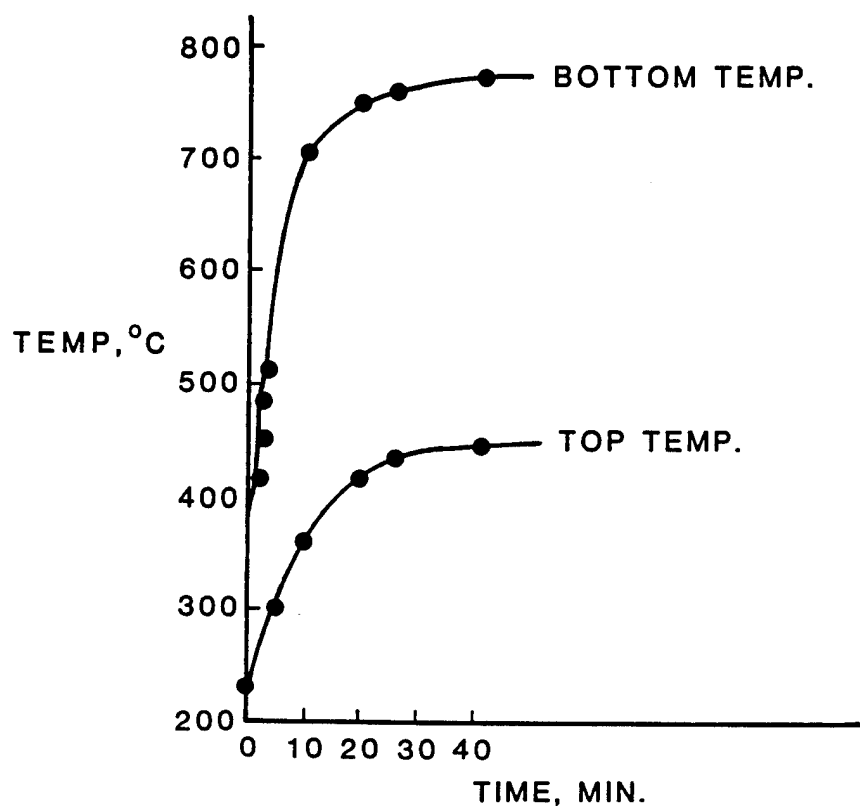## IN PHOSPHORUS INJECTOR

FIGURE I-4

RATE OF TEMPERATURE RISE
INSIDE THE P INJECTOR

FIGURE I-5

CONCENTRATION OF IMPURITY ELEMENTS
FOUND IN InP CRYSTALS

* LESS THAN 10^{14} ATOMS / CC

FIGURE I-6

FIGURE I-7

PHOSPHORUS
INJECTOR

4K GAUSS
MAGNET

FIGURE I-8

FIGURE I-9

SEED SHAFT

TYPE K THERMOCOUPLE

B$_2$O$_3$

QUARTZ TUBE

INDIUM

FIGURE I-10

BOTTOM OF
INJECTOR T/C

SEED SHAFT

TRANSFER TUBE
TYPE "K" T/C

TOP OF INJECTOR T/C

QUARTZ SHIELD

INJECTOR COVER

P INJECTOR

InP SEED CRYSTAL

QUARTZ CRUCIBLE

GRAPHITE SUSCEPTOR

LOW CON FELT

IN

B_2O_3

PRED

BOTTOM OF
CRUCIBLE T/C

FIGURE I-11

29

STAINLESS
STEEL

QUARTZ

INSULATION
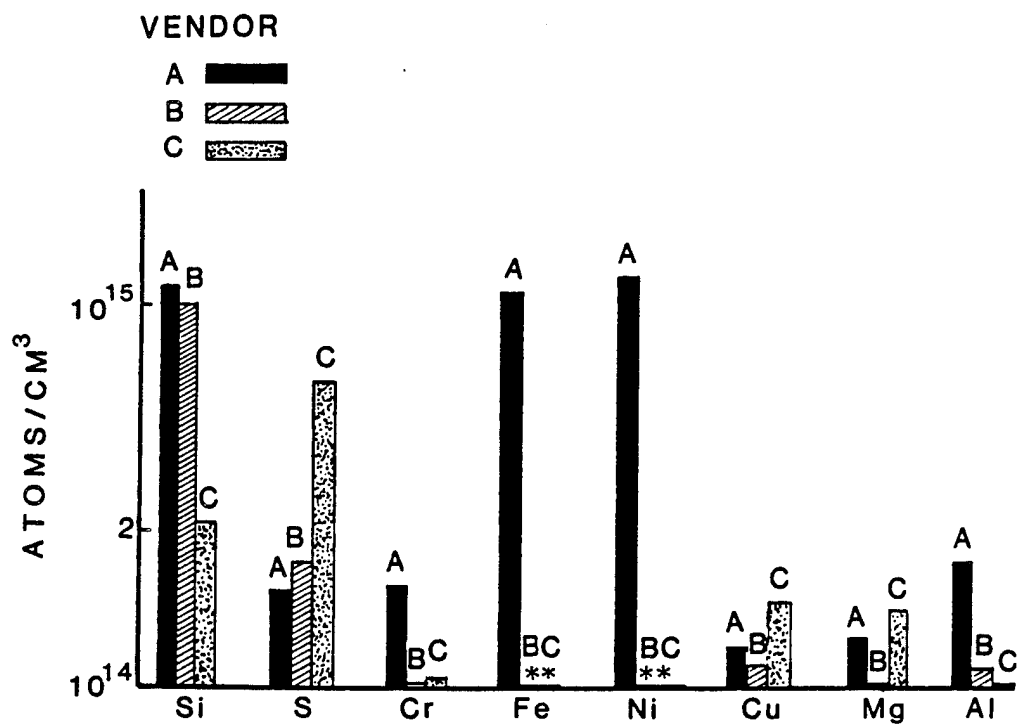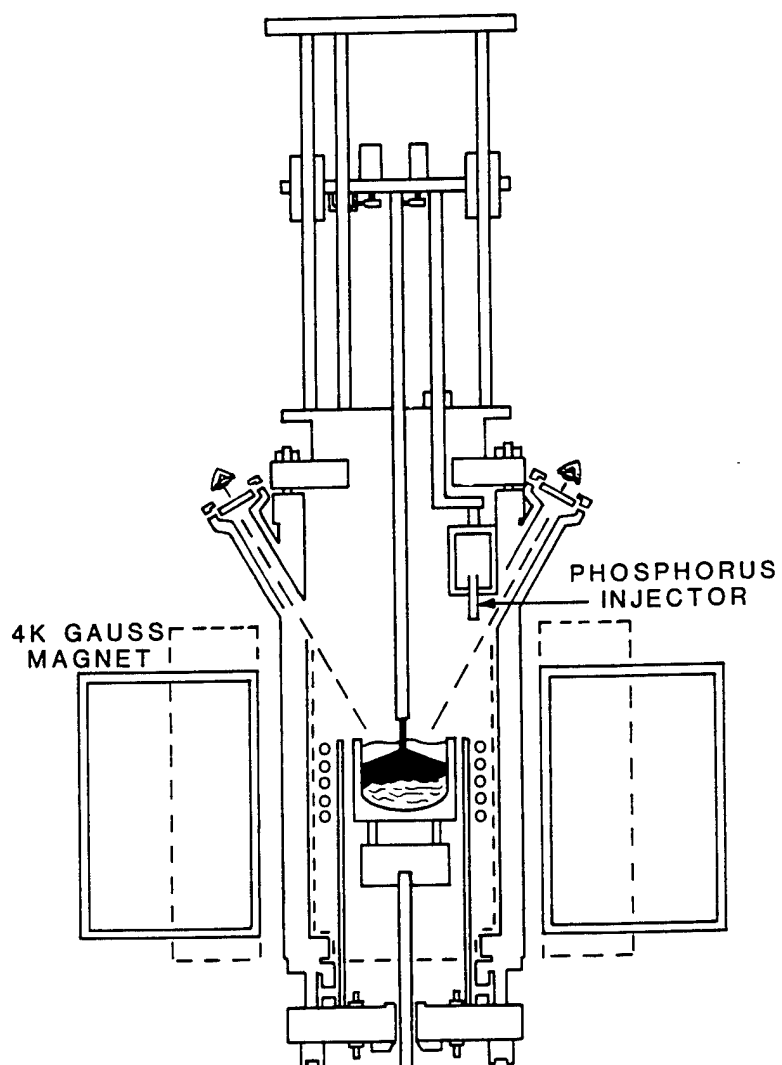
BORON
NITRIDE

INSULATION

GRAPHITE
SUSCEPTOR
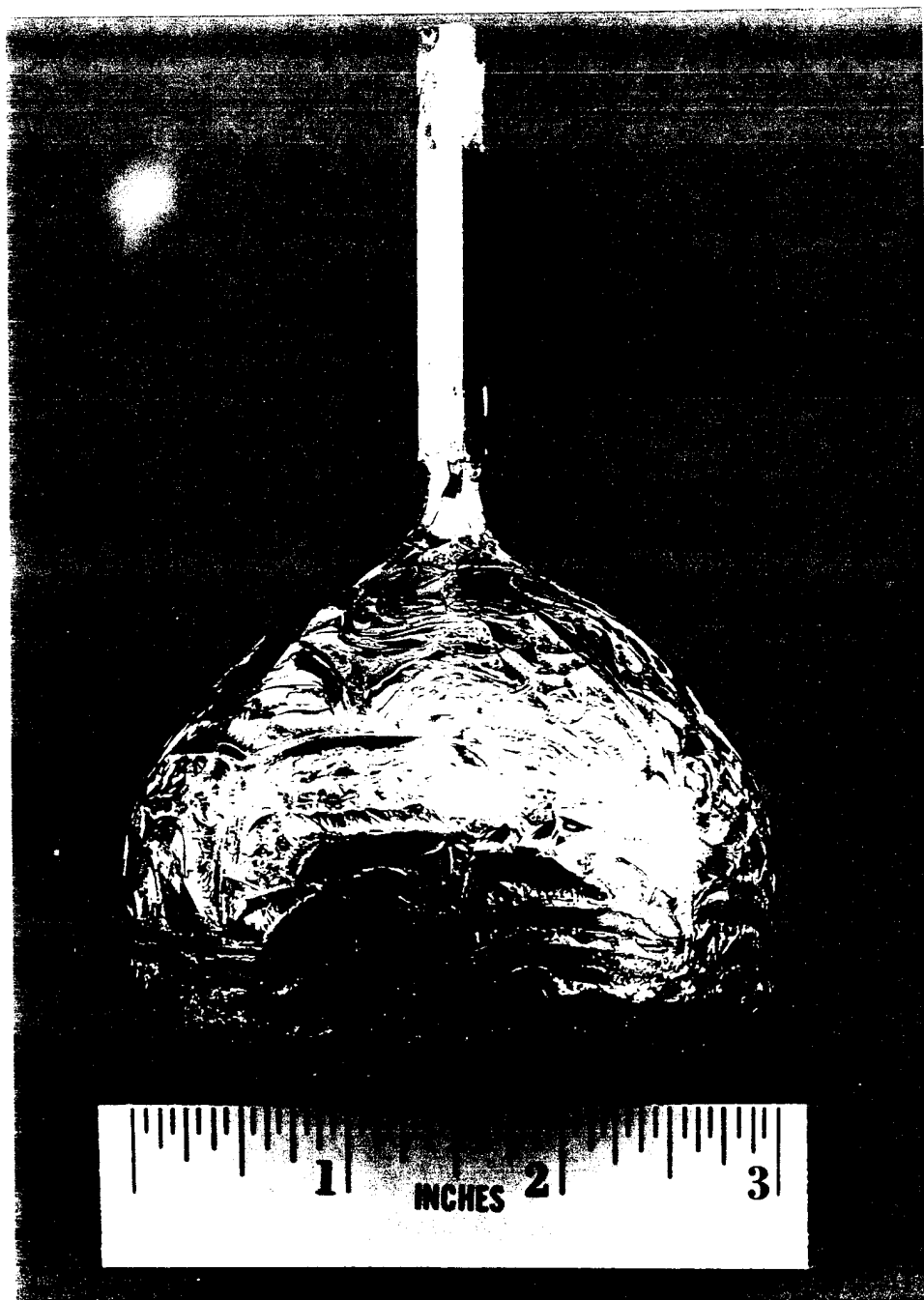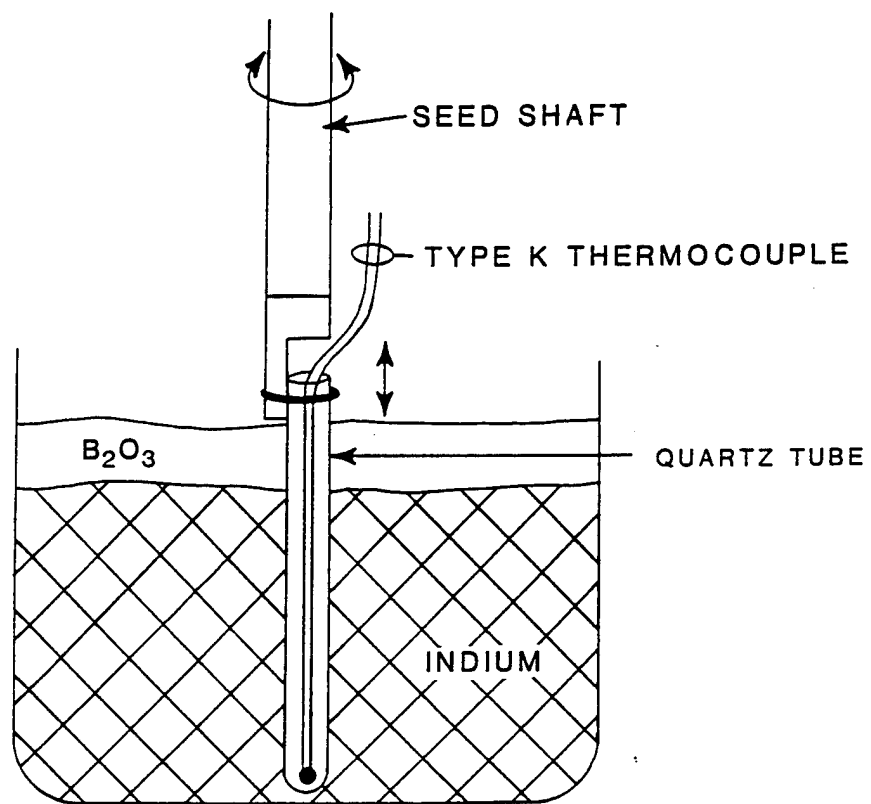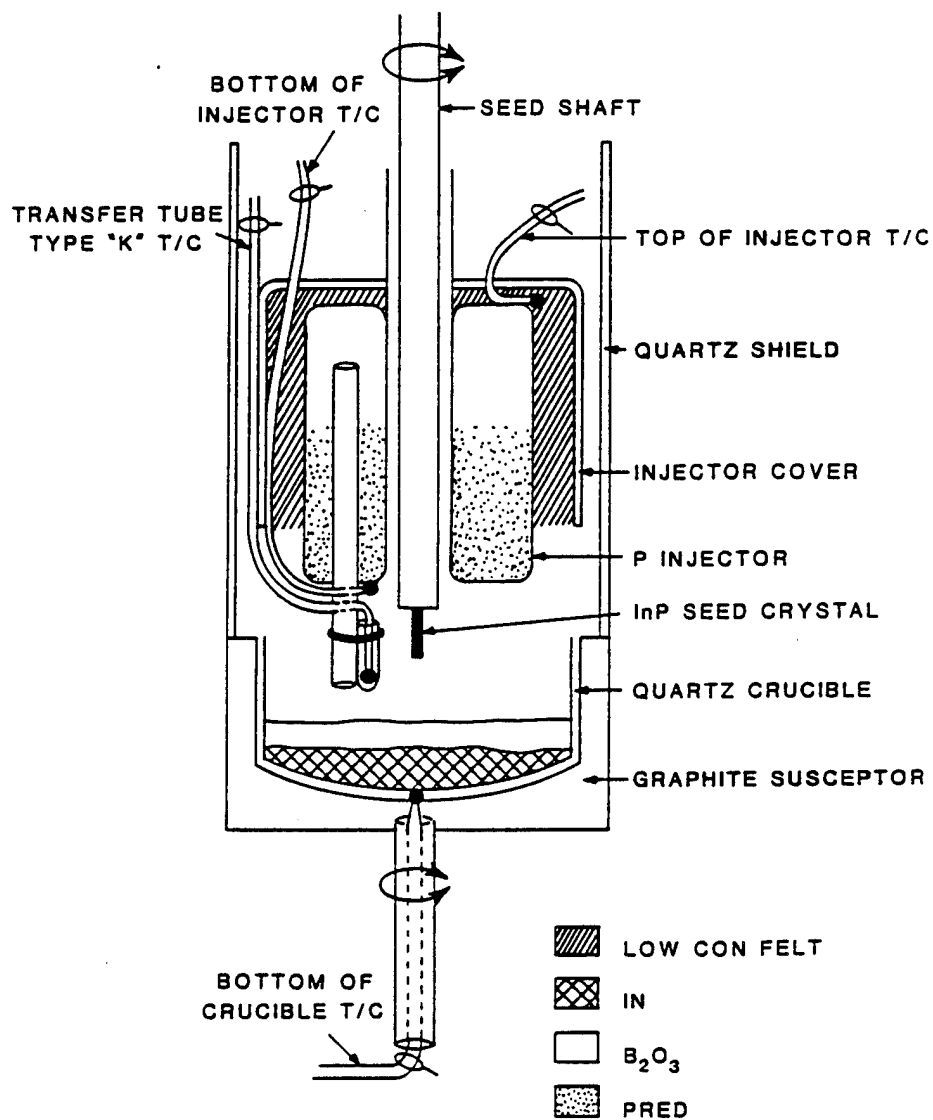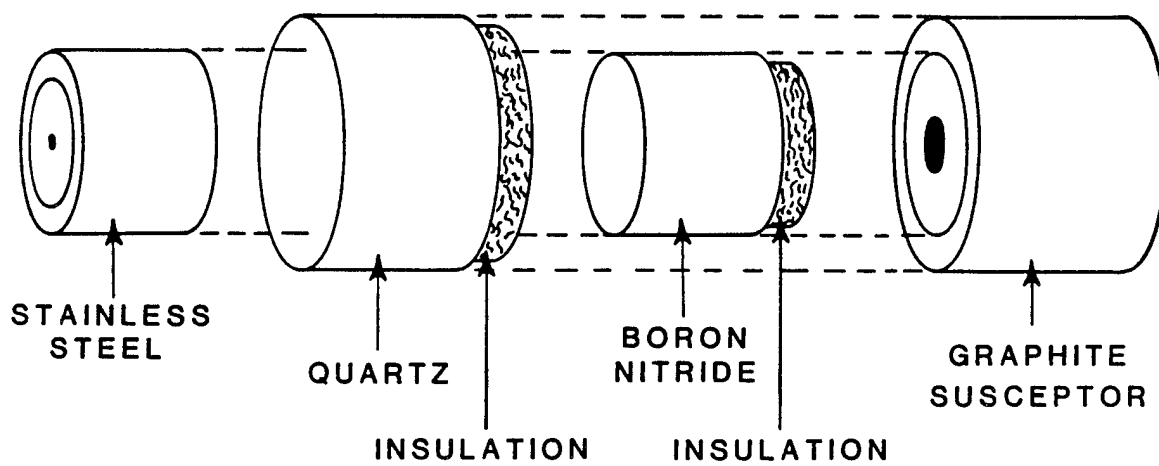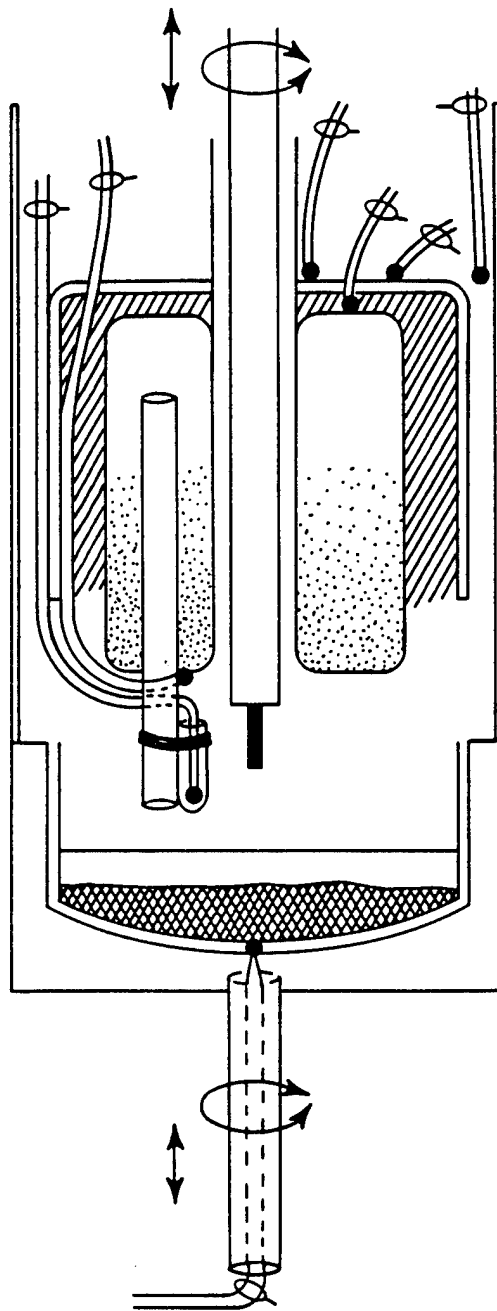
FIGURE I-12
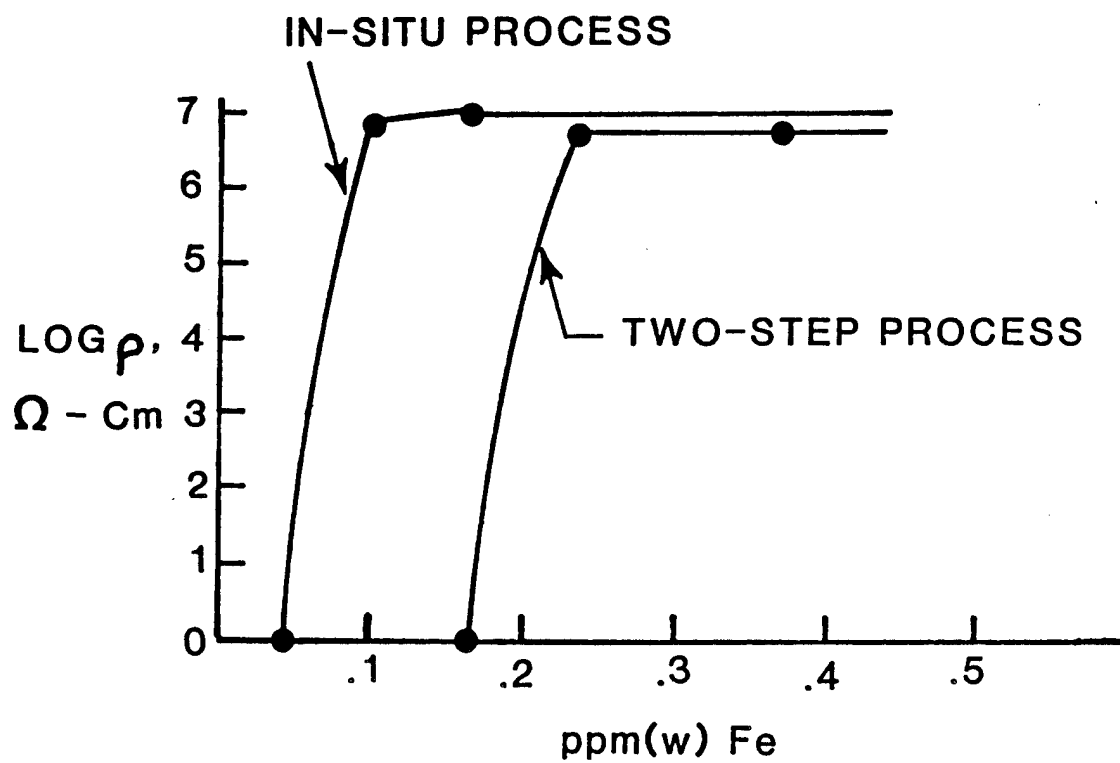
FIGURE I-13

FIGURE I-14
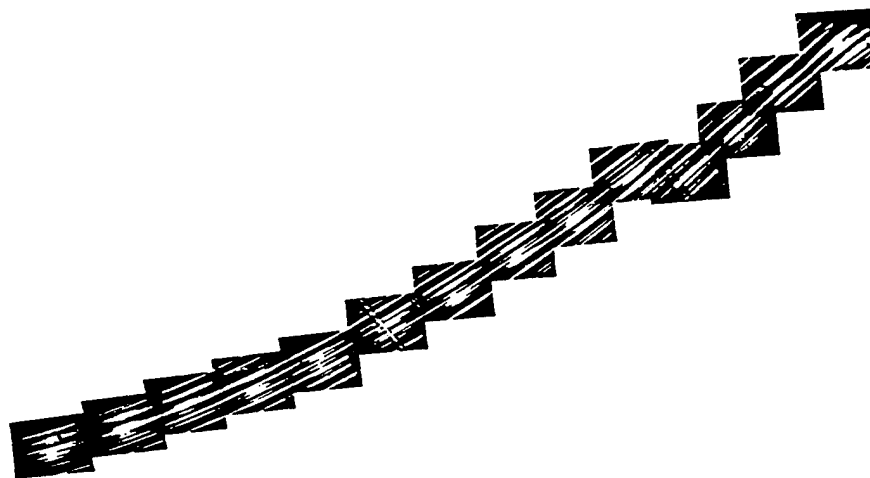
FIGURE I-15

FIGURE I-16

33
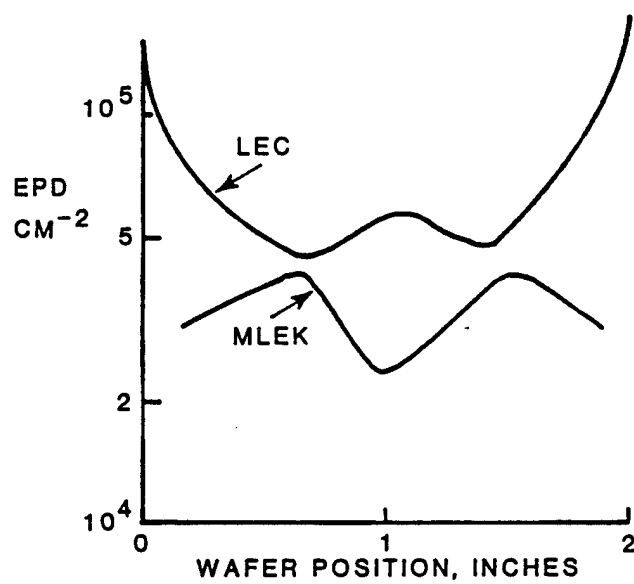
ISOCONTOURS OF MAGNETIC FIELD AT HALF POWER

FIGURE I-17

34

CONAX FITTING

INJECTOR SHAFT

FOLLOWER

SEALANT

FOLLOWER

CRUCIBLE

RF COIL

B_2O_3

InP

2"

SUSCEPTOR

HEAT SHIELD
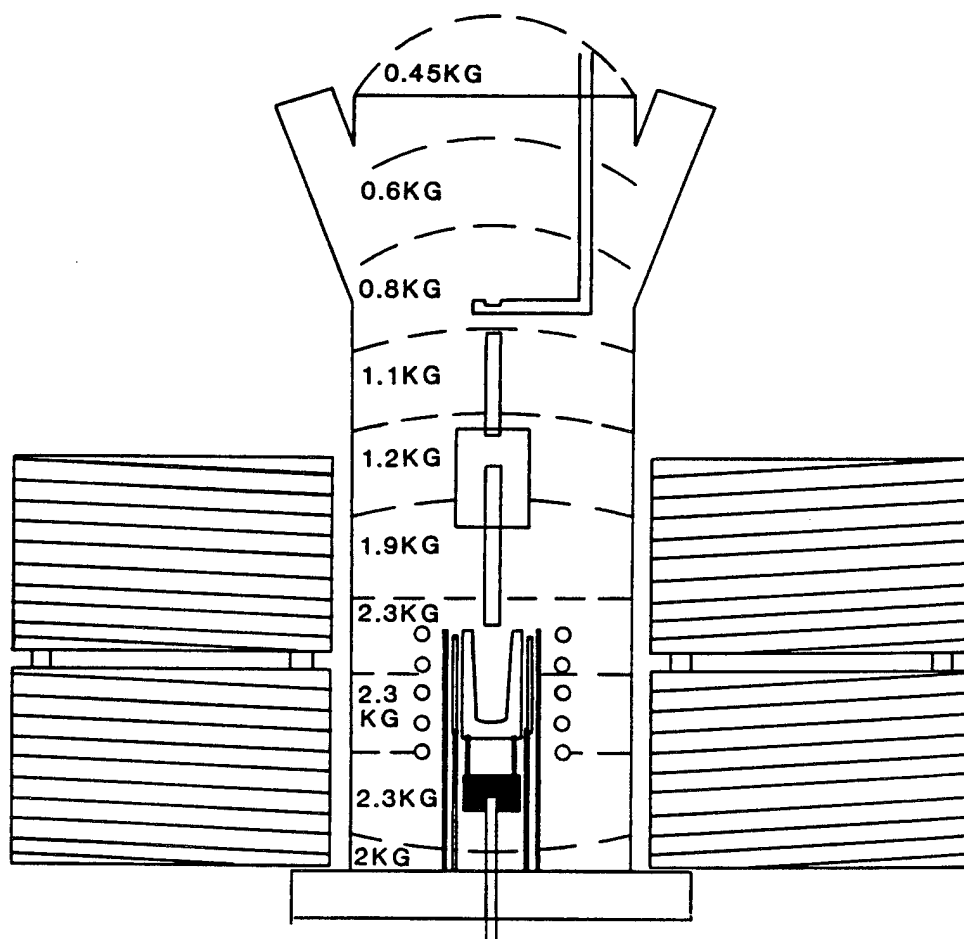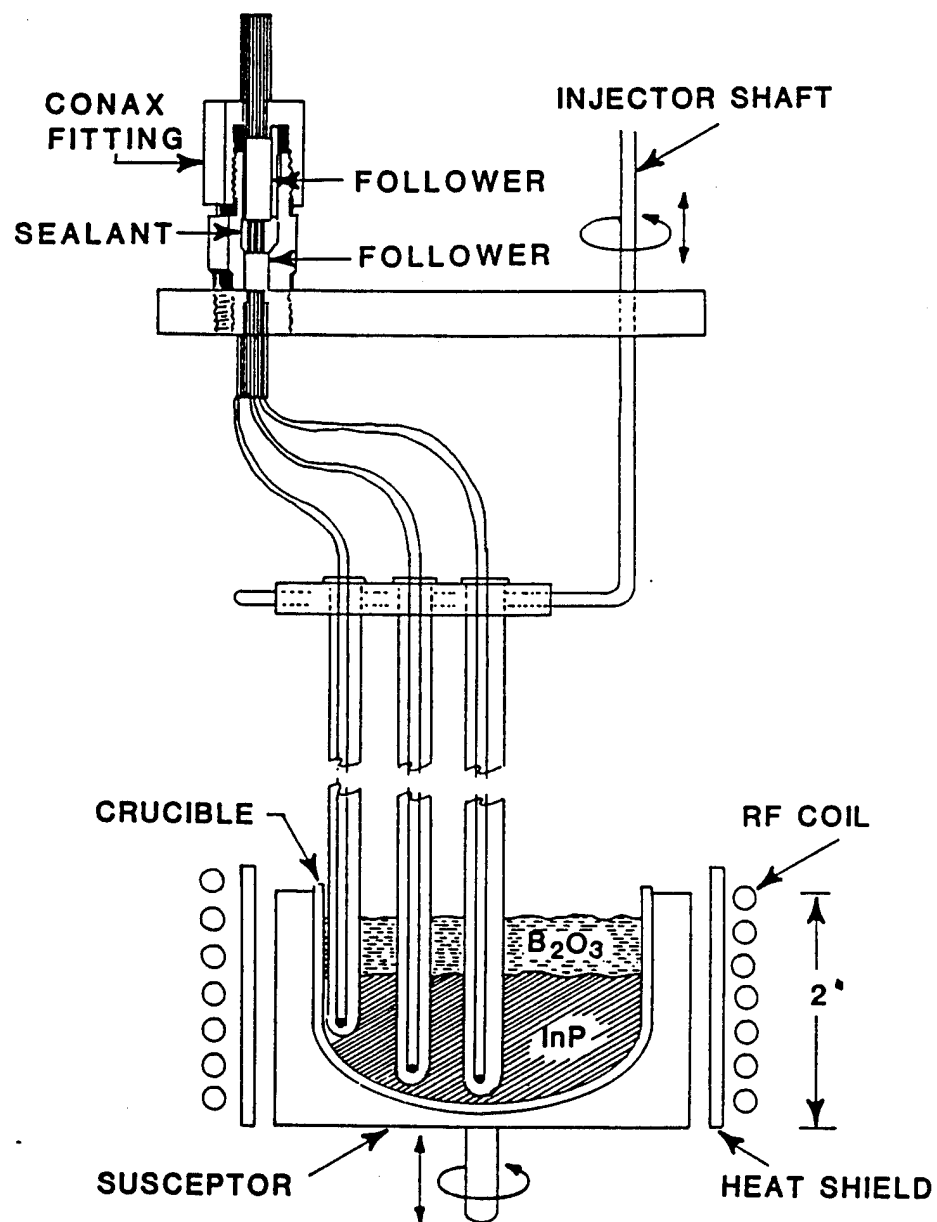
FIGURE I-18

AXIAL TEMPERATURE PROFILE
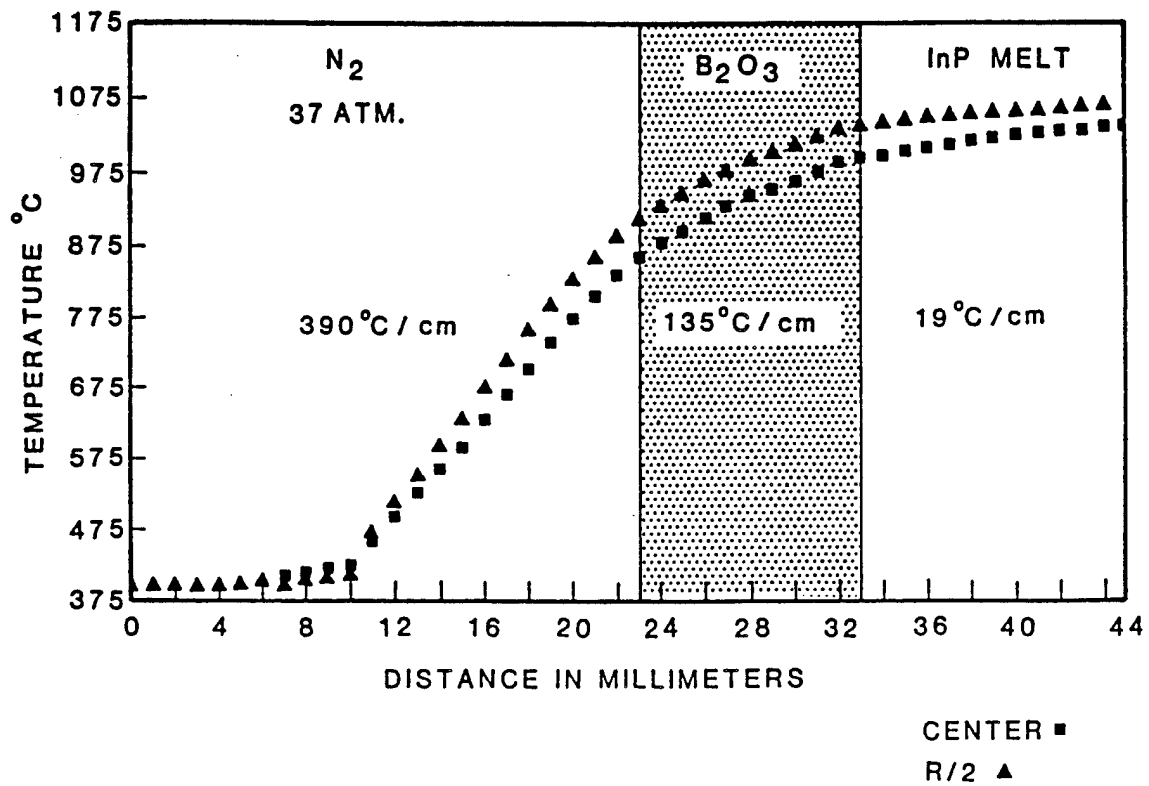
FIGURE I-19

TEMPERATURE FLUCTUATIONS IN MELT

FIGURE I-20

MELT TEMPERATURE VS MAGNETIC FIELD
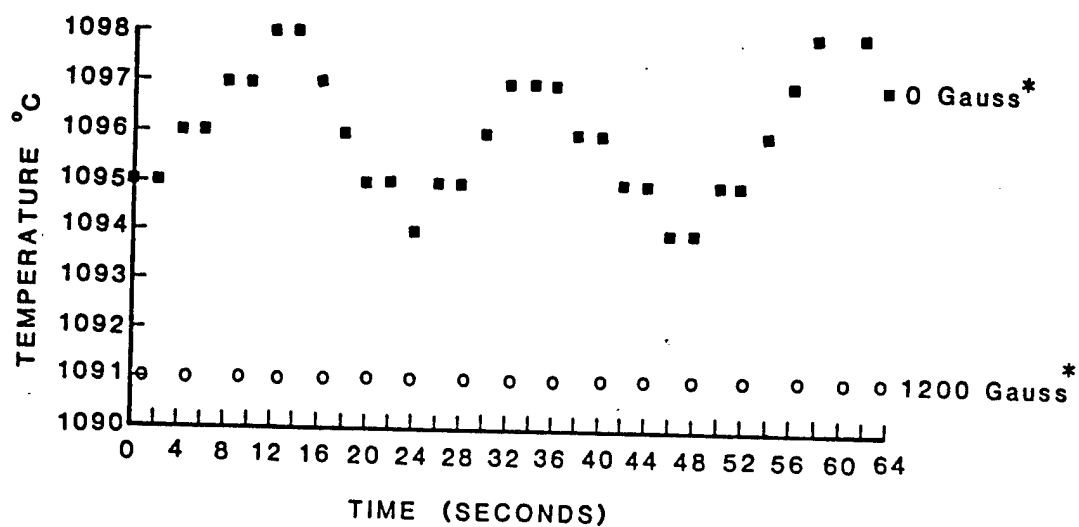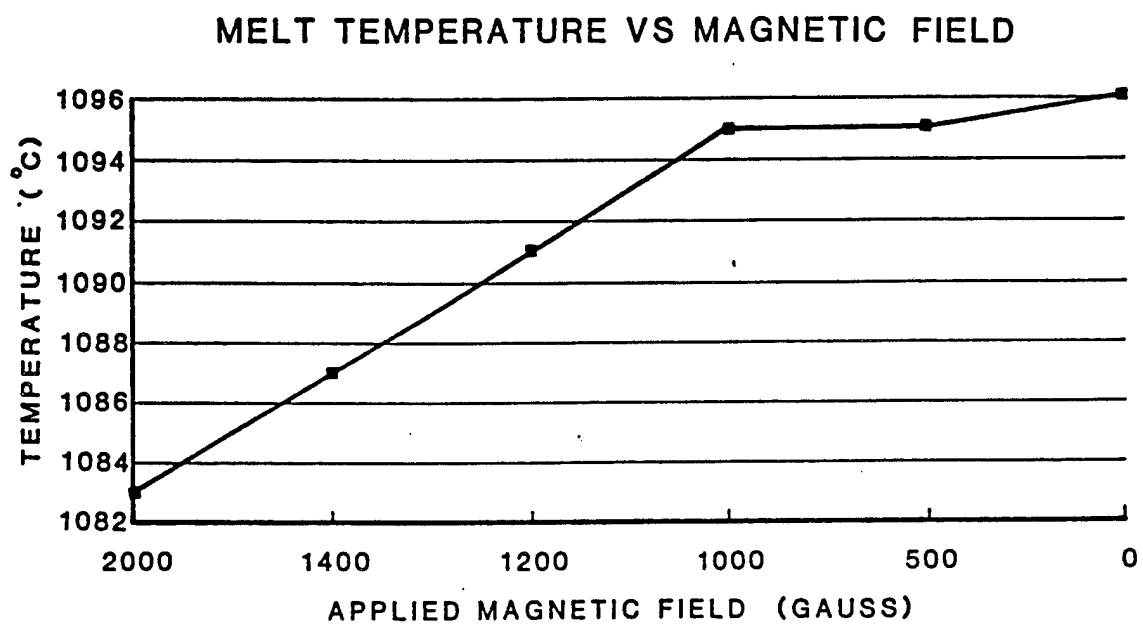
FIGURE I-21

		SEED		TAIL	
		N_D-N_A(cm^{-3})	μ(cm^2/V - sec)	N_D-N_A(cm^{-3})	μ(cm^2/V - sec)
VENDOR A	RT	4.9E15	4,250	5.6E15	4,380
	77 K	4.3E15	28,600	4.7E15	24,000
VENDOR B	RT	4.2E15	4,300	3.14E15	4,600
	77 K	3.8E15	31,000	2.8E15	37,000
VENDOR C	RT	4.3E15	4,460	3.3E15	4,500
	77 K	3.87E15	34,000	2.9E15	38,000

TABLE I-1

BORON PHOSPHIDE

Boron phosphide is an interesting material both as a high energy gap semiconductor and as a substitute for diamond thin film applications. During this period a project was initiated on the growth of boron phosphide using chemical vapor transport with iodine. While this has never been reported in the literature, it should be possible due to the transport of boron using iodide intermediates which was studied extensively at Rome Laboratories during the 1960's and the high vapor of phosphorus at elevated temperatures. The initial runs using the published data were unsuccessful. The formation temperature was $1000°C$, and the decomposition was $800°C$. The result appeared to be that boron iodide was formed at the formation temperature but did not decompose at the expected temperature. A subsequent review of the literature showed that in one instance the decomposition occured more readily at a higher temperature. Thus, runs were made reversing the gradient. These experiments were also unsuccessful. Other references have indicated that temperatures as high as $1200°C$ may be required.

In addition to the vapor phase transport of BP, we planned some experiments to grow BP using a solution growth technique with molten copper phosphide as the solvent. Small BP crystals were grown using platinum as the solvent at General Electric during the 1960's. Japanese workers claim some success using copper, but again only small crystals. We would like to attempt to grow useful size crystals using top seeded melt and an encapsulant. The equipment necessary had been refurbished for another project and was available. Because of the renovation of BLDG #1141, we lacked the space to do this study in this contract period.

BISMUTH SILICATE

The major effort during the contract was the growth and doping of bismuth silicate, a promising electro-optic material with several possible applications. We initiated a study on the optical absorption of doped bismuth silicate crystals to determine whether there might be some difference in the absorption due to the dopant. We have used several wavelengths from the visable to the ultraviolet. We made over sixty transmission scans of the IR and visable spectrum using both doped and undoped samples grown by the Czochralski and hydrothermal techniques. From these scans, the cutoff and the tangent to the cutoff values were determined for a wide variety of doped samples.

Initially, the absorption coefficient was determined at three wavelengths; 500, 600 and 750 millimicrons. All this data was entered into a database on Windows using a computer with a large memory in Building #1142. This enabled us to make comparisons between different properties which might allow us to determine the dominant properties required for photochromic material. We developed a data base for the comparison of the absorption coefficient of eleven polished slices taken from different locations in the same Czochralski grown boule. From this we were able to determine the optical uniformity in a

40

Czochralski boule. We made a similar comparison using a hydrothermally grown crystal. The results indicated a high degree of uniformity in both cases. We presented a paper on these results at the International Conference on Crystal Growth(in August in San Diego) and was published in the Journal of Crystal Growth(October). In the meantime, we took selected optical samples and extended the number of absorption coefficient points to twenty using a different data base, again in 500-750 millimicron range which is of most interest. This data has been transferred to another computer program (Sigmaplot) which automatically plots curves of the wavelength vs the absorption coefficient. With this data compiled, we compared these curves as functions of the length along the crystal and across the crystal(crystal uniformity), of dopants, stoichiometry and of the crystal growth technique. A second series of Czochralski runs, using different melt stoichiometries was also analysed, again we found no significant changes in the optical uniformity in any of these results. These results were presented at the AACG meeting in June, 1993. During the rest of the contract period, we concentrated on the phosphorus doping of bismuth silicate since this element did seem to bleach the crystals similar to the manner of aluminum doping. In aluminum doping the bleaching is reported to be due to p-type imperfections; in the phosphorus doping it may be the result of n-type imperfections.

For the purpose of this work, we spent some time developing a method for the preparation of bismuth phosphate which we used as the dopant.

ZINC GERMANIUM DIPHOSPHIDE

We have attempted to tranfer cadmium germanium phosphide, but we were unable to until we obtained starting material. This was finally synthesized at RL in a pressure vessel used for the crystal growth of indium phosphide. While not pure ZnGeP, this was used as a nutrient for the growth of ZnGeP using chemical vapor transport.

Chemical vapor transport (CVT) involves the movement of a polycrystalline, or powdered, starting material from one heated region of a tube to a second heated region under the influence of a transporting agent usually iodine. Crystallizaion occurs in the latter region which may or may not be seeded. Success of the technique relies on the formation of a gaseous intermediate at the temperature of the starting(nutrient) zone and the disassociation of this intermediate at the crystallization zone temperature.

It is possible to estimate the desired temperatures for this transport from thermodynamic data. The standard values for H(enthalpy) and S(entropy) can be found in thermodynamic tables such as Kubaschewski(1). The F(free energy) can then be determined from the equation;

$$F = H - T S$$

for the transporting reaction at the desired temperature. One can then solve for K_p using the equation;

41

$$F = -RT \ln K_p$$

where K_p is the ratio of pressures between the intermediate/reactant. The equilibrium temperature can then be calculated by selecting a desired value of K_p. According to Jeffes[2], this value should be between 10 and 10^{-1} for best results. He plotted these temperature vs K_p for a number of systems. The sign of H for the formation of the transporting compound is also significant. If it is negative the reaction will proceed from the lower to the higher temperature(exothermic) while if it is positive the reaction will go from the higher to the lower temperature.

Both the physical perfection and the purity of the crystal are affected by the growth rate. Generally, the faster the growth, the less perfect the crystal. Thus, a tradeoff has to be made between the growth rate and the desired perfection.

It should be mentioned that it is rarely necessary to actually perform calculations to determine the desired operating temperature since there is sufficient experimental data in the literature to estimate initial reaction temperatures for almost any system.

While either elemental or two component compounds have been most investigated for chemical vapor transport some ternaries have also been successfully grown. These are mostly ternary sulfides[3]. Binary phosphides have been reported in the same reference. Thus, it did seem feasible to grow zinc germanium phosphide by this method, based on certain assumptions.

The temperature in the nutrient zone must be sufficient to partially decompose the $ZnGeP_2$, specifically to partially vaporize some of the phosphorus which will then travel to the growth zone at the lower temperature. Since the temperature of the starting zone will be higher, the zinc remaining in the compound should also vaporize to the lower zone since it also has an appreciable vapor pressure at elevated temperature. This is not actually the case as it has been found that zinc diiodide[4] is the transferring medium. This compound is responsible for the zinc transport in several zinc compounds, including zinc selenide, zinc sulfide and zinc telluride. The transfer is from the higher to the lower temperature. The upper temperature is usually in the range from $950°C$ to $1000°C$ while the lower temperature is from $850°C$ to $800°C$.

Except for zinc, the only element that has to be transported chemically is the germanium, the transport of which has been studied previously[5]. Both GeI_2 and GeI_4 theoretically could be used for the germanium transport. One rule of this type of growth however, is that the transfer should occur below the melting point. The free energy of formation of germanium tetraiodide (at room temperature) is over -100 Kcal/mole indicating that the tetraiodide is stable to about 2000 °C indicating that a reverse reaction to deposit the germanium is highly unlikely at reasonable temperatures. The free energy of formation of the diiodide is about -56 Kcal/mole which is also quite high. There is

another reaction that does show promise at temperatures below 1000° C and has been studied previously (4). This is;

$$GeI_4 + Ge = 2GeI_2.$$

This reaction has a F of -4.9 Kcal at 727°C and since this value is decreasing(toward zero) with increasing temperature, transport should be possible in the 800-1000°C which should produce near equilibrium concentrations since the free energy is near zero. A rough calculation results in the value of F=0 at 973° C which indicates this is the temperature at which the reaction is at equilibrium. As indicated by Jeffes, one does not have to operate through equilibrium but can also be near equilibrium and still have successful transport. Theoretically, the rate of transport can also be calculated. This would be a worthwhile exercise if we have successful transport.

There are two limiting factors as to the desired temperature range. First, the melting point of germanium is 958° C which is below the estimated equilibrium temperature. This may not be significant since we are not attempting to produce elemental germanium but to reproduce a solid compound. The melting point of the ternary compound is over a thousand degrees(6) so it might be possible to use the equilibrium temperature for the transport. The same authors(6) report that unless the preparation temperature of the ternary is above 850° C, zinc phosphide forms and prevents the formation of the ternary compound.

Based on the above, one could suggest several experiments to determine the feasibility of the growth of $ZnGeP_2$ by the transport method. First we tried transporting the compound using a gram of iodine and about 15 grams of the compound with a gradient of 1000° to 950° C. The experiment was successful in that ZnGeP was transported. The starting material was synthesized using a high pressure furnace used for the indium phosphide project. X-ray analysis indicated that the nutrient was not pure ZnGeP, but consisted of several phases. X-ray analysis of the tranported material showed only the lines associated with pure ZnGeP. Several runs were performed all of which gave the desired product. Small changes in the temperature profile were used in these runs, but no signficant improvement occured. Crystals of greater than five mm in their major direction were produced by lowering the iodine pressure and using a quartz rod affixed inside the cool end to act as a cold finger. The rod extended outside the furnace .

The runs were continued using a seed produced from this run.

ZINC OXIDE (ZnO) STUDIES

Zinc oxide is a potentially useful material as a substrate for a variety of optical devices. High quality material is not available at the present time. Therefore, we have initiated a project on the growth of this material using the hydrothermal technique. Some

43

research on the hydrothemal material was done several years ago at the Bell Laboratories(7) and was used as a starting point for this study. The initial runs using the Bell data resulted in no transfer; in fact, the seed dissolved in most cases.

PUBLICATIONS UNDER CONTRACT

1. Synthesis and growth processes for zinc germanium phosphide, D. Bliss, M. Harris, J. Horrigan, W. Higgins A. Armington and J. Adamski, Journal of Crystal Growth, 137(1994)145.

2. Optical studies of Czochralski and hydrothermal bismuth silicate, M.Harris, J.Larkin, E.Cormier and A. Armington, Journal of Crystal Growth,137(1994)128.

3. Growth of non-linear BSO using the hydrothermal technique, M. Harris, J. Larkin, E. Cormier and A. Armington

PATENT APPLICATIONS

1. Hydrothermal Growth of non-linear optical materials, M. Harris, E. Cormier, J. Larkin and A. Armington.

2. Crystal Growth of zinc germanium phosphide, M. Harris, D. Bliss, A. Armington.

REFERENCES

1. Kubaschewski and Evans, <u>Metallurgical Thermochemistry</u>, Pergamon Press(1967).

2. J.H.E. Jeffes, <u>J.Crystal Growth</u>, 3/4(1968)13.

3. H. Schafer, <u>J.Crystal Growth</u>, 9(1971)17.

4. H.Schafer, <u>Chemical Transport Reactions</u>, Academic Press, NYC,NY,(1964).

5 .R.F.Ralsten, <u>Iodide Metals and Metal Iodides</u>, John Wiley and Sons, New York(1961), p292.

6. K. Masumoto, S. Isomura and W. Goto, <u>J. Phys. Chem. Solids</u>, 27,(1966)1939.

7. R.A. Laudise, E.A. Kolb, & A.J. Caperaso, J. Amer. Ceram. Soc., 47 (1964) 9.

INTRODUCTION

Periodic check ups and maintenance were performed to ensure performance of the ultra high vacuum systems used to make refractory metal silicide infrared sensitive diodes. The system that had a load lock installed during this period needed numerous adjustments. Another wafer holder is being fabricated hopefully with the correct parameters.

The laboratory has several different types of pumping systems used to create ultra high and high vacuum ambiants used in a variety of processes. The mechanical pumps used are compound oil-sealed rotary vane pumps. "Compound" refers to the fact that there are two pumping stages in series. This allows the pump to attain pressures in the 10^{-4} scale as opposed to single-stage pumps, which are generally limited to about 25 microns. "Oil-sealed" refers to having the pumping mechanism immersed in a reservoir of oil. The oil is a high grade, turbine oil that has been vacuum distilled to remove the most volatile components. This distillation results in a fluid with considerably less vapor pressure.

In addition to sealing the pumping mechanism from the atmosphere, the oil serves as a coolant and lubricant. And, at lower pressures where the gas volume is low, the oil injected into the second stage provides the mass to force the second stage valve open. Gas molecules entrained in this oil are pushed out into the reservoir and thus diffuse out to the atmosphere. The compression of gas and oil in both stages is accomplished by eccentrically-mounted rotors having internal, spring-loaded vanes. When no oil contamination caused by backstreaming can be tolerated sorption pumps are used.

SORPTION PUMPS

Sorption pumping is achieved through the process of physical adsorption. Electrostatic attraction (Van Der Wall force), although weak, is capable of holding, or adsorbing, a certain amount of gas when it comes into equilibrium with a surface. Since these same forces are responsible for binding molecules together when a gas condenses to form a liquid, chilling the surface to near the liquefaction temperature of a gas (or gases) greatly increases its capacity for adsorbing those gases.

As mentioned earlier, the principle was known in the early 1900's but it was not developed into a viable commercial product until the early 1960's. In order for such development to take place, it was necessary to examine and establish certain required characteristics. First, for a pump to have adequate capability, it must contain a large sorption surface area. This is achieved by using a porous material having a large surface area per unit volume and pore size comparable to molecular diameters. The material used in the sorption pumps is type 5A molecular sieve, which is a synthetic zeolite. It has a surface area of approximately 800 meters^2 per cc, so a standard pump will possess about 300 acres of sorption area.

A sorption pump consists basically of a vacuum-tight enclosure containing an adsorbent which evacuates the air from a chamber in the manner described above. The sorption material in the enclosure is chilled by immersing the pump body in a dewar flask containing liquid nitrogen and this chilling initiates the pumping action. However, since adsorbents such as molecular sieve are inherently poor conductors of heat, and since the maximum capacity of a sorption pump is realized only when the adsorbent is completely chilled, the rate of pumping in most cases is limited by the rate at which the adsorbent material cools. To compound the problem, the sieve becomes vacuum-insulated as the pump pumps on itself. For this reason, great emphasis has been placed on the heat transfer characteristics of the sorption pump design. High thermally conducting, all-aluminum body and internal cooling fins afford the best possible heat transfer characteristics from the adsorbent to the liquid nitrogen bath.

Another characteristic that must be considered is that this pumping action is selective. That is, when a mixture of gases is to be pumped, openly those gases whose liquefaction temperatures are above or near the surface temperature will be adsorbed with any significant capacity. Although certain gases are not pumped well, e.g. neon and helium, it is possible to trap them in the pump thus removing them from the chamber being evacuated. This trapping is accomplished by allowing the in-rushing air to carry all gas constituents, including neon and helium, into the pump, then closing off the valve before these noncondensable gases can migrate back out of the pump into the chamber. A second sorption pump is then used to continue the pumpdown to the crossover point where a high vacuum pump takes over.

Pumping speed is generally not a major consideration when roughing an ultrahigh vacuum system. Several "high" vacuum pumps are used.

DIFFUSION PUMPS

Diffusion pumps are vapor jet pumps that work on the basis of momentum transfer from a heavy high speed vapor molecule to a gas molecule. This results in the gas molecules being moved through the pump.

The bottom of the pump contains an electric heater which is used to produce the vapor by heating the pumping (motive) fluid to its boiling point at reduced pressure. This means that before the pump is started, it must be "rough pumped" down to and held at an acceptable pressure, typically 10^{-1} Torr. To do otherwise will result in no pumping action and possible damage to the pumping fluids. Once boiling of the fluid has begun, the vapor is forced up the central columns of the jet assembly. It then exits at each downward-directed jet in the form of a molecular curtain that impacts the water-cooled pump body. Here, the vapor condenses and runs back down to the boiler. This refluxing action continues as long as proper heat and forepressure are maintained.

As gas molecules from the system randomly enter the pump (molecular flow conditions), they encounter the top jet. Some of them are correctly impacted and driven on to the next jet. Subsequently they reach the foreline where they are exhausted to the atmosphere by the mechanical backing pump.

The diffusion pump is similar in character to other-compression pumps in that it develops a relatively high exhaust pressure compared to the inlet pressure. This compression ratio for an inlet pressure of $2x10^{-7}$ Torr and a foreline pressure $2.0x10^{-1}$ would be ten million to one for most gases. The speed remains constant from the 10^{-3} Torr scale to the X^{-10} Torr scale and then falls off as a result of the compression ratio for hydrogen and helium plus the vapor pressure contribution of the pumping fluid.

In the same way that the pump must be rough pumped before starting, so must the system to be evacuated by rough pumping prior to exposure to the pump. Exposing a hot pump to a rush of air at atmospheric pressure could be catastrophic for the equipment and possibly explosive depending upon the pump fluid being used.

ION PUMPS

Vacuum pumps in general operate on the basis of maintaining a lower gas density within themselves than exists in the environment they are pumping. This results in a net gas migration into the pump due to the random motion of the molecules under molecular flow conditions. Once in the pumps, few escape and they are either displaced or captured, depending on the type of pump.

Rather than being a displacement pump that actually moves molecules of gas through it to the atmosphere, the ion pump instead captures and stores them. As a result, at some point in time the pump must be cleaned out and renovated. This procedure is generally required only after many years of use.

The generic name is Sputter Ion Pump (or Ion Getter Pump) because some of the gas molecules undergo ionization and cause sputtering of the gettering agent. This material chemically reacts with the active gases to form stable compounds that are deposited on the internal walls of the pump. The getter, usually titanium, is provided initially by a plate or electrode of that material, which is in turn sputtered away by gas ions formed under the influence of the high voltage. These electrical potentials are in the range of 3,000 to 7,000 Vdc.

All ionization devices operate in the same way. Gas molecules enter a field of high speed electrons where some are subject to collisions. In the collision process, a molecule may lose one or more of its own electrons and thereby is left as a positively charged ion. Under the influence of a strong electric field, the ion is accelerated into the titanium cathode. The force of this collision is sufficient to cause very small particles, usually atoms, to be physically removed from the electrode and "sputtered" onto adjacent walls of the pump. This particulate titanium is extremely reactive and will

48

chemically unite with the active gases. The resulting compounds accumulate on surfaces of the pump elements and pump walls.

Active gases are those such as oxygen, nitrogen, CO, CO_2, and water, as opposed to the noble gases like helium, neon, argon, krypton, and xenon, which are non-reactive. The latter are pumped by "ion burial." (ion burial is the "plastering over" of inert gas atoms by the sputtered getter atoms.)

The simplest form of ion pump is the Penning cell, which was originally conceived as a cold cathode vacuum gauge. It consists of a central anode unit upon which is imposed a positive voltage. This anode cell can either be a short section of metal tubing or a square, box-like structure, open at each end like a unit of an egg crate. Opposite each open end is placed a plate of titanium metal that is electrically connected to ground to form the cathode structure. A cell configured in this way is said to be a diode pump. It is then packaged in a suitable high vacuum container and the unit cell becomes a pump with a pump speed of about a liter per second. To make a higher speed pump, it is now simply a matter of making a package containing more cells.

SUBLIMATION PUMPS

Pumping accomplished by coating the inner surfaces of a vacuum system with sublimed titanium films is generally abbreviated TSP (Titanium Sublimation Pumping). Since it involves a chemical reaction, this kind of pumping is useful where mainly active gases are present.

The pumping speed of a unit area varies with various reactive gas species. Cooling the substrate to liquid nitrogen temperature markedly increases the speed for hydrogen and water.

The gases thus "gettered" form stable compounds with titanium and are stored in the system as such until they are removed by cleaning. Since there is generally un-reacted pyrophoric titanium buried in the deposits, caution should be used in cleaning. A typical reaction involving nitrogen is:

$$2Ti + N2 \rightarrow 2TiN$$
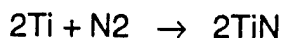
In the case of the Mini Ti-Ball titanium sublimation source, there are 15 grams of usable titanium (atomic weight = 48). This quantity of titanium would be sufficient to react with 4.2 grams of nitrogen (molecular weight = 28). From the relationship $PV = P_1V_1$, that amount of nitrogen would occupy an enormous volume of over 25 million liters at 1×10^{-4} Torr.

The throughput of the titanium film can easily be calculated from $PV = nrT$ where r (the molar gas constant) is 62.36 Torr-liters/mole $K°$, and $T° = 293$. If the source is

49

operated at 52 amperes, it will sublime 15 grams in 20 hours (2.1×10^{-4} grams/sec), and the theoretical throughput will be 3.9×10^{-2} Torr-Liters/sec (theoretical, because in most systems more titanium is sublimed that can be effectively used).

TURBO PUMPS

The turbomolecular pump is a bladed axial flow turbine that compresses gas by momentum transfer from the high-speed rotating blades to the gas molecules. The pump has a rotor (driven by a controller at rotational speeds reaching 75,000 rpm for small pumps) made by a number of slotted disks (typically 10 to 14). These disks are spaced so that between every rotating disk is a fixed disk (stator) whose slots are in the opposite direction. The relative velocity between the rotor and the stator makes it probable that gas molecules will be transferred from the pump inlet to the exhaust, where a mechanical rotary pump, preferably a two-stage type, will finally exhaust to atmosphere.

Each rotor disk is able to support a differential pressure. Because the compression ratio is small for a single rotor/stator stage, it is necessary to use a series of disks: the total compression ratio is the product of ratios obtained by each stage.

The disks near the high vacuum inlet are designed to serve a different purpose from those near the outlet. The blades near the inlet must have high pumping speed and low compression ratio (therefore large incidence angle), while the opposite is true for the blades close to the outlet, which have a small angle. In our pumps there are three different types of blades with angles of 40, 30, and, finally $20°$.

The compression ratio is dependent upon rotor speed, and the molecular weight of pumped gas. This explains why the turbo pump has no backstreaming for oil vapor (heavy masses), and, therefore, doesn't need a trap for operation at any range of pressure. It also explains why the compression ratio for hydrogen and helium are usually given among the major specifications.

The turbomolecular pumps can be driven by two types of controllers, either solid state or rotary converter. The solid state turbo controller converts the single-phase AC line voltage into a 3-phase, medium-frequency voltage suitable for operation of the pump motor. A rotary converter in general is used only in environments with radiation levels not compatible with semiconductors, or with high transient voltage which may occur in plasma fusion equipment, accelerators, etc.

The ultra high vacuum system used to produce platinum silicide that has a load lock has been operating very successfully. The system is stable at a very low vacuum even when platinum is being evaporated. One anomaly is the spectra of the residual gases which shows water vapor at the highest pressure of the residual gases (see Figure III-1). When this system which has been leak checked before is not being used,

the water lines will be leak checked with high pressure gas to see if an extremely minute leak is present.

The ultra high vacuum system used to evaporate iridium has a normal very good residual gas spectrum as seen in Figure III-2.

PART 1

The system used to make ohmic contacts on silicon semiconductor devices was converted from a filament (used aluminum "hair pins") evaporator to an "E" beam gun evaporator (loaded with aluminum plugs).

PART 2

A description of the system is as follows:

A high vacuum system generally includes a mechanical pump, diffusion pump, and cold trap, terminating at a pumping port or manifold port that connects to a bell jar, chamber, or other process vessel. To complete the vacuum system, other components are added to aid or control the action of the pumps. These other components in the 7700 system include a high vacuum valve, port vent valves, and baffle.

The 7700 is an "in-line" high vacuum system, so named because the high vacuum components (pumping port manifold, high vacuum valve, cold trap, baffle, and diffusion pump) are arranged in a straight line to provide the most direct path from the diffusion pump to the pumping port. This assures maximum pumping conductance, which results in high pumping speed and low ultimate pressures.

The sequencing of valves is semiautomatic, with built-in time delays and interlocks to permit operation by a semiskilled operator.

The high vacuum pumping system (see Figure III-1) is designed for rapid evacuation of bell jars into the 10^{-8} mm Hg range. The system can be divided into five basic sections: A diffusion pump system, a mechanical pump, a chamber consisting of a bell jar and hoist, basic system controls, and the cabinetry.

The diffusion pump system consists of a four stage oil diffusion pump with a rated speed of 2000 l/s at its inlet, a water-cooled baffle/cold trap combination, a liquid nitrogen tank for pumping of condensable vapors, a high vacuum valve, a baseplate onto which the vacuum chamber is mounted and the manifolding required to valve the mechanical pump between the foreline of the diffusion pump and the chamber roughing valve. The manifold also includes thermocouple gauges which are used to monitor foreline and roughing pressures, a leak test quick coupling and a vent valve.

The mechanical pump is used to evacuate the chamber from atmospheric pressure to a level at which the diffusion pump can be utilized -- generally in the pressure range of from 1540 to 50 microns.

The system is supplied with an 18" x 30" Pyrex bell jar with implosion shield and a counterbalanced manual hoist for easy trouble-free operation.

The basic system controls consist of a single-lever valve control, two station thermocouple gauge and an ionization gauge control. The control panel includes circuit breakers for the mechanical and diffusion pumps, readouts for the roughing and foreline thermocouple gauges, a vacuum system logic schematic with lights that indicate valve positions, and a single-lever valve control with adequate interlocks and time delays to assure proper sequencing. It controls all functions that are necessary for all pumping operations and is completely fail-safe. The ionization gauge control is connected to a Bayard-Alpert type ionization gauge tube that can be mounted in quick coupling either in the chamber or below the high vacuum valve. It is used to measure pressure over the range of from 10^{-3} mm Hg to 10^{-8} mm Hg.

The cabinet has a welded, formed steel frame with removable sides and lower front panels. The right front racks accommodate three 5-1/4" x 19" rack panel adapters which are used for mounting optional items such as evapatrols, heater power supplies, liquid nitrogen controllers, shutter controllers, fixture drive controls, variable leaks and high vacuum set point controllers.

The left front half of the unit contains the integral valve controller and gauge controls. The diffusion pump is used to reduce system pressure to the neighborhood of 10^{-8} Torr. Fast pumping action is achieved through the use of the high speed oil vapor jets which trap gas molecules and compress them in the direction of the mechanical pump.

The vapor jets are created when the oil pool at the bottom of the pump is heated, causing oil vapor to be forced up the jet stack. The vapor is projected downward and outward by the three upper jets. The high speed vapor jet entrains gas molecules and gives them momentum towards the cooled pump walls, which are externally cooled by water. Upon striking the cooled walls, the vapor is condensed into liquid which then flows back to the bottom pool. The entrained gas molecules are ejected into the foreline by the fourth stage and are exhausted to atmosphere by the mechanical pump. Thus, a continuous cycle of vaporization, condensation, and revaporization takes place. A highly refined low vapor pressure oil (500 cc of DC 704) is used in these pumps.

A diffusion pump has a "limiting forepressure" or "forepressure tolerance" that is an upper pressure limit against which it can exhaust. The mechanical pump provides this exhaust pressure (or forepressure) for the diffusion pump.

The EP-7000 diffusion pump has a rated inlet pumping speed of 2000 l/s for air. The four stage, partially fractionating pump has an inlet diameter of 7-3/4 inches. A thermal switch on the body of the pump is used to cut the power off in case of insufficient water flow. The body of the pump is cooled by one quarter inch diameter stainless steel tubing that is continuously nicrobrazed for optimum heat transfer. The water is fed to the pump from the top and designed so that a thermal gradient exists down the pump wall. The warmer lower portion of the pump casing thus operates at a higher temperature, so that thermal decomposition products are evaporated from the oil and exhausted through the mechanical pump before the oil returns to the boiler.

The jet assembly is spun aluminum for optimum thermal uniformity and all other parts of the body are nicrobrazed or heliarced stainless steel. The second and third jets are covered with shields which catch oil dropped from the lips of the jets above so that it does not drop onto the hot jets and also serves to help trap oil evaporated from the edges of the jets. The fourth stage is an ejector stage which directs gas into the foreline. A foreline baffle is included to prevent oil from passing out of the diffusion pump into the mechanical pump. The boiler is heated by a single 1800 watt pancake type heater which is easily removed from the bottom. Systems are supplied with a charge (500 cc) of DC 704 oil.

A water-cooled baffle (built into the combination baffle and cold trap) is located between the diffusion pump and the cold trap. Backstreaming diffusion pump oil molecules are condensed on the internal water-cooled baffle surfaces and returned to the diffusion pump in the form of liquid oil.

The baffle also helps to keep the refrigerated surface of the cold trap operating at maximum efficiency by acting as a thermal barrier and an intermediate trapping surface between the diffusion pump and cold trap. Otherwise a layer of oil could freeze on the cold trap and reduce trapping efficiency through its insulative action.

The cold trap reduces pressure by condensing or freezing out on its cold surfaces condensable vapors that may exist in the system. Together with a water-cooled baffle it also prevents oil vapor that originates from the diffusion pump from diffusing back into the system. By removing "condensablés", a trap actually serves as a cryogenic pump.

The trap is filled with liquid nitrogen (LN2) after the system has been evacuated to a pressure of less than one micron, when most of the condensable vapors have been pumped out of the system by the mechanical and diffusion pumps. Filling the cold trap prior to the system's reaching a high vacuum condition may result in excessive buildup of condensables (in some cases, ice) that will reduce the effectiveness of the cold trap and retard the attainment of very high vacuum.

The high vacuum valve isolates the chamber from the diffusion pump, water baffle and cold trap. The high vacuum valve is interlocked so it cannot be opened

when the bell jar is at atmosphere. A pressure switch in the roughing line is in series with the high vacuum valve actuator preventing the high vacuum valve from opening until bell jar pressure is roughed below approximately 1 inch of mercury.

The high vacuum butterfly valve has an opening of 7-3/4 inches in diameter and is pneumatically actuated by a rotary actuator. The construction is all stainless steel. Its 90° full opening, 1-5/8" thick low profile design attains the necessary requisite of maximum conductance and minimum surface area to achieve high pumping speeds and low ultimates. A short 7-3/4" diameter stainless steel transition piece is included with a non-magnetic stainless steel baseplate. The all-stainless steel construction assures minimum outgassing and contamination.

A roughing and foreline manifold is designed to valve the mechanical pump between the chamber for roughing and the foreline of the diffusion pump for exhausting the gases compressed by the diffusion pump. The manifold includes mounting positions for foreline and rough vacuum thermocouple gauge heads and a quick coupling type leak detector connection port. Because the manifold is never evacuated below one micron pressure, it is not necessary to construct it of stainless steel.

The roughing and foreline valves have 1-1/2" port diameters for high conductance and are bellows sealed, pneumatically actuated so that they close in case of power failure. A system leak test quick coupling is connected into the foreline of the manifold facing the rear of the cabinet so that the quick coupling extends through the rear service panel for easy access. There are ports in the roughing and foreline sides of the manifold into which thermocouple control tubes are inserted, the high vacuum valve interlock is also connected into this manifold. A 1/4" quick coupling is mounted in the roughing side of the manifold to be used for pumping the cavities in double-pumped rotary feedthroughs.

The mechanical pump is capable of reducing pressure to below 1 micron. A mechanical pump physically "sweeps" the air from a system, usually with a rotary device, which is mounted off center to the pump cavity. The rotating vane (or seep) is kept in contact with the walls of the pump cavity by a compression spring.

Rotating vane positive displacement pumps have large gas handling capacities, but cannot achieve high vacuum. They are used for two purposes: to remove the bulk of air from a system which is initially at atmospheric pressure ("roughing") and, once this is accomplished, to "back" the diffusion pump, since a diffusion pump cannot exhaust against atmospheric pressure. In some applications, two pumps may be used, one for roughing the system and the other for backing the diffusion pump. When one pump is used, it serves two purposes: one, pumping out the manifold during "roughing" operations, and two, providing "backing" for the diffusion pump during high vacuum pumping.

The system is equipped with a 20-1/2" diameter, 3/4" thick stainless steel baseplate. A stainless steel transition piece connects the baseplate to the port of the pumping system. This arrangement raises the baseplate four inches above the cabinet table top and provides convenient accessibility to the underside of the baseplate.

The Bell Jar Hoist is a manual counterbalanced type. The counterweight is within the support mast and is connected by a steel cable via pulleys to the top of the bell jar. The bell jar is guided by two guide rods and is self aligning with the base plate.

All valves are controlled by a single valve control lever located on the front panel. While the system still essentially is manually controlled, interlocks and time delays are built in to assure fail-safe operation by a semiskilled operator. All valve states are clearly displayed on a front panel vacuum schematic.

The baseplate of the system was removed and sent out to be electropolished, the feedthrough ring was also sent out for electropolishing. The gun mount was designed and a limited number of the "e" beam power supplies were mounted. The operation of the power supply is as follows:

The TT-15 Electron Beam Power Supply uses a conventional 3-phase high voltage transformer and fullwave semiconductor rectifiers to deliver raw rectified negative high voltage DC to a filter capacitor and a resistance bleeder. The positive connection is delivered to the regulator tube.

The unregulated high voltage is fed to a tetrode series regulator controlled by a reference signal taken from a feedback voltage divider.

The total emission current is monitored and the control objective changes from regulated voltage to regulated current if a pre-set current value is exceeded (current cutback).

The system is operated so that the emission current is limited by the temperature of the electron gun filaments (determined by filament current), rather than depend on control of the high voltage. The control signal for the electron gun filament is derived from measuring the emission current in the high voltage line with a current sensor. (The current sensor measures current by sensing the magnetic field around the HV line and allows safe isolation from the line.) A single gun power supply may use the current sensing resistor (R13 in the cathode circuit of the tetrode tube) to sense the gun current. This resistor is used for overall current sensing in all power-supplies.

In a practical vacuum evaporation system, the evaporant crucible cannot be located in a line sight position with regard to the filament; contaminant positive ions would bombard the negative filament and destroy it. A magnetic field beam-bender is required to bend the electron beam to the evaporant crucible. Heavy ions do not follow

the same curved path as the electrons. The beam bender also is used to focus the beam and to move the beam over the surface of the evaporant material in the crucible.

PART 3

OHMIC CONTACTS

The majority of contacts are now made in a conventional vacuum system by evaporating the metal onto a semiconductor surface prepared by cutting, polishing, and etching, although it is becoming increasingly common to use a very-high-vacuum system fitted with an ion pump. Such contacts invariably contain a thin oxide film between the metal and semiconductor and are therefore not ideal, but they are sufficiently near to the ideal for most practical purposes.

An ohmic contact is defined as a metal-semiconductor contact that has a negligible contact resistance relative to the bulk or series resistance of the semiconductor. A satisfactory ohmic contact should not significantly degrade device performance, and it can pass the required current with a voltage drop that is small compared with the drop across the active region of the device.

As normally used in semiconductor technology, the term "ohmic contact" means one for which the I/V characteristic is determined by the resistivity of the semiconductor specimen or by the behavior of the device of which the contact forms part, rather than by the characteristics of the contact. It is not essential that the I/V characteristics of the contact itself is linear, provided its resistance is very small compared with the resistance of the specimen or device. In addition, the contact should not inject minority carriers and should be stable both electrically and mechanically.

An important property of an ohmic contact is its specific resistance (resistance multiplied by area). A good ohmic contact should have a specific resistance of less than about 10^{-9} Ω m^2. The specific resistance R_c can be found by measuring the total resistance of a circular contact of diameter d on a slice of semiconductor of thickness t and resistivity ρ. The total resistance R_{tot} is given by

$$R_{tot} = \frac{\rho}{\chi d} \quad \tan^{-1} \frac{4t}{d} \qquad \frac{4R_c}{\chi d^2} \qquad R_o$$

where R_o is the resistance of the contact on the face of the slice (assumed to have infinite area).

The fabrication of ohmic contacts is still more of an art than science, and every laboratory tends to have its own favorite recipes which involve particular metal or alloy systems, particular deposition methods, and particular forms of heat treatment.

All the recipes appear to depend on one or other of the following three principles:

1.   If the semiconductor is one which conforms approximately to the simple Schottky-Mott theory, it should be possible in principle to obtain a contact with a negative barrier height (which should behave as an ohmic contact) by finding metal with a work function less than the work function of an n-type semiconductor or greater than the work function of a p-type semiconductor. Alternatively, if the barrier height is determined by Fermi-level pinning, it occasional results in a pinning position that is within the conduction band or valence band, in which case negative barrier heights should be obtainable on n-type or p-type semiconductors, respectively. The ohmic contact formed by gold on indium arsenide seems to operate in this way (Walpole and Nill, 1971). Unfortunately, there are very few metal-semiconductor combinations with this property, though if the barrier height is positive, but very small, the contact should have a low enough resistance to be effectively ohmic.

2.   The vast majority of ohmic contacts depend on the principle of having a thin layer of very heavily doped semiconductor immediately adjacent to the metal. The depletion region is then so thin that field emission takes place and the contact has a very low resistance at zero bias.

3.   If the surface of the semiconductor is damaged (for example by sandblasting), crystal defects may be formed near the surface which act as efficient recombination centers. If the density of these is high enough, recombination in the depletion region will become the dominant conduction mechanism and will cause a significant decrease in the contact resistance. This method is of mainly historical interest; it was widely used during the early days of semiconductor research for making contact to silicon and germanium, the actual contacts being obtained either by soldering or by the application of pressure.

The UHV system used to evaporate iridium to form silicides has a small water leak in an "o" ring seal. The total pressure is 2.0×10^{-7} and the air spectra high mass 28 due to N_2 and a peak at 32 due to O_2 as well as a high peak at mass 40 due to argon (see Figure III-1). (N_2 is molecular nitrogen, O_2 is molecular oxygen and A is Argon.)

Figures III-2 and III-3 are analog spectra of Figure III-1. The peaks are as follows:

mass 2 is hydrogen, mass 4 is helium, mass 14 is doubly ionized nitrogen, mass 16 is oxygen, mass 17 is OH radical, mass 18 is water vapor H_2O, mass 20 is doubly ionized argon, mass at 28, 29 and 30 due to nitrogen and its isotopes and the last peak at 40 due to argon.
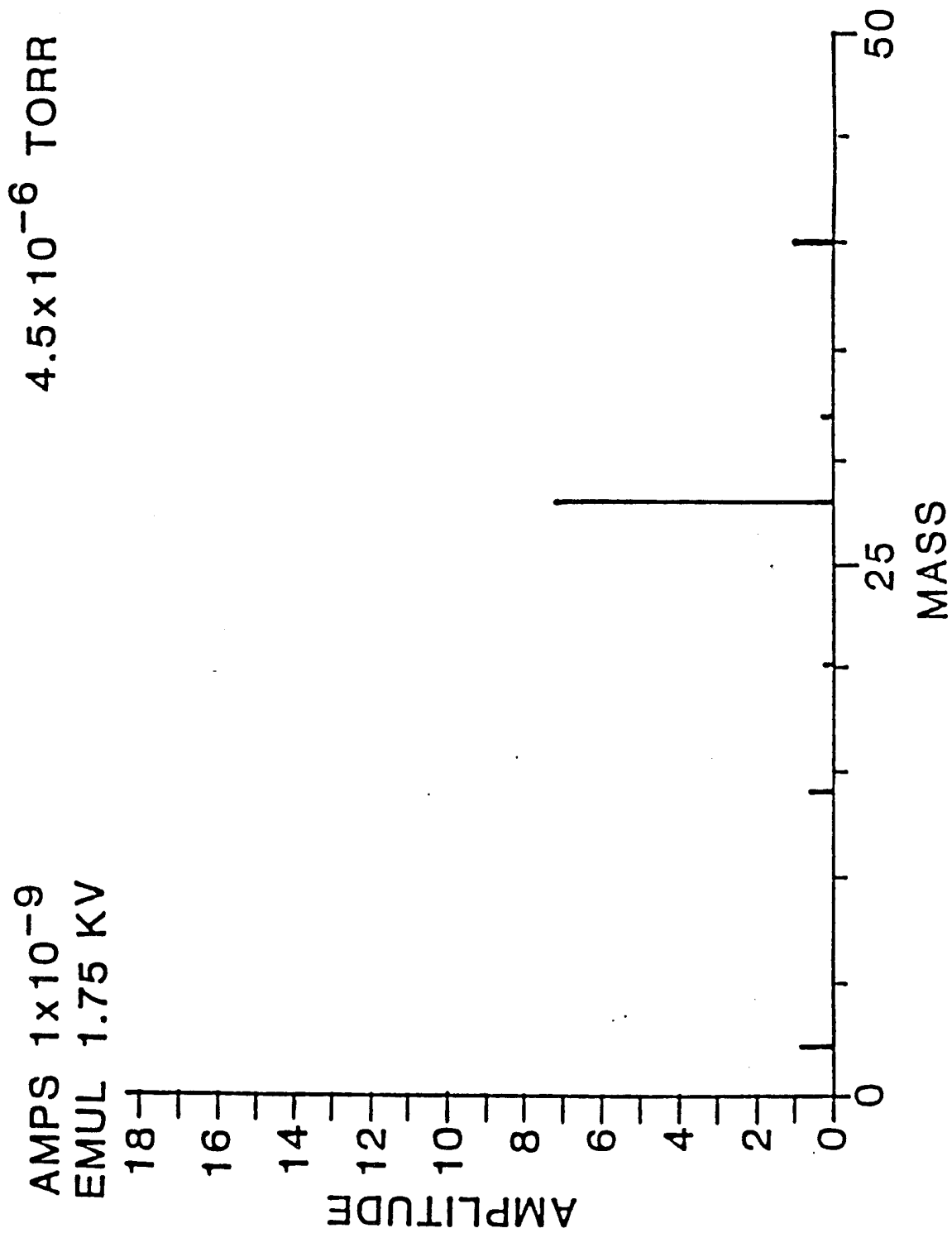
FIGURE III-1

FIGURE III-2

59

AMPS 1×10^{-9}
EMUL 1.75 KV

4.0×10^{-6} TORR
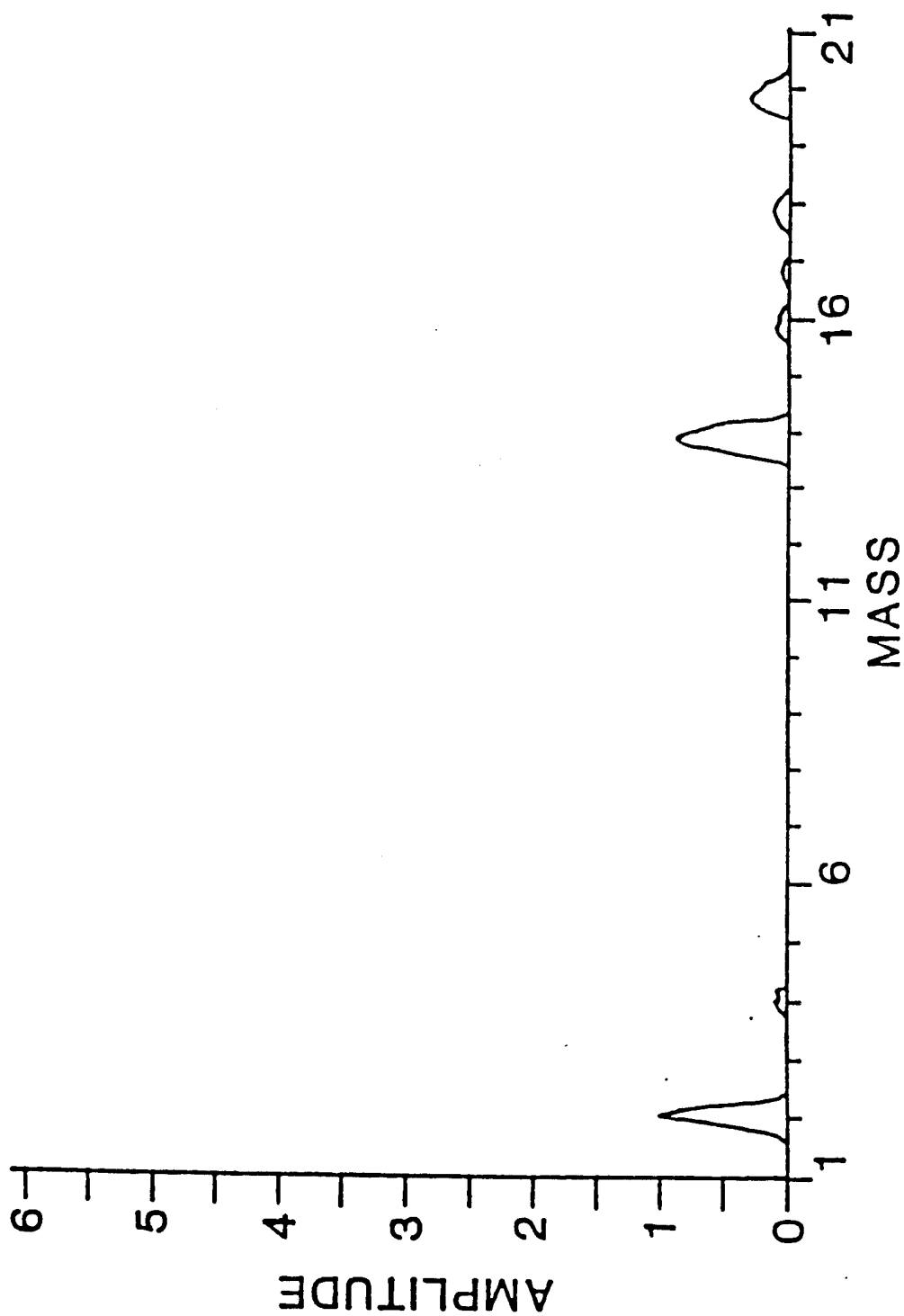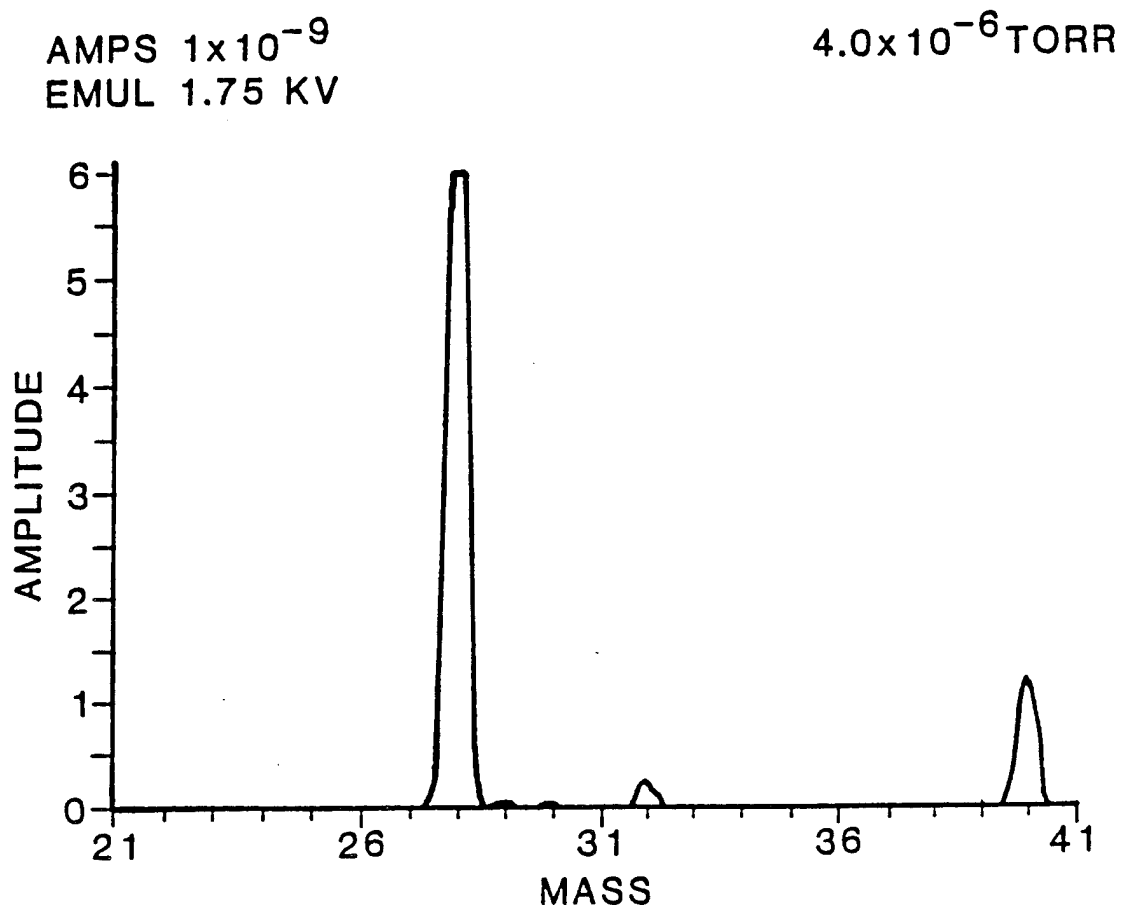
FIGURE III-3

SUMMARY

During this reporting period 40 crystal growth runs were carried out. Indium Phosphide doped with Fe,Cd,Sn,S and Rh was grown and a method for S doping was developed. Growth conditions were improved leading to a reduced incidence of twinning and a modification to the seeding procedure was introduced. Crystal growth utilizing phosphorus and indium obtained from a number of different sources was investigated.

Methods for controlling the in-situ phosphorus injection synthesis of InP were developed leading to markedly improved repeatability and a melt stoichiometry close to 50 mol% P.

High temperature outgasing of the furnace prior to loading led to improved visibility by reducing the deposition of contaminants on the transparent fused quartz heat shields and convection barriers.

A recirculating water to chilled water heat exchanger was installed to replace direct connection of the furnace chamber to the chilled water supply. Condensation of moisture on the furnace, especially on humid days, has been eliminated. Internal water pressure and temperature limit switches in the RF generator were replaced, reconnected and wired in series with a flow switch in the furnace coolant circuit. These safety devices make it possible for the furnace to be powered overnight while unattended.

RF load coil design was improved. Teflon centering spacers were developed for accurate positioning. A dual section coil was built to heat a secondary susceptor to provide additional power to the injector and to reduce phosphorus deposition on the quartz heat shields.

General maintenance was performed as necessary.

CRYSTAL GROWTH

INTRODUCTION

Indium phosphide crystals were grown by the MLEK method using the standard procedures developed by PML and RL personnel. For runs in which InP was synthesized in situ by phosphorus injection, 800 g of In and four 40 g RASA type D B_2O_3 cylinders were used. Crucibles were either fused quartz or pyrolytic BN ~3.8" ID. Dopants were added in elemental form. One exception was S which will be discussed below. Generally the seeds were <100> although <111> crystals were occasionally grown. For the injection runs, the previously developed side tube style injector was used. Crystal growth runs were also carried out utilizing remelts of previously synthesized charges or from a charge prepared from selected cuttings of previously grown crystals.

The purpose of these runs was multifold: to advance the technology of one step in situ synthesis and growth of InP and to improve the flat top growth (Kyropulos) method with the goal of reducing the cost, increasing the per crystal yield of wafers and improving the purity of the product by minimizing the handling and processing that is inherent in the commercial multi-step process. The improved technology will have potential for transfer to the commercial sector.

GROWTH CONDITIONS

It is necessary to have favorable thermal gradients to be able to grow twin-free single crystals. The main parameter investigated was the melt level position relative to the RF coil and insulation stack. Figure IV-1 illustrates these relationships. [Note: Figure IV-1 was produced on the Macintosh to 1/2 scale but has been further reduced for printing on one page. Objects that move together in the furnace are grouped on the drawing so that when displayed, may be translated up and down as in the furnace.] The furnace was set-up with the top turn of the RF, measured between the leads, positioned 1" below the top of the insulation stack and the top of the susceptor was adjusted to be level with the selected reference point on the coil. This defines the zero position of the susceptor. Positioning of the susceptor for the different operatons carried out, injection,

cleaning cycle and seeding was done relative to this point. The susceptor is positioned at a level above zero for crystal growth. Development of faceting or twinning as the flat top of the crystal expands from the seed depends upon the position selected. Over many growth runs, variations in position were qualitatively investigated. Starting the growth at a position about 2.5 cm above zero was generally successful at minimizing twinning. Other improved growth conditions relate to centering of the RF coil, which will be discussed below.

SEEDING

Seeding is the process by which a new crystal is nucleated on an oriented piece of previously grown material. Seed were 1/4" x 1/4" x ~2" bars. The melt temperature was adjusted so that the liquidus isotherm passed through the seed just above the surface of the melt. Since this temperature could not be measured directly, we had to rely on the base thermocouple to provide a reproducible reference temperature. Final adjustment to the seeding temperature was based on a visual observation of the meniscus at the seed melt interface. In some groups of successive runs, the base thermocouple which had been reading correctly appeared to indicate a temperature as much as 150° lower than we believed it to be. Due to these variations, it was not always possible to rely on this measurement for setting the seeding temperature. Instead, the process setpoint or the power calculated from the RF plate current and voltage was often a better indicator of melt temperature. The technique of dipping the seed into a slightly cold melt was introduced. In this method, the melt temperature is allowed to stabilize before it is increased to melt back the seed till the meniscus assumes a circular shape slightly smaller than the seed diameter. The amount of meltback and the initial temperature lowering rate can be controlled when this process is utilized. There has been no indication that randomly nucleated material that might have formed on the seed as a result of the cold dip has remained or interfered with crystal growth. According to the procedure in use earlier, the seed was contacted to the melt at a temperature slightly higher than required with the express purpose of melting off or melting back a few millimeters of material. If the contact did not melt off within a minute or two and it was determined that the temperature was sufficiently high, a temperature lowering ramp was begun. Under these conditions, the melt temperature was often still changing in response to a previous set point change. Seeding was therefore done under transient

63

conditions with no control over the amount of meltback or initial growth rate. The older method has not been abandoned and is utilized when the first estimate of seeding temperature is too high.

BASE THERMOCOUPLE

To understand the origin of the thermocouple error a number of tests were done. Calibrated outside the furnace, the accuracy was found to be within a few degrees. The base thermocouple is postioned in a well located on center in the bottom of the graphite susceptor. It is positioned to within 1/16" of the bottom of the well. The sheath of one thermocouple was removed to show the position of the bead. It is isolated from ground and spaced from the end of the sheath as shown in Figure IV-2. The observed error may be due to positioning, but this has not been confirmed.

SULFUR DOPING

Repeated attempts to dope InP with sulfur starting with elemental S were marginally successful for both P injection and remelt runs. There appeared to be some attack on BN crucibles and possibly on quartz as well. There was also a loss mechanism that resulted in deposition of a residue on the quartz convection shielding above the susceptor that could not be removed in the usual in situ cleaning cycle. Only traces of S were found in the crystals. The use of In2S3 in place of S was suggested and found to be more successful. The interfering deposits did not form and axial slices of a crystal inspected under the infrared microscope showed a prominent striation pattern indicating significant S incorporation. Growth of the In2S3 doped crystals was characterized by prominent faceting during expansion of the crown accompanied by extensive twinning. Similar behavior was not observed when elemental S was used as the dopant.

RAW MATERIALS

Rectangular In billets rated at 6,9s and 6,9's5 pure were obtained from Indium Corporation of America and 7,9's billets and 7,9's split disks from Arconium were used in various runs. The advantages of one type or purity over another have not yet been

demonstrated. However, it appears that the split disk type may be contaminated with material that floats to the InP melt surface. Crystal growth from melts prepared from this lot of indium were heavily twinned.

Phosphorus with a rated purity of 6,9's was obtained from Mitsubishi Materials Corp. and from MCP Electronic Materials, Ltd. The Mitsubishi material consisted of ~one milimeter sized grains and fines, while the MCP phosphorus was made up of larger chunks some measuring nearly one cm in two dimensions. The latter material was not entirely easy to load into the injector as larger pieces would lodge in the transfer tube. Otherwise, the behavior of both materials was similar and the differences in particle size and packing did not require changes to be made to the injection procedure.

Type D B2O3 containing ~125 ppm water in the form of 25mm dia x 50 mm long cylinders was used in all the growth runs.

INJECTION SYNTHESIS OF INP

In situ synthesis and growth is the key procedure that distinguishes InP crystal growth at RL from growth elsewhere. InP is synthesized in situ by injecting P vapor into molten In above the melting point of InP. Injections are carried out under a pressure of ~630 psi of nitrogen. After a crystal growth run is completed, the success of the injection is evaluated in terms of the stoichiometry of the InP melt produced from the mass of the injector, P, In, B2O3, seed, crucible and susceptor loaded into the furnace and the mass gain of the combined crucible susceptor, B2O3, and crystal produced at the end of the run. The mass of P remaining in the injector and the mass of P lost to the furnace is also estimated. A successful injection synthesis yields a melt with stoichiometry near 50 mol% P, a small loss to the furnace and a minimum of P remaining in the injector. An unsuccessful injection may be characterized as yielding a melt that contains insufficient P for untwinned single crystal growth or as releasing too much phosphorus to the furnace in which case not only will the melt be In rich, but also the visibility required for control of crystal growth will be compromised or completely lost. In the worst case, the injector explodes, damaging the furniture and creating a difficult clean-up job.

Work during this period consisted in investigating the parameters that affect injection and developing an experimental approach to increase the process reproducibility, give a near stoichiometric melt and reduce the amount of P lost to the furnace. A record of injection performance as a function of Run# is shown in Figure IV-3. It can be seen that over a period of time, injection reproducibility has improved and the mole fraction of P has generally become closer to 50%. Gaps in the plot indicate injector explosions, while gaps in the sequence of Run #s represent runs not completed for some other reason or execution of non injected runs. The sharp drop in mol% P at # 4044 is an outlier and the low value at Run#4047 occurred when a new type of RF coil was installed. Figure IV-4 shows the phosphorus loss to the furnace as a function of Run #. The trend is to lower values with increasing Run #. This reduced P loss in recent runs has resulted in markedly improved visibility. The achievements resulting from the experimental investigation of the injection process have been development of a procedure that gives improved reproducibility, stoichiometry above 48% to slightly higher than 50% and a reduction in P loss to the furnace.

Attempts to correlate melt stoichiometry with injection parameters were made, time span of the injection, maximum temperature of the injector, the amount of P remaining in the injector and the amount of P loaded among them. Figure IV-5 illustrates the injector, crucible with a charge and heater annotated with various operator controlled parameters.

To start the process, the transfer tube is lowered when the injector temperature indicates ~250°C, into the molten In which has been heated to a temperature above the melting point of InP as indicated by the base thermocouple. To mix the melt, the crucible is rotated at a few rpm. The system power is raised in steps to drive temperature rise of the injector.

Indicators of the course of the injection are visual observation of P vapor bubbles on the surface of the In/InP melt as they emerge from the transfer tube and temperature rise of the injector. The base temperature is also noted. When the position of the transfer tube is optimal, it is possible to see whether it is clear or whether it contains InP that has formed when the melt has been sucked back. Phosphorus bubbles are either absorbed by the melt, or when the rate of generation is too high, escape from the surface of the B2O3 producing a puff of smoke. A low incidence of P escape, which is not a serious diversion from the In/InP melt is an antecedent of the more rapid phase

of P release. This phase of the injection is characterized by P smoke that fills the furnace chamber and completely obscures the view of the melt surface. The injector and base temperature rise rapidly at this time, probably as a result of reduced thermal loss. Over a period of time the smoke clears and visibility is restored. As this occurs, the injector temperature briefly levels off and begins to fall, signaling that InP will be sucked into the transfer tube where it will freeze creating the potential for an injector explosion if it is further heated. Generally the injector is withdrawn from the melt at this time, terminating the synthesis.

Onset of dense smoke phase is rapid, occurring within one or two minutes of the first indication on the injector thermocouple of an acceleration of the temperature rise. Response of the injection rate to changes in furnace power are too slow for this variable to be effectively used in controlling excessive P release once it has started. Response to injector position is more rapid and some control can be exercised but a lag still exists between appearance of smoke and its regulation.

The negative effect of excess P loss is diminished visibility. Some P remains on the view tubes and there is significant contamination of the quartz shield. Reduced stoichiometry is by far the most important effect. The quartz shield can be cleaned to an extent by lowering the susceptor into the insulation stack for a short period of time. Loading the injector with a large excess of P is to be avoided as any additional contamination of the quartz cylinder would make subsequent crystal growth very difficult.

Injector temperature as a function of time was plotted for a number of runs to characterize the process to determine which parameters for achieving a high stoichiometry. Figure IV-6 shows the profiles of a number of representative runs. The point on the curves where there is sharp upturn in slope corresponds to appearance of P smoke. The sharp downturn at the end of the curve indicates withdrawal of the injector. It appears that the time span and slope of a given injection or the maximum temperature are not sufficient indicators of a high stoichiometry. The effect of excess P was not taken into account and no attempt was made to correlate the amount of P released to the furnace with the slope or integral of the injector temperature curve. The data does suggest that if the temperature rise could be maintained 5 and 20°C/min, a high stoichiometry would be obtained. An effective method for temperature control

would also avoid the sharp rise associated with onset of excessive P release to the furnace.

A procedure for slope control was developed based on modulating the temperature rise by raising or lowering the injector from its starting position by 1 or 2 mm. The response of the injector to these changes was rapid and occurred within a minute or two after the change was made. The power level was also changed if operator judgement indicated that it was too high or low. That decision was based in part on the temperature of the melt and how fast it was changing. The slope was manually estimated from the temperature trace plotted on Omega data logger strip chart. Having the Omega calculate and plot the slope was not workable as the time constant for this function was too long compared to the rapid changes in injector temperature and the data was difficult to read. Most recently, a PC was interfaced to the data logger allowing slope and other variables to be displayed and printed to files.

Figure IV-7 shows the injector temperature, susceptor base temperature, injector position and power settings and rate of change of the injector temperature as a function of time for Run# 4040 in which a stoichiometry of 50.1% was obtained. The data was read from the strip chart recording. During the run, the slope was graphically measured. The estimate of P excess calculated from the mass balance was confirmed by observation of P containing blow holes in the bottom of the crystal and in the residual melt.

With the computer in place, a reliable and current value of the slope was always visible. In Runs 4054 and 4055 the slope was in the 5°C/min range. Although good control of P loss was maintained, the amount of smoke was minimal, and stoichiometry was high, the injections took too long. In these runs, the balance between injector position and power in modulating the injector temperature slope favored power and as a result, toward the end of the process the crucible temperature may have been too high. Factors that come into play but have not been investigated in more than a qualitative way are position of the entire susceptor-injector unit within the coil and insulation stack and crucible rotation rate. The positioning affects the thermal characteristics of the system and influences the relative temperature of the In/InP melt and injector. It is assumed that the concentration of InP is greatest near the mouth of the transfer tube which slows the rate of P reaction especially when the melt stoichiometry is high. P escape from the melt may be a sign that liquid is locally

saturated. There is an indication that increasing the rotation rate of the crucible results in an increased rate of P reaction through increased mixing of the melt but more work needs to be done to characterize this behavior.

Variations in the physical dimensions of the injectors have worked against achieving good run to run repeatability. As we have established, the rate of injector temperature rise is very sensitive to injector position. Variations of several mm in the length of the transfer tube measured from the bottom of the injector were common in the past. The length of the injector body also comes into play as this dimension influences the size of the uninsulated area. Injectors that are too long are not heated as effectively. Through more attention to quality control these variations have been reduced.
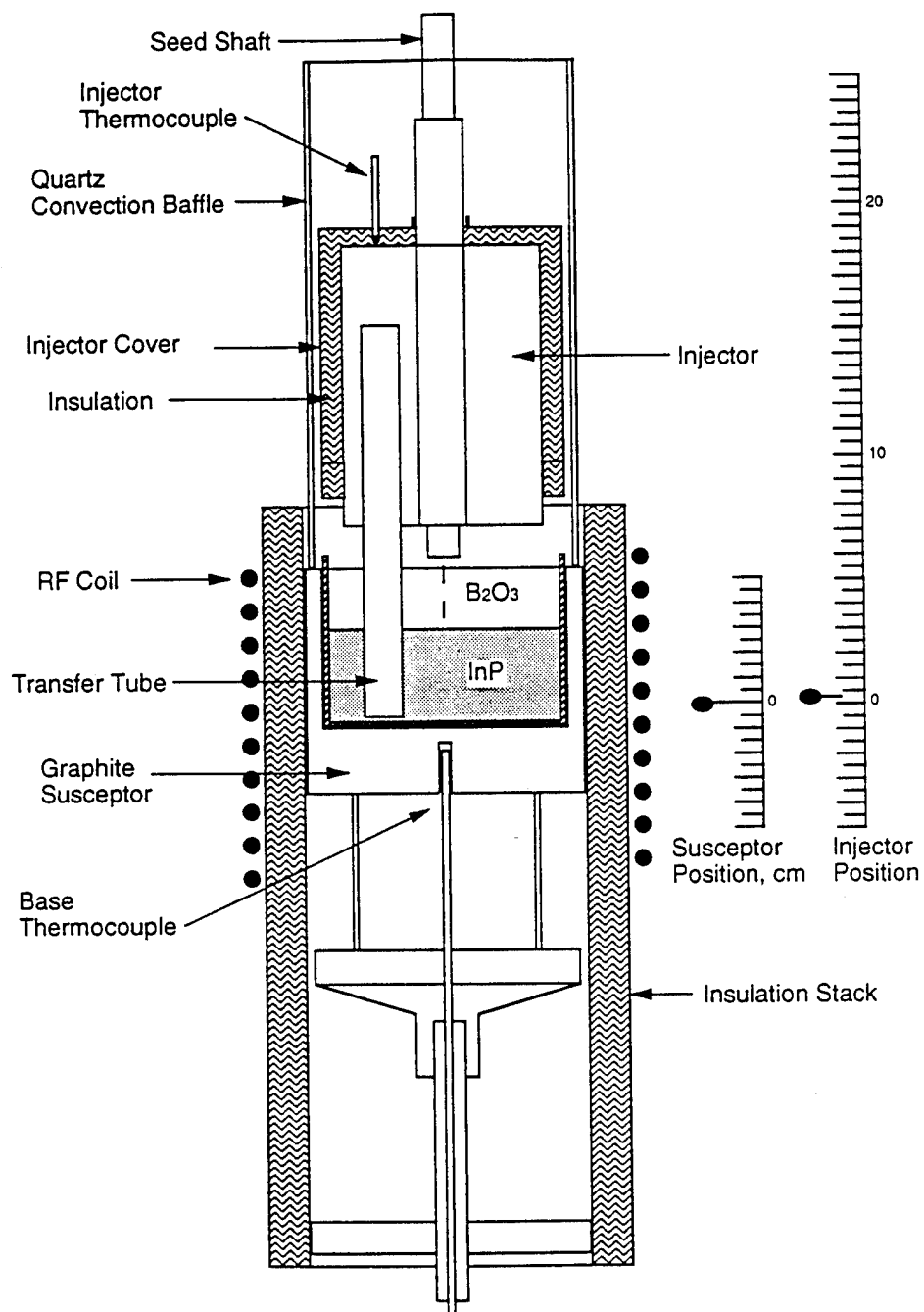
RF COIL DESIGN

To maximize the amount of phosphorus transferred from the injector, it is necessary to heat the upper portion to ~700°C. Under this condition all of the P will be gaseous, and the amount present will be determined by the volume of the injector and pressure. A rough calculation indicated that at under the injection conditions, a mean injector temperature of 1000°K at 42 atm we may expect ~30 g of P to remain in the injector. The target temperature for the injector top is difficult to attain without overheating the melt when the main susceptor is the only heat source.

A dual coil design was developed to heat a second susceptor located near the top of the injector in addition to the primary graphite crucible holder. Figure IV-8 shows the dual coil and upper secondary susceptor in relation to the injector. The upper susceptor, which is a graphite ring, is supported by a three legged fused quartz pedestal which rests on the quartz separater disk atop the insulation stack. The graphite ring is backed by ceramic felt insulation. The coil was wound from 1/4" copper refrigeration tubing. Copper soft solder fittings were used to join the various segments. Three Teflon wings extending to the furnace walls were tied to the coil with high temperature glass tape. The wings space the coil to a uniform pitch and center the coil in the furnace. This feature allows the coil to be mounted and demounted for cleaning with relative ease. Centering on the susceptor is accurate and reproducible.
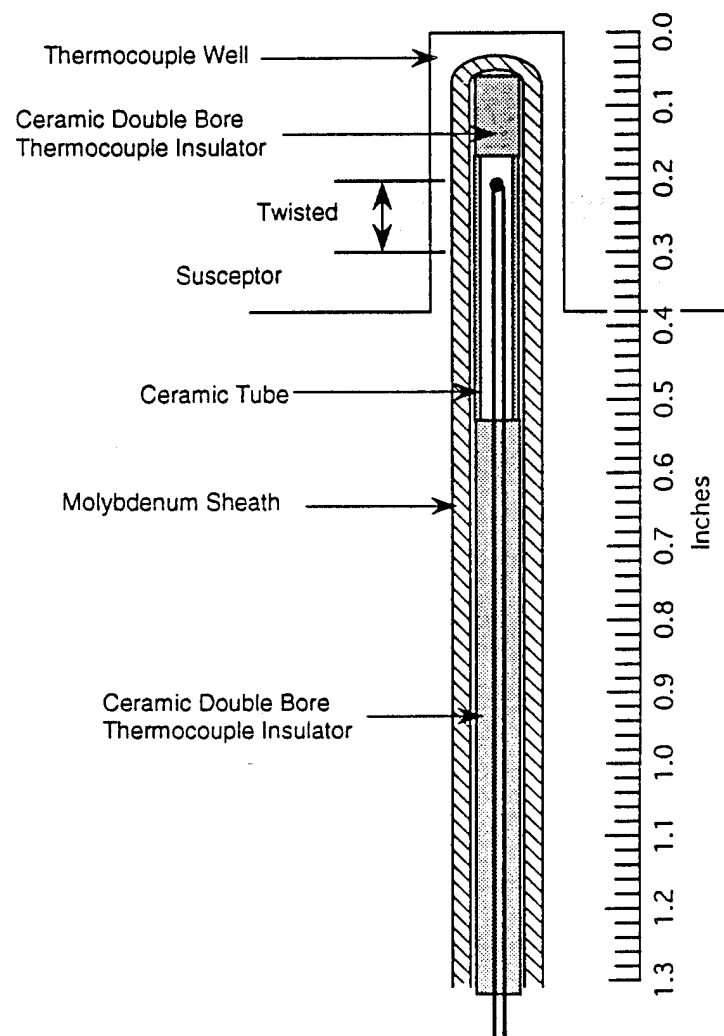
In addition to heating the injector, it was also expected that the upper susceptor would provide enough heat to prevent deposition of P on the quartz heat shield or quartz dome that is utilized in remelt runs. The performance of the coil did not fully meet expectations. The temperature reached by the upper susceptor was judged by eye to be between dull and mid red heat when the base temperature was between 1100 and 1200°C. The variation depended upon positioning of the upper segment which was adjusted with a BN spacer. Additional heating of the injector was not characterized, and the melt stoichiometry did not show a marked improvement over that obtained with the single segment coil used earlier. Phosphorus deposition on the quartz shield or dome was reduced, but mainly in a band adjacent to the upper susceptor.

The principle advantages of the new coil over the type used earlier are its accurate pitch and centering, its light weight, the ease with which it is installed, and the ease with which it is demounted and cleaned.
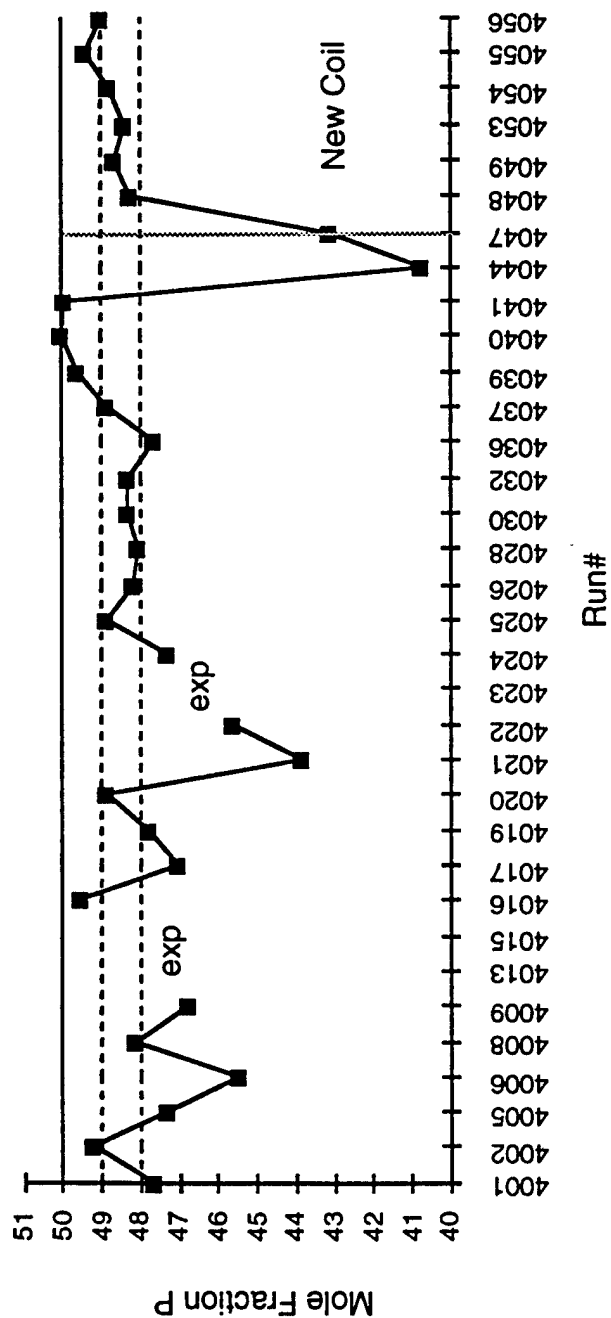
Seed Shaft

Injector
Thermocouple

Quartz
Convection Baffle

Injector Cover

Insulation

Injector

RF Coil

B_2O_3

Transfer Tube

InP

Graphite
Susceptor

Base
Thermocouple

Susceptor
Position, cm

Injector
Position

Insulation Stack

Relative position of melt level, coil, injector and insulation stack.

FIGURE IV-1

Thermocouple Well

Ceramic Double Bore
Thermocouple Insulator

Twisted

Susceptor

Ceramic Tube

Molybdenum Sheath

Ceramic Double Bore
Thermocouple Insulator

Inches

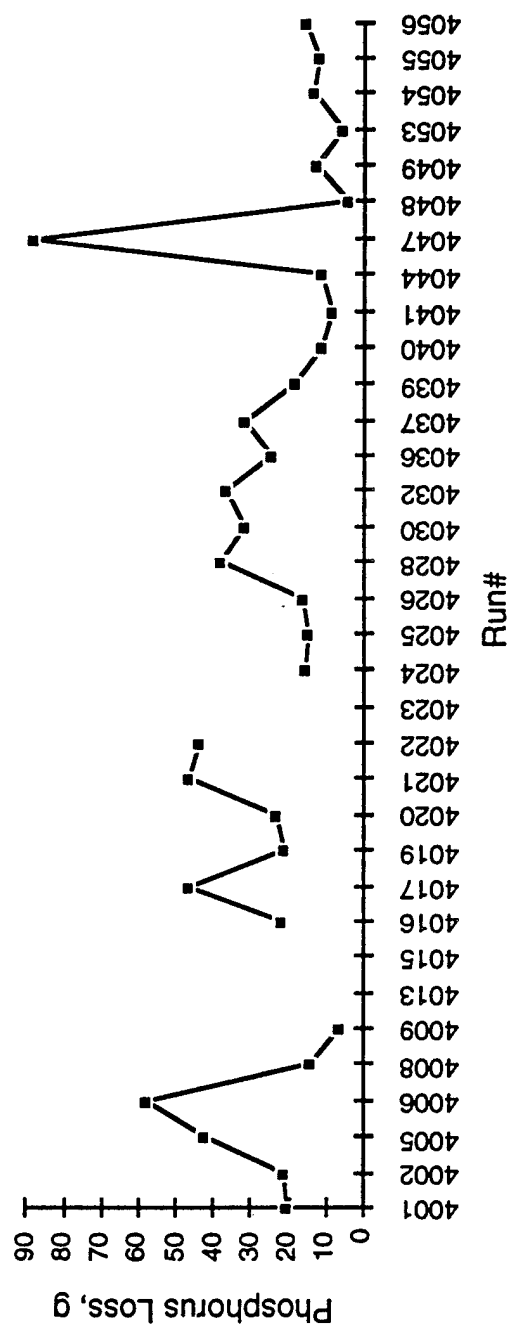0.0 0.1 0.2 0.3 0.4 0.5 0.6 0.7 0.8 0.9 1.0 1.1 1.2 1.3

Thermocouple bead position within susceptor well. 5x Scale.
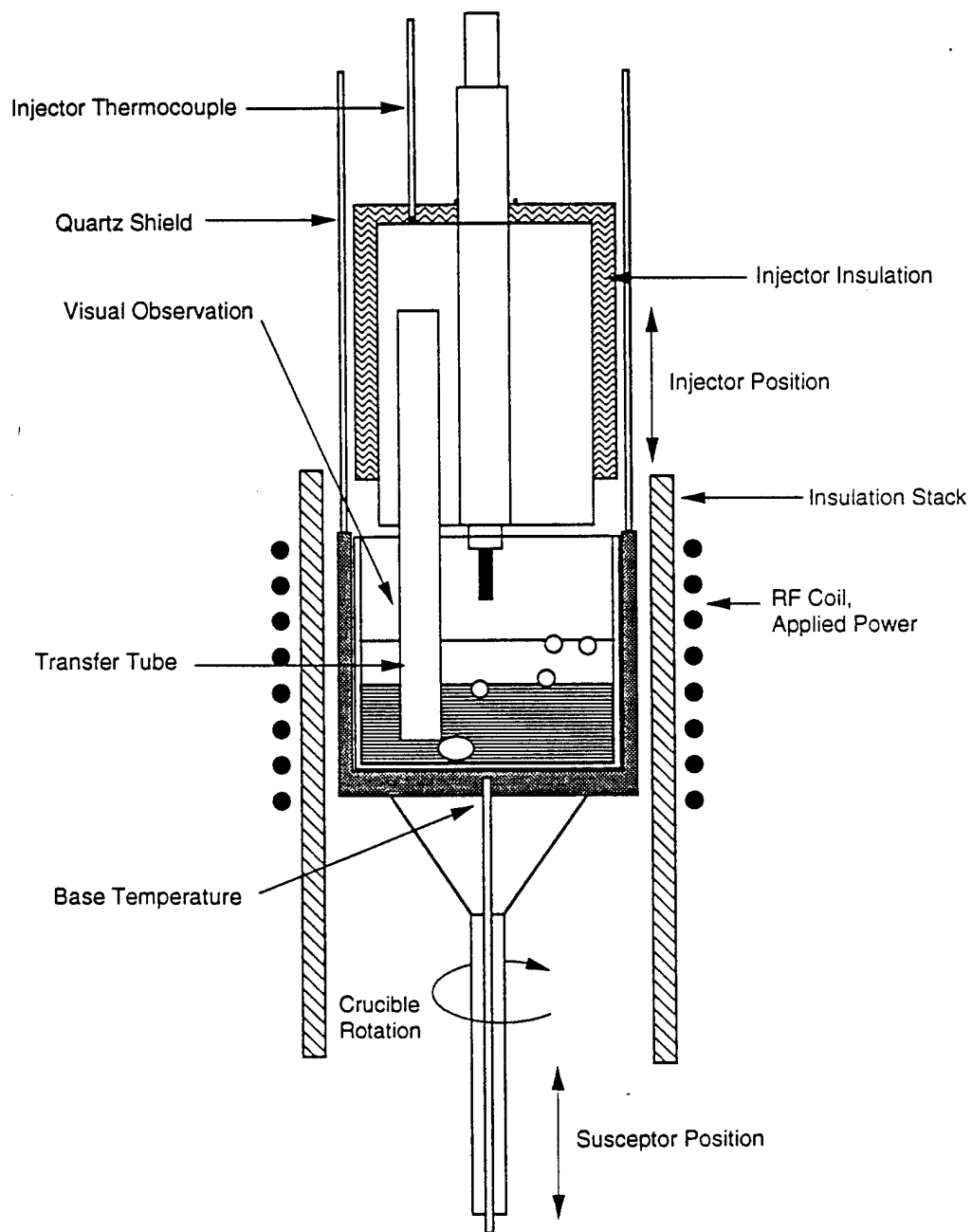
FIGURE IV-2

Melt stoichiometry as a function of Run#. (exp= injector exploded)

FIGURE IV-3

73

Phosphorus loss to the furnace as a function of Run #.

FIGURE IV-4

Injector Thermocouple

Quartz Shield

Visual Observation

Injector Insulation

Injector Position

Insulation Stack

RF Coil,
Applied Power

Transfer Tube

Base Temperature

Crucible
Rotation

Susceptor Position

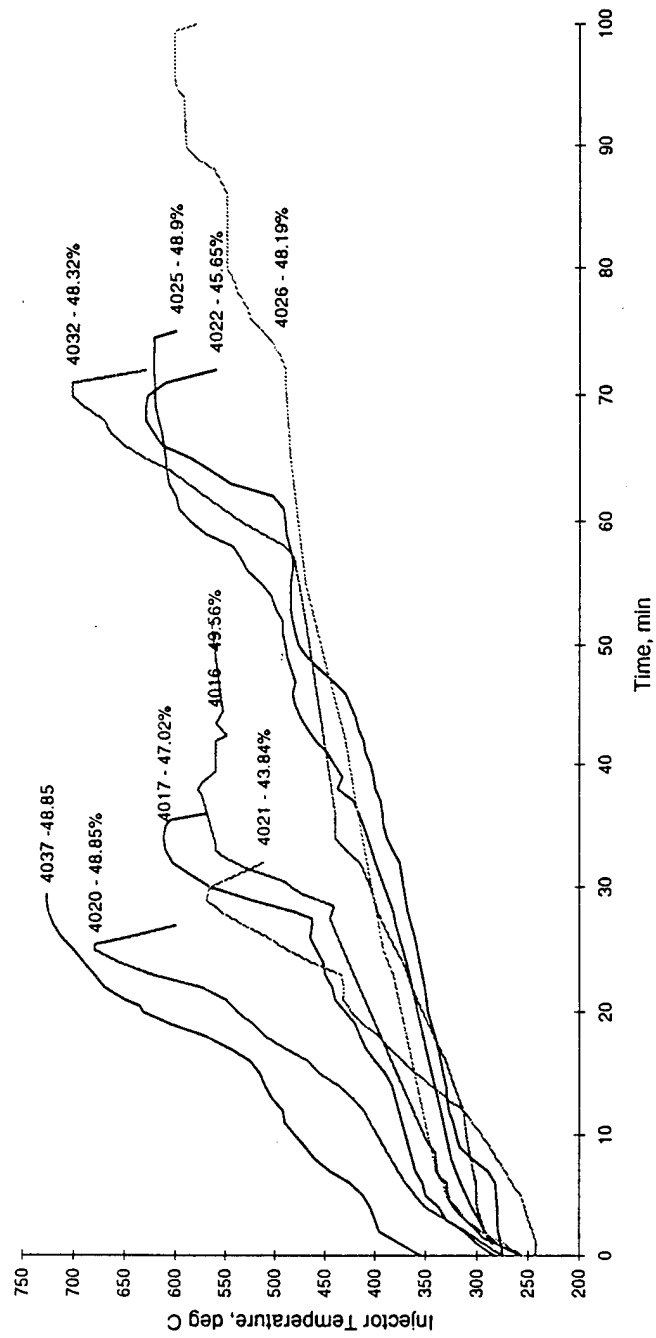Injector with operator controlled parameters.
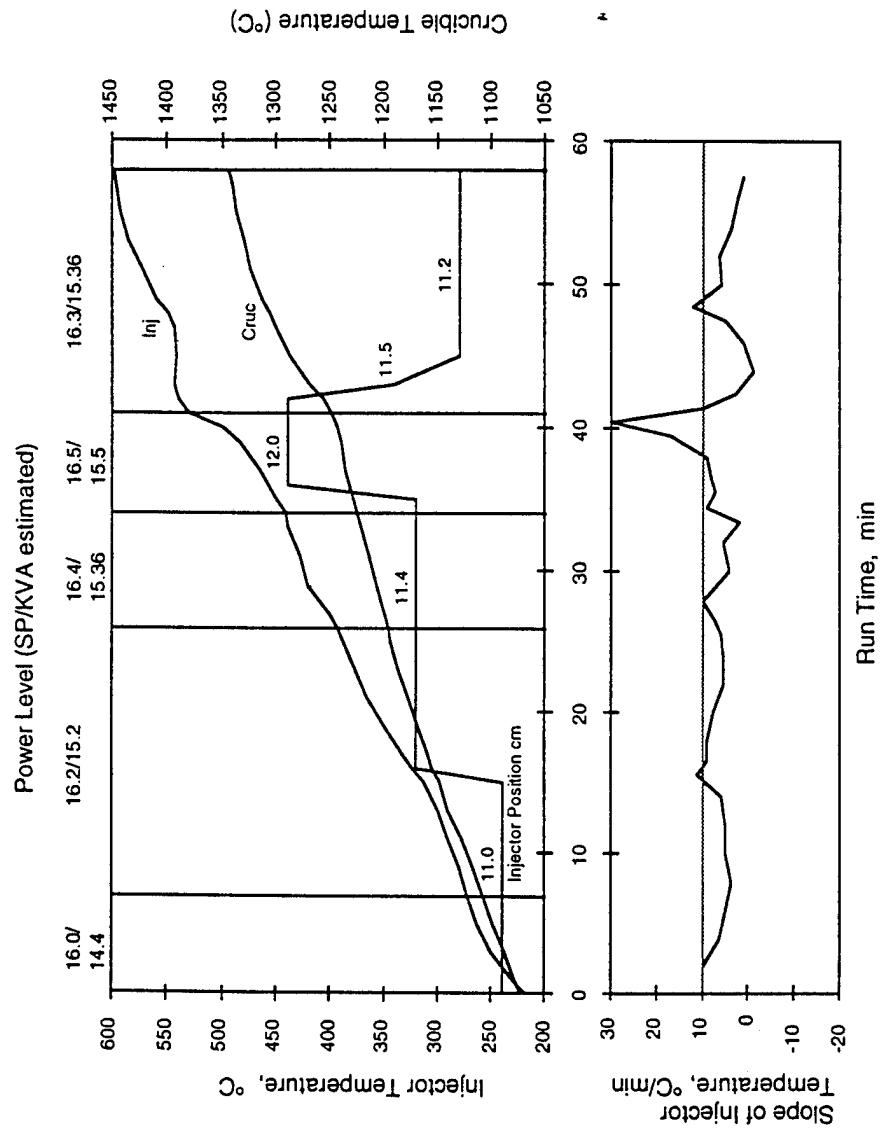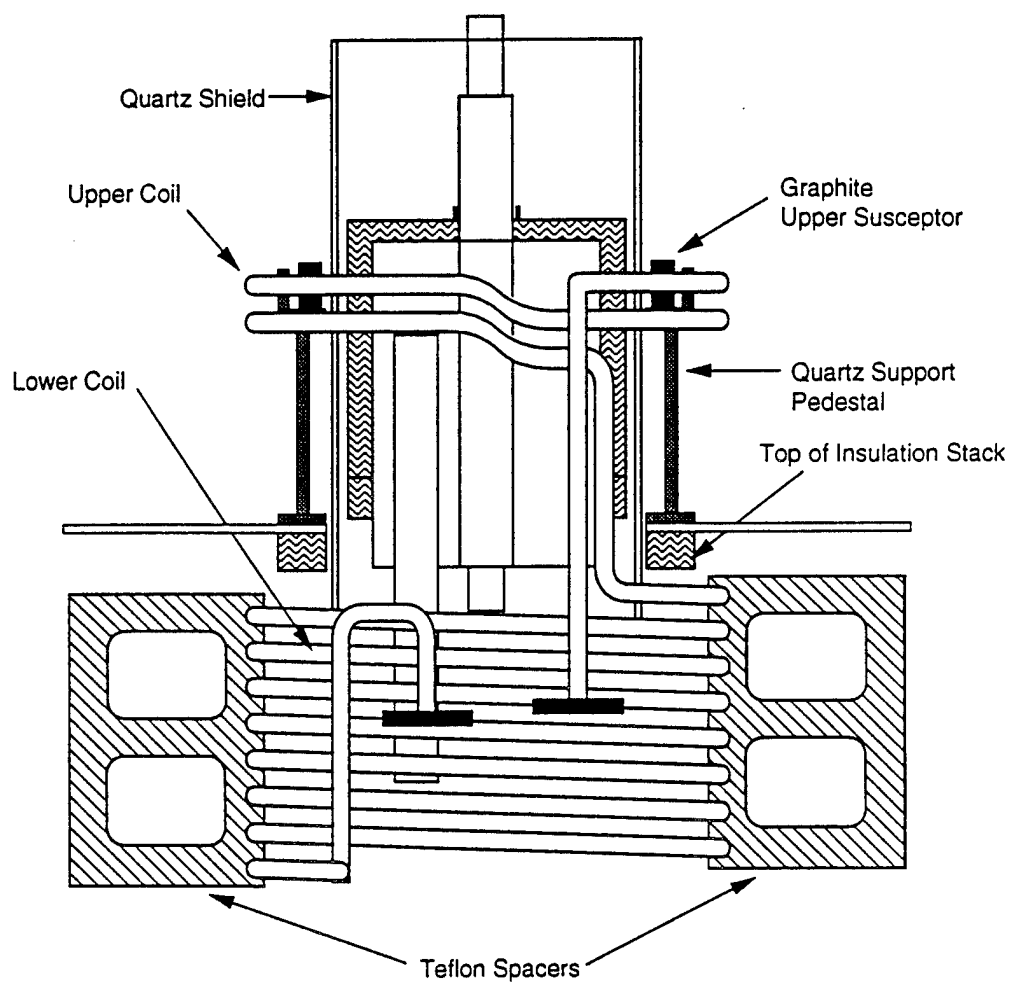
FIGURE IV-5

FIGURE IV-6

Injector temperature as a function of time.

76

Run 4041. Injector temperature, slope and crucible temperature vs. run time.
Vertical lines delineate SP/KVA level.

FIGURE IV-7

77

Quartz Shield

Upper Coil

Graphite
Upper Susceptor

Lower Coil

Quartz Support
Pedestal

Top of Insulation Stack

Teflon Spacers

Dual coil with Teflon centering spacers in relation to the injector.

FIGURE IV-8

INTRODUCTION

During the reporting period from October 1, 1992 through June 30, 1993 several experiments were made to improve the performance of the MLEK process for InP growth. Key parts of the crystal growth system were upgraded to improve system performance. Experiments were made to synthesize $ZnGeP_2$ by the P-injection process, and to grow $ZnGeP_2$ crystals by the CVT (Chemical Vapor Transport) process. Since CVT growth occured at 875° C, which is below the $ZnGeP_2$ disorder/order temperature of 951° C, this process has the potential for growth of ordered $ZnGeP_2$. A manuscript and oral presentation entitled "Synthesis and Growth Processes for Bulk Zinc Germanium Diphosphide" were delivered at the Ninth American Conference on Crystal Growth in August 1993. The authors were Mr. David F. Bliss, Mr. Meckie Harris and Ms. Jane Horrigan of RL/ERX, and Mr. William M. Higgins, Dr. Alton F. Armington and Mr. Joseph A. Adamski of Parke Mathematical Laboratories, Inc. Mr. Higgins gave the oral presentation.

EXPERIMENTAL

A series of fourteen (14) high pressure MLEK experiments were performed in these three quarters. One phosphorus injection experiment successfully produced an InP melt, but mechanical interference between the quartz heat shield and the seed holder prevented a crystal from being grown during the injection run. One InP run was aborted because the RF coil arced and the RF generator had to be turned off. Three InP remelt runs resulted in the growth of two InP crystals. RF coil arcing has occurred before in this system. Evaluation of the broken coil showed that two turns of the coil had probably touched at one spot. To prevent this from reoccurring, we have placed ceramic spacers between the coil turns at several vulnerable spots. This has resulted in a stiffer assembly which is much less likely to shift around and arc. An inspection mirror is used before each run to look at the spacing of the coil turns. One phosphorous injection experiment successfully produced an InP melt, but we were unable to successfully seed on after three attempts. The inconel sheathed thermocouple had "burned out" during the injection process. One InP run was aborted after a short length of crystal was pulled because the water cooling hose slipped off of the magnet and flooded the lab. The first run with a molybdenum sheathed type K thermocouple was a remelt run and the thermocouple appeared to "burn out" after the crucible temperature went to over 1355°C. The run was aborted after several attempts to seed and for the flat crown only resulted in twinned crystals. The next remelt run with a molybdenum sheathed thermocouple had a misaligned quartz convection shield. This resulted in erratic rotation of the shield. The resultant thermal asymmetries resulted in melted seeds and dendritic growth.

Thermocouple "burn out" and meltdown of the inconel sheath have been significant growth process control problems. The use of molybdenum sheaths will eliminate the melted sheath problem. Growth temperatures must stay below 1360°C to prevent the loss of the K thermocouple element. This becomes a difficult problem when

thermal runaway occurs during the phosphorous injection process. The rate of change feature on the Omega datalogger will help us monitor and minimize the thermal runaway.

The use of pointed seeds eliminated the formation of the bubble that migrates to the meniscus between the seed and the melt. This bubble can cause a crystal to become polycrystalline growth. An attempt at high purity growth of InP used a 4" diameter PBN crucible. Incorrect system pressure resulted in loss of phosphorous to the walls and windows of the system. A polycrystalline ingot was grown. A remelt run was aborted due to bottom thermocouple failure.

Two $ZnGeP_2$ compounding runs were made. We attempted to nucleate one of the charges with a cold alumina rod. A polycrystalline matrix was formed that appeared to have $ZnGeP_2$ in it. Two $ZnGeP_2$ CVT growth runs were made. The first run was a double transport of the $ZnGeP_2$. The second run was a single transport with more isothermal source and growth environments. All the material transported from the source to the growth zone.

InP growth Run 10:14:92 was a successful remelt and growth of the InP charge formed in the Injection Run 9:30:92. The resultant crystal was oriented (100), and the diameter varied from 2.5" to 2.8" over the 2" length. This was the first growth run where crucible rotation was used for the entire run.

InP Growth Run 12:16:92 was a remelt of Injection Run 10:21:92. This was the third remelt for this charge. Extra Fe was added to improve the semi-insulating properties of the InP. A (100) seed was used. The crystal repeatedly became polycrystalline during the seeding process. The twins appeared to propagate back to the seed when we melted back. We decided to pull the crystal in order to get future seed material.

$ZnGeP_2$ Injection Run 12:2:92 appeared to be too short. Only about 1/3 of the phosphorus had been injected into the melt after 25 minutes. The injector held the remaining 2/3 of the phosphorus. For a complete reaction of the Zn and Ge, the injection phase must last longer and thermocouples should be used to monitor the crucible and the top injector temperatures. X-ray tests indicated that the solid charge was rich in Zn and Ge and contained smaller amounts of phosphorus. The vapor pressure of the hot Zn was high and some of it was lost to the chamber before the B_2O_3 encapsulant melted. Excess Zn needs to be added in future runs to compensate for this.

$ZnGeP_2$ Injection Run 12:8:92 was successful. An excess 5% Zn was added to compensate for evaporative losses. Most of the phosphorus was injected into the melt and reacted. The injection lasted about 1 hour, and the injector was removed after the top temperature reached 630°C. An alumina ceramic rod attached to the cool seed

shaft was used as a nucleation source for the melt. The melt temperature was ramped at about 1°C/minute over a 2 hour period to about 1054°C. The temperature was then ramped down at about 4.6°C/minute over a 2 hour period to about 494°C. The system was then rapidly cooled down over 45 minutes. The resultant polycrystalline charge was 350 grams and is shown in the attached photo. X-ray analysis indicates that the crystal plane spacings match literature values for $ZnGeP_2$, but the X-ray intensities vary. This may be due to orientation or a slight difference in stoichiometry. A trace of unreacted Ge was observed. Optical microscopy shows the presence of both metallic material and a clear reddish material. This material is the $ZnGeP_2$.

InP Growth Run #4001 was an undoped injection run. Pumpdown of the molten indium charge at 544°C resulted in a very shiny and clean indium charge. The inconel sheathed thermocouple "burned out" during the phosphorus injection part of the run. This makes accurate control of the growth process very difficult. We cannot judge the melt temperature very accurately without it. The seed quickly melted three times during the seeding operation. The run was aborted after the seed was used up. During the injection process the InP melt was pulled part way up into the quartz injector tube when the injector temperature dropped slightly and created a partial vacuum in the injector. Some of this InP solidified in the injector tube and created an almost complete plug. A completely solid InP plug could result in an exploded or imploded injector. The use of the rate of change mode for the injector thermocouple will allow us to monitor this temperature very closely in the future. The ingot was 47.6% phosphorus. We ended the injector run at 646°C. We need to inject longer to increase the phosphorus content.

InP Growth Run #4002 was an undoped injection run. A (111) seed was used. Pumpdown of the indium charge at 617°C was not completely successful. The boron oxide encapsulant had melted and sealed over the molten indium and any volatile impurities that we wanted to pump off. This was a long, slow injector run. The final injector temperature was 700°C. This was done to maximize the amount of phosphorus injected into the melt. The inconel sheathed thermocouple died during the injection part of the run when the temperature reached 1385°C. The lack of a rugged crucible thermocouple makes it very difficult to determine the proper seeding temperature. After several tries, the best that could be obtained was a twinned crown. We pulled about 15mm in 1 hour. The run was abruptly aborted when we accidentally lost one of the cooling water hoses for the magnet.

InP Growth Run #4003 was a remelt of the prereacted charge from Run #4001. Iron was the dopant and a (100) seed was used. This was the first run with a molybdenum sheathed type K thermocouple. The melt temperature went to 1355°C when the magnet was turned on. The sheath survived but the thermocouple element appears to have been "burned out" at the end of the run. Several attempts at seeding

were unsuccessful. A meniscus did not want to form when the seed was inserted in the melt. Only twinned crystals could be grown. The run was shut down.

InP Growth Run #4004 was a remelt of two previously pulled crystals. This was a very clean melt. Tin was the dopant and a (100) seed was used. Some of the bottom crucible insulation was removed to allow faster thermal response and to reduce the temperature gradient between the top and bottom of the melt. The crucible temperature stayed below 1230°C for the entire run, and the molybdenum sheathed thermocouple has survived. The misaligned quartz convection shield resulted in erratic rotation of the shield. The resultant thermal asymmetries resulted in melted seeds, twinned seeds and dendritic growth. After repeated attempts at growth, the run was shut down.

InP Injection Run #4005 was successful. A (111) seed was used. The seed repeatedly melted off. A weak meniscus finally formed, and we grew a 2.5" diameter and 2" long polycrystalline ingot. This run showed that crucible height has a significant impact on injection rate. This was a fast injection (26 minutes total), and a clean melt was the result. Raising the crucible further should slow down the injection rate and make it more controllable. The pointed seed eliminated the bubble that forms and migrates to the seed/meniscus interface. This bubble can be a source for stress and nucleation.

InP Injection Run #4006 was not completely successful. This was planned as a high purity InP growth run. An undoped charge with a PBN crucible was used. The injector was lowered into the melt before the system pressure had been increased to 600 psi. This resulted in the injector heating too rapidly. This was about a 20-minute injection, and a lot of phosphorus (57 grams) was lost to the system. The crucible was at about the same position as in Run #4005. The crucible needs to be positioned higher to slow down the injection rate. A (111) seed was used. A 2.5" diameter and 1.25" long polycrystalline ingot was grown.

InP Growth Run #4007 was a remelt of the InP charge formed in the Injection Run #4006 and an unspecified Fe doped ingot. This was the first use of a concentric pair of quartz shields to minimize convection currents and to minimize deposition of phosphorus on the shields. A longer quartz front window was used to minimize phosphorus deposits on it. A (100) seed was used. The seed repeatedly melted off. The seeding temperature was about 100°C cooler than expected. The bottom thermocouple had failed and caused the system to be much hotter than desired. The shields clouded up when nitrogen pressure was released. About 29 grams of phosphorus were lost to the system. The run was aborted because of poor visibility, a bad thermocouple and the inability to get good seeding and single crystal growth.

The first $ZnGeP_2$ CVT growth run had a source zone temperature of 975°C and a growth zone temperature of 875°C. Due to the dimensions of the ampoule and the

furnace, the source and growth zones had significant temperature gradients within them. This was reflected in the difficulty to get complete transport of the source material. X-ray analysis confirmed that this was primarily tetragonal $ZnGeP_2$ with a trace of what is believed to be a cubic phase.

The second $ZnGeP_2$ CVT growth had a source zone temperature of $1000^{\circ}C$ and a growth zone temperature of $875^{\circ}C$. A new furnace was carefully constructed to make the temperatures within the zones more uniform. The source material completely transported to the growth zone over the two week growth run. The ampoule accidentally ruptured during the cooldown cycle. The iodine leaked out and the $ZnGeP_2$ partially decomposed. This process looks very promising. We should redesign the ampoules and use single crystal seeds in future runs.
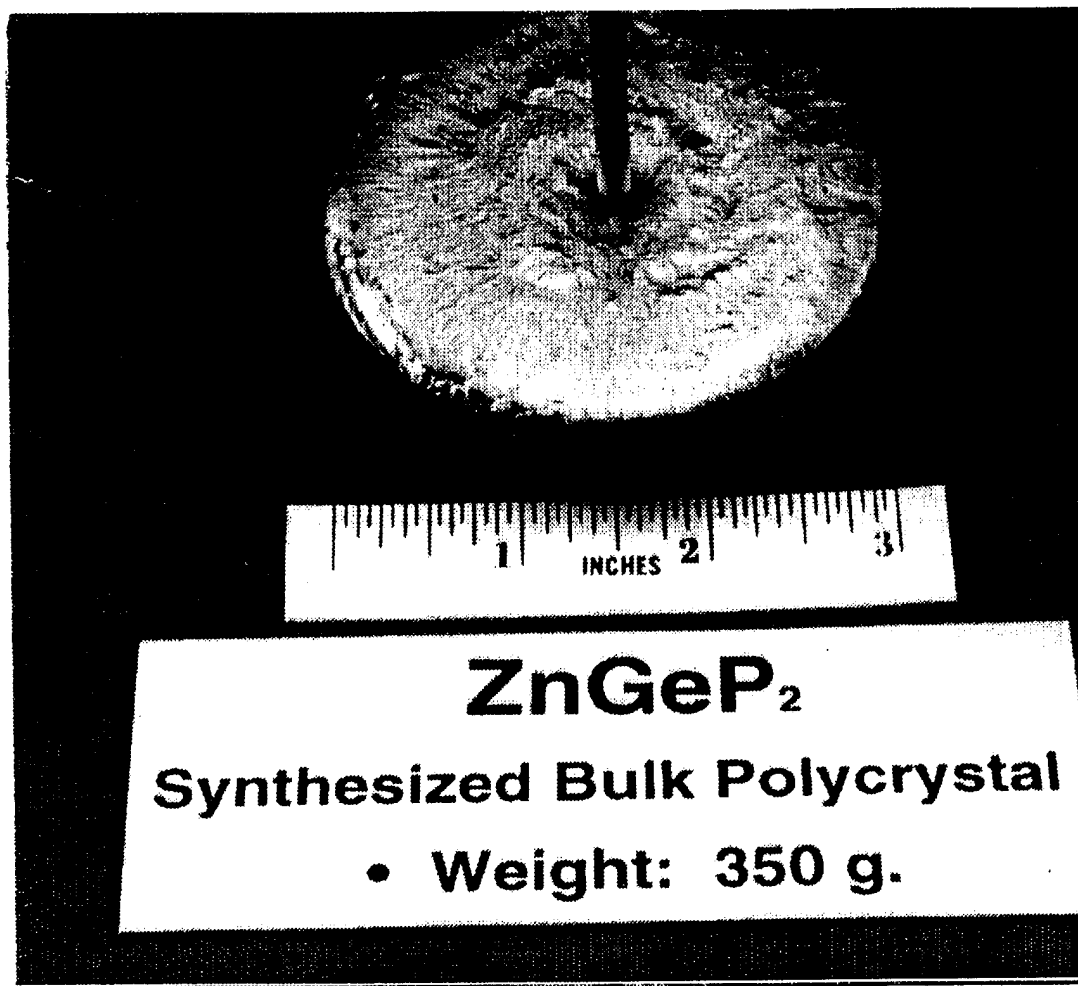
ZnGeP₂
Synthesized Bulk Polycrystal
• Weight: 350 g.

FIGURE V-1

ROBUST FIBER OPTIC NETWORKS

1. INTRODUCTION

1.1. GOALS

The goal of the R&D effort described below is to create fiber optic networks, on the scale of LANs, that provide a degree of robustness and survivability not previously possible. The potential for such robustness is created by using:

1) broadcast network topologies that possess a multiplicity of simultaneously active propagation paths between each pair of network users and

2) very wide band signal sets that allow the signals arriving at a user's receiver via the different paths to be resolved from each other and to be combined so as to eliminate multipath and intersymbol interference.

The advantage of using a network containing a multiplicity of paths is that the loss of some paths need not interfere with the network's operation-that is, it is robust. The signal sets do have bandwidths that far exceed those required in the absence of multiple paths but such signals are feasible in networks which utilize the fiber's full optical bandwidth. This work is intended to determine how that can best be done, in both a theoretical and a practical sense.

To achieve that end the substantial body of theory concerning the design and performance of systems intended to operate in the face of multipath and intersymbol interference[1-3] has been brought to bear upon robust fiber optic networks. Additionally, classes of network topologies whose performance can be analyzed have been identified and the analysis has been completed. Briefly stated, the conclusions reached thus far are as follows:

1. The basic concept for robust networks appears to be sound.

2. It will be necessary to use relatively wide band optical sources so as to avoid deleterious carrier phase interference on paths that have the same nominal group delay. This bandwidth precludes the use of heterodyne detection.

3. The use of optical amplifiers within the network often will be dictated by the large propagation losses of robust networks.

4. The noise of optical amplifiers will severely constraint the performance of the network unless predetection optical filtering is used to eliminate out of band noise.

These conclusions will be discussed in more detail after the structure and properties of the networks are reviewed.

1.2. NETWORK DESCRIPTION

The network shown in Fig. VI-1 possesses a substantial degree of robustness and illustrates the characteristics of robust networks. In the figure each link represents a unidirectional fiber. Each passive coupler dissipates some of the power incident upon it and distributes the rest to the outgoing fiber links and to any user receiver that may be attached to it.

The receivers, and their associated transmitters, i.e. the transceivers, are indicated by a short diagonal line emanating from a coupler. Four transceivers are shown in the figure but the number could be much larger. The connection of transceivers to the network can be implemented in several different ways that will be discussed in Section 4.2.

Optical amplifiers also may be present within the network. They are depicted in Figure VI-1 by: —▶— The use of such amplifiers can significantly ameliorate the consequences of the rather large propagation losses associated with robust networks. However, the accumulation of optical noise from them limits the number of amplifiers that can be used-particularly when predetection optical filtering is not employed.

The network operates in a broadcast mode so an access method is required to create simultaneous virtual circuits between different transceivers. Because of the multiple propagation paths that exist within the network FDMA or CDMA are preferable to TDMA. The choice between FDMA and CDMA ultimately will be dictated by the relative merits of the available technology but for the initial phases of this investigation FDMA has been assumed.

With either FDMA or CDMA communication is established by setting up a virtual circuit, between the transceivers in question, that functions essentially independently of all other such circuits. Therefore, the analysis and design of the network reduces to the analysis and design of the virtual circuits, on the one hand, and the network control mechanism used to establish the virtual circuits on the other. The control problem is nearly identical to that encountered in all other broadcast networks employing virtual circuits- the new challenge is in the design of the virtual circuits themselves.

The unique characteristic of the virtual circuits is that power arrives at any given transceiver, say the jth, by many different paths. For example, from transceiver i to transceiver j in Fig. VI-1 there are the three paths that pass through five intervening couplers plus many others passing through more couplers. Indeed, since the network contains loops, an infinite number of paths exists between every pair of transceivers.

The network robustness is accompanied by both multipath and intersymbol interference that can preclude satisfactory performance unless appropriate wide band signals are used. Loosely stated the requirements are that

1. the bandwidth of the signals exceed the reciprocal of the minimum differential delay between paths and

2. carrier phase interference be kept within acceptable limits.

When these conditions are satisfied the contributions of the different paths to the received signal resulting from one transmitted symbol can be resolved from each other and combined in a constructive manner and intersymbol interference can be eliminated effectively by an equalizer.

1.3. MULTIPATH AND INTERSYMBOL INTERFERENCE

To illustrate the nature of the multipath interference problem suppose that, in communicating one symbol of information to transceiver j, transceiver i transmits the signal p(t) -corresponding to the complex modal amplitude of a single mode fiber excited by a modulated narrow band laser. The complex modal amplitude at transceiver i then will be

EQ. 1

$$\sum_{k} \sqrt{\mu_k}\, p(t - T_k) \exp j\varphi_k$$

where the sum on k is over all the propagation paths connecting transceivers i and j, μ_k is the power attenuation on the kth path, T_k is the group propagation delay associated with that path and $\varnothing_k$ is the optical phase shift associated with it. The phase shift accounts for the very small differences in propagation delay that result from small variations in the length of fiber.

Terms in Eq. 1 with different values of T_k give rise to time dispersion and selective fading in the received signal and terms for which the T_k are identical may give rise to nonselective or flat fading. Referring to the network shown in Fig. VI-1 and assuming that all links in the network are of the same length, flat fading results from sets of paths that contain the same number of couplers and

87

time dispersion and selective fading results from sets of paths that contain different numbers of couplers.

1.3.1 Nonselective Fading

Nonselective fading attenuates the signal collected from the paths in question without changing its shape. Since the phases ϕ_k are unknown and random this attenuation can be substantial. Three ways of dealing with it have been considered in the investigation.

One way is to treat the occurrence of nonselective fading as another mechanism by which sets of paths are lost and to insure that the number of sets is large enough to provide acceptable performance on the virtual circuits even when such fades occur. Analysis has shown that this approach is not viable.

Another way is to use lasers, or LEDs, whose spectral linewidths are large enough to average out the phase interference between paths, i.e. to cause the signals to combine incoherently. This does preclude the use of heterodyne detection but it appears to be a promising approach for direct detection receivers. This is the approach we have chosen to take.

Some preliminary thought was given to the possibility of finding network topologies for which no two paths between transceivers have the same envelope delay, i.e. topologies for which the T_k in Eq. 1 are all different. However, it was concluded that few, if any, topologies of practical interest satisfy this condition.

1.3.2 Selective Fading

Time dispersion, which results in selective fading, also can seriously degrade the communication performance of the virtual circuits but this degradation is far less severe when the bandwidth of p(t) is large enough that the signals arriving on paths with different group delays can be "resolved". In the simplest case this will be possible when the signals arriving on the different paths do not overlap. For the network of Fig. VI-1 with all links of equal length they will not overlap if the width of p(t) is less than the link propagation delay.

More generally, when direct detection without predetection filtering is used it will be possible to resolve the signals if

EQ. 2

$$\int dt \, |p(t)p(t+T_m-T_n)|^2 = 0$$

88

for values of m and n such that $T_m - T_n$ is nonzero. Equation 2) always can be satisfied by a properly chosen p(t). The bandwidth of p(t) will be on the order of the reciprocal of the minimum nonzero value of $T_m - T_n$.

When the signals on different paths are resolvable the (optimum) receiver performs as though it had separate access to the signals arriving on each of the paths rather than only to their sum. Then the proper design and performance of the virtual circuits connecting transceivers can be determined in a relatively straightforward way by drawing upon well know results in communication theory - provided that intersymbol interference is not a concern [1]. That was the initial goal of the work.

1.3.3. Intersymbol Interference

Intersymbol interference is a manifestation of multipath interference that involves successive transmitted information symbols. To illustrate the issues involved, consider a sequence of binary information symbols s_1, s_2, s_3, s_4, s_5, ... that is to be sent from transceiver i to transceiver j at a rate of one symbol every T seconds by transmitting the complex envelope

EQ. 3
$$\sum_n A_{kn} p(t - nT)$$

where

EQ. 4a
$$A_{kn} = 0 \text{ if } s_n = 0$$

and

EQ. 4b
$$A_{kn} = 1 \text{ if } s_n = 1$$

As a result of multipath propagation within the network the complex envelope at the destination will be

EQ. 5
$$\sum_k \sum_n \sqrt{\mu_k} A_{kn} p(t - T_k - nT) \exp j\varphi_k$$

Intersymbol interference occurs when some of the signals corresponding to one transmitted information symbol overlap, or interfere with, those corresponding to another information symbol. It will not occur if T exceeds the

89

sum of the largest T_k and the width of p(t). In particular, it will not occur when the data rate 1/T is small enough.

For larger data rates intersymbol interference will occur and can preclude satisfactory performance of the virtual circuits unless it is dealt with properly. A large body of knowledge concerning techniques for dealing with it effectively exists and has been brought to bear upon the robust networks of interest here [1-3].

The performance limitations imposed by selective fading and intersymbol interference are the subjects of the following sections. In Section 2 the impulse response describing propagation on a virtual circuit is developed and the total amplifier noise arriving at a receiver is determined. In Section 3 the performance of a virtual circuit is expressed in terms of those impulse responses and the optical noise power when the bandwidths of the signals and noise are large enough that the network is linear in power- as it will tend to be if deleterious flat fading is to be avoided and optical prefiltering is not used. In Section 4 the frequency responses for some specific networks are determined, and in Section 5 some of the tasks that remain to be addressed are discussed.

2. **VIRTUAL CIRCUIT MODEL**

We focus upon the virtual circuit between two users and realistically assume cross talk from all other such circuits is negligible. The details of coupling the user's transceivers to the network are discussed in Section 4. Here we model the system's behavior from an input to one node to an output of another. That is, we find the node-to-node impulse response of the network.

The fact that the bandwidths of the optical transmitter and the amplifier noise are large compared to both the post detection bandwidth and the reciprocal of the differences in group delays for different paths implies that the circuits behave as though they were linear in power. In Section 2.1 the impulse response relating the transmitted and received signal powers is developed and in Section 2.2 the total amplifier noise arriving at a receiver is expressed in terms of those responses and the distribution of amplifiers. In Section 2.3 the results are combined into a system model for the virtual circuit.

2.1 VIRTUAL CIRCUIT IMPULSE RESPONSE

To obtain the power impulse resonse under the variety of conditions of interest, we first consider the optical fields within the network. Since the fibers are assumed to be single mode those fields are described by a complex modal amplitude. Those modal amplitudes will be of the form s(t)z(t) where s(t) is the

90

complex envelope of the information signal representing a sequence of messages and z(t) is the random complex field generated by the optical source.

In the extreme of a very narrow line width source, z(t) would be a constant and the modal amplitude at the receiver would be obtained by convolving s(t) with the impulse response describing the propagation. However as the linewidth increases to the point where the bandwidth of z(t) is much larger than that of s(t) some modification of the equation is necessary.

In particular, as the bandwidth of z(t) increases the small differences in propagation delay that will inevitably exist between different paths possessing the same group delay cannot be accounted for by a phase delay alone. Consequently, the impulse response relating the modal amplitudes at two points will be of the form

EQ. 6

$$h(t) = \sum_{i,k} s_{ik} \delta(t - T_i - \delta_{ik})$$

In this expression $\delta(.)$ is the unit impulse function, the T_i are the group delays of the different transmission paths forming the virtual circuit in question, s_{ik} is the strength of the kth path whose group delay is T_i and the δ_{ik} account for the very small variations in propagation delay that give rise to phase interference.

Without loss of generality, the T_i will be assumed to be distinct. That is, the s_{ik} and δ_{ik} account for the combined effect of all the physical paths that possess the group delay T_i. The δ_{ik} are so small that their effect upon s(t) can be neglected- but not necessarily their effect upon z(t) .

The received power is determined by convolving the above impulse response with s(t)z(t) and taking the magnitude square of the result. When account is taken of the fact that the δ_{ik} are too small to effect s(t) the following expression for the received power is obtained.

EQ. 7

$$P(t) = |\sum_{i,k} s_{ik} s(t - T_i) z(t - T_i - \delta_{ik})|^2$$

Equation 7 clearly is not a linear relationship between the transmitted and received signal powers. However, since the bandwidth of z(t) is much larger than the post detection bandwidth the detector will behave as though its input were the time average of P(t) over a time that is large relative to the reciprocal of z(t)'s bandwidth but small relative to the reciprocal of s(t)'s bandwidth. Since the

91

process is ergodic, that time average will equal the ensemble average given below.

EQ. 8

$$P(t) = \sum_i \mu_i |s(t-T_i)|^2$$

where

EQ. 9

$$\mu_i = \sum_{k,l} s_{ik} \dot{s}_{il} R_z(\delta_{ik} - \delta_{il})$$

and $R_z(.)$ is the correlation function of $z(t)$. These expressions have been simplified by using the fact that the bandwidth of $z(t)$ exceeds that of $s(t)$ which, in turn, exceeds the reciprocal of the smallest difference between group delays.

Equation (8) implies that the power impulse response is given by

EQ. 10

$$h(t) = \sum_i \mu_i \delta(t - T_i)$$

where μ_i is given by Eq. 9.

One familiar extreme of Eq. 9 occurs when the bandwidth of $z(t)$ is so large, i.e. the correlation function $R_z(.)$ is so narrow, that only the terms in Eq. (9) for which k equals l contribute to the sum. Then Eq. (9) reduces to

EQ. 11

$$\mu_i = \sum_k |s_{ik}|^2 R_z(0)$$

which describes the addition of powers in an "incoherent" system.

Another interesting extreme of Eq. 9 arises when the source linewidth is still large relative to the post detection bandwidth and the reciprocal of the minimum difference between the group delays but is small relative to the reciprocal of (δ_{ik} - δ_{il}) for all i, k and l. Then $R_x(\delta_{ik} - \delta_{il})$ will essentially equal $R_x(0)$ and Eq. 9 can be restated as

EQ. 12

$$\mu_i = \left| \sum_k s_{ik} \right|^2 R_i(0)$$

With the power impulse response before us we next determine the amount of amplifier noise power present at a receiver's input.

2.2 OPTICAL AMPLIFIER NOISE

Optical amplifiers within the network reduce the propagation loss at the cost of added spontaneous emission noise. That noise is characterized below for direct detection receivers that do not use predetection optical filtering.

The optical noise modal amplitudes of the amplifiers can be modeled as zero mean Gaussian random processes with the common power spectral density, $S_a(f)$, referred to the amplifier's input. The noises of different amplifiers will be statistically independent so the power spectral density of the noise at the receiving node will be a Gaussian random process whose power spectral density equals the sum of the spectral densities of the different processes. The spectral density will be very wide band because of the frequency multiplexing that is employed.

For direct detection receivers without optical prefiltering and wide band noise the receiver behaves as though the noise incident upon it were a constant equal to the average noise power. This is the so called "constant intensity" model. Moreover, because of the wide band signals employed, the response of the detector to the sum of signal plus noise is just the sum of the responses to them separately.

To determine the average noise received at node i we first consider the nth amplifier located at a position in the network from which the power impulse response to node i is $h_{ni}(t)$. The contribution of this amplifier to the average noise power at the receiver is $P_n H_{ni}(0)$ where P_n is the average value of the amplifier's optical noise power and $H_{ni}(0)$ is the DC value of the frequency response associated with $h_{ni}(t)$. Consequently, the total noise power at the receiver is

EQ. 13a

$$P_i = \sum_n H_{ni}(0)$$

where the sum is over all amplifiers in the network and

93

EQ. 13b

$$P_s = \int_{-\infty}^{\infty} S_s(f)df$$

2.3 SYSTEM MODEL

In this phase of the investigation it has been assumed that m-ary PAM or QAM is employed. Then s(t), the complex envelope of the transmitted signal, is of the form

EQ. 14

$$s(t) = \sum_n A_{k_n}p(t-nT)$$

where p(t) is the basic signaling pulse, T is the signaling interval, k_n is the nth in the sequence of m-ary information symbols to be transmitted (k_n = 1, 2, ..., m) and A_{k_n} is the amplitude used to transmit the information symbol k_n (A_{k_n} = A_1, A_2,..., A_m). We will assume, realistically, that p(t-iT) and p(t-jT) are disjoint in time for i not equal to j.

For direct detection with a source whose linewidth is wide relative to the post detection bandwidth and the reciprocal of the smallest difference between group delays the post detection waveform, y(t), can be modeled as described in Fig. VI-2. In that figure h(t) is the impulse response given by Eqs. 10 with μ_i given by Eq. 9 and n(t) is a (real) zero mean noise that accounts for the optical amplifier noise, signal shot noise and thermal noise. Which of the three noises is dominant depends upon a number of factors but thermal noise usually can be neglected for the reasons discussed below.

In the absence of predetection optical filtering, all system users contribute to the signal shot noise. Thus it will be the dominate noise if there are many such users or if the propagation loss to the intended receiver from the transmitter of interest is much greater than the loss from some other user. This is an example of the so-called near-far problem that arises in many networks. It is important in the robust networks we consider because the difference in propagation loss between the "far" transmitter of interest and a "near" noise contributor can be many tens of dB unless optical amplifiers are used in the network.

The noise, n(t), in Fig. VI-2 will be a complicated nonstationary process when it is dominated by signal shot noise. However, if the noise is contributed by many users there will be enough averaging that it will not be grossly in error to model the noise as a stationary process with a power spectral density of No/2.

94

In the interests of expediency we will assume that is the case when signal shot noise is dominant. The spectral density is given by

EQ. 15

$$\frac{No}{2} = \frac{h\nu}{nP_b}$$

where Pb is the average total received signal power, η is the detector's quantum efficiency and hν is the energy of a photon at the operating wavelength.

Amplifier noise, rather than signal shot noise, will be dominant if many optical amplifiers are used to reduce the propagation loss of the virtual circuits. As discussed earlier that noise will be stationary with a power spectral density that can be approximated by No/2. The value of No/2 is given by Eq. 15 with Pb replaced by Pa as given by Eq. 13.

An equalizer is needed to reduce the effects of the intersymbol interference (ISI) present in y(t). For a broad class of equalizers y(t) is first passed through a filter matched to the pulse that y(t) would contain if a single information symbol were transmitted and the output of that filter is then sampled periodically to obtain a set of samples that are passed through a transversal filter to obtain a set of equalized samples that are used, perhaps in combination with decision feedback, to make symbol-by-symbol decisions as to the transmitted symbols.

Since it is well documented in the literature [1], the detailed description of that equalizer will not be presented here. Instead we turn to its performance for the situations of interest.

3. __PERFORMANCE EXPRESSIONS__

For this report it will be assumed that the number of taps employed in the equalizer is not constrained. Then, for a variety of equalizers, the output signal to noise ratio, or equivalently the output mean squared error can be expressed as relatively simple functions of the system parameters appearing in Fig. VI-2.

In presenting those functions it is useful to define

EQ. 16

$$g_{(t)} = \left| p_{(t)} \right|^2$$

95

For a zero forcing equalizer with decision feedback (ZF DFB) the mean squared error in the equalizer's output is given by

EQ. 17

$$mse = N_o \exp\left\{-\frac{1}{2\pi}\int_{-\pi}^{\pi} d\phi \ln S(\exp j\phi)\right\}$$

where

EQ. 18a

$$s(\exp j\phi) = \frac{1}{T}\sum_{k=-\infty}^{\infty}\left|Q(\phi + \frac{2\pi k}{T})\right|^2$$

which is called the folded spectrum and

EQ. 18b

$$Q(\omega) = G(\omega)H(\omega)$$

where $G(\omega)$ and $H(\omega)$ are the Fourier transforms of g(t) and h(t).

An equivalent expression for S(exp jø) is

EQ. 19a

$$S(\exp j\phi) = \sum_{k=-\infty}^{\infty}\rho(k)\exp jk\phi$$

where

EQ. 19b

$$\rho(k) = \int dt q(t) q^*(t - kT)$$

and q(t) is the inverse Fourier transform of Q(ω).

For the same equalizer used without decision feedback the mean squared error is

EQ. 20

$$mse = \frac{N_o}{2\pi}\int_{-\pi}^{\pi}\frac{d\phi}{S(\exp j\phi)}$$

where S(exp jø) is again the folded spectrum given by Eq.18a.

96

The mean squared error for a minimum mean squared error equalizer differs slightly from that for a zero forcing equalizer but the difference is negligible in the situations of interest here. Therefore Eqs.17 through 20 will be used to describe both classes of equalizers.

We now introduce two assumptions-one that is central to the investigation and another simplifying assumption that can be removed. The fundamental assumption is that p(t) is chosen so that, in response to the transmission of a single pulse, the signals arriving at the receiver from paths with different group delays can be resolved.

The assumption always can be satisfied by using a suitably chosen p(t) that has a large enough bandwidth. Stated mathematically, the assumption is that

EQ. 21

$$\int dt g(t - T_i) g^*(t - T_k) = 0$$

when T_i differs from T_k which occurs when i differs from k.

The simplifying assumption is that any intersymbol interference involves a complete, as opposed to a partial, overlap between the interfering pulses. Mathematically, the assumption is that T_i / T is a rational number. That is, the T_i are of the form

$$T_i = (M_i / N_i)T$$

where M_i and N_i are integers that may be functions of i. Without loss of generality, the N_i will be set equal to a single integer N, which is the least common denominator of the N_i. Also M_i may be taken to be 1 by introducing additional paths whose strengths are zero and relabeling the μ_i. Thus

EQ. 22

$$T_i = \frac{iT}{N}$$

When Eq.22 is introduced into the condition of Eq.21 that condition becomes

EQ. 23

$$\int dt g\left(t - \frac{iT}{N}\right) g^*\left(t - \frac{kT}{N}\right) = 0$$

for i different than k.

In combination with the expressions for h(t), Eq.18b implies that

EQ. 24

$$q_{(t)} = \sum_i \mu_i g\left(t - \frac{iT}{N}\right)$$

and that

EQ. 25a

$$p_{(k)} = E \sum_i \mu_i \mu_{(i + kN)}$$

where

EQ. 25b

$$E = \int dt \left| g_{(t)} \right|^2$$

Consequently,

EQ. 26a

$$S(\exp j\phi) = E \sum_i \sum_k \mu_i \mu_{(i + kn)} \exp(jk\phi)$$

which also can be written in the form

EQ. 26b

$$S(\exp j\phi) = \frac{E}{N} \sum_{i=0}^{N-1} \left| U\left(\frac{\phi + 2\pi i}{N}\right) \right|^2$$

where

EQ. 26c

$$U(\phi) = \sum_i \mu_i \exp(1 - j\phi_i)$$

For any given network, and hence given μ_i, the performance of the virtual circuit is determined by Eq. 26 in combination with Eqs. 17 and 20.

4. SPECIFIC TOPOLOGIES

In this section the node-to-node frequency responses are determined for several network topologies that are regular in the sense illustrated in Figs. VI-1

and VI-3. In particular, the nodes can be arranged in a rectangular array of rows and columns with a set pattern of links connecting them.

4.1 NODE TO NODE FREQUENCY RESPONSES

It will be assumed throughout that all links have the same nominal length, L. As discussed previously, it also will be assumed that all links are unidirectional and that the inevitable small variations in the propagation times for the links are large compared to the reciprocal of the source bandwidth so that the short term time averaged power arriving at a node is the sum of the powers arriving on each inbound link, i.e. the network is linear in power.

It further will be assumed that the power on an input link to a node produces an output power signal of μ times the input signal on each output link of the node. The value of μ will be assumed to be the same for all nodes. If the couplers were lossless the reciprocal of μ would be the number of output links per node, including those going to transceivers.

With these assumptions a network is completely characterized by μ, L and a description of the connections between the nodes. That description can be conveniently provided by a connection matrix, **C**, of elements c_{ij}, where c_{ij} is one if a link goes from node i to node j and is zero otherwise. The connection matrices for the networks of the form shown in Fig VI-3a and b but with three rows and four columns are as follows

EQ. 27a   Refer to Figure VI-3c

for the network of Fig VI-3a and

EQ. 27b   Refer to Figure VI-3c

for the network of Fig VI-3b

The frequency response from an input link of node m to an output link of node n can be written as

EQ. 28

$$H_{mn}(f) = \sum_{k=1}^{\infty} N_{mn}(k)\mu^k \exp\left[-j2\pi(\kappa - 1)fL\right]$$

where $N_{mn}(k)$ is the number of distinct paths by which a signal can travel from the input link to the output link by traversing k nodes.

Alternatively, $H_{mn}(f)$ is given by the mn element of the following matrix **H(f)**

99

EQ. 29

$$\underline{H}(f) = \mu \sum_{R=0}^{\infty} \mu^k \underline{C}^k \exp(-j2\pi kfl)$$

which also can be written as

EQ. 30

$$\underline{H}(f) = \mu \left\{ I - \mu \underline{C} \exp(1 - j2\pi fL) \right\}^{-1}$$

4.2. USER CONNECTIONS

It remains to discuss the mechanisms by which users are connected to the network. Two possibilities will be considered. One is that the coupler at each node contains an unused input and output link to which users can connect their equipment and the other is that users insert their equipment into a link either by severing it or by inserting a coupler into it.

For the first method it will be assumed, for convenience, that the unused links are characterized by the same value of μ as are the other links. The disadvantage of this method is that it increases the insertion loss of all the couplers thereby increasing the propagation loss for the users. When it is employed the user's frequency responses are the network node-to-node frequency responses obtained from Eq. 28 or 30 .

For the second method of connection, if the user connection is realized by severing a link the network's topology and connection matrix are changed. The user's frequency responses again are given by the node-to-node frequency responses of the (modified) network since the transmitter and receiver are located on node input and output links. However, in contrast with the first method, for which the transmitter and receiver are connected to an input and an output of one node, the user's transmitter and receiver now will be on links connected to different nodes.

A variation of the second method is to insert an additional coupler, with gain, into a link instead of severing it. If the gain is properly chosen neither the topology nor the node-to-node frequency responses will be changed, although some additional amplifier noise will be introduced into the network.

The performance differences between the different user connection methods will be small when the network is robust, as we wish it to be, and will be given by the node-to-node responses of Eqs. 28 and 30. In the interests of simplicity we will assume that is the case and use the node-to-node responses as the responses describing the propagation between users.

4.3. A SIMPLE RECTANGULAR MESH NETWORK

Networks of the form shown in Fig. VI-3a and described by the connection matrix of Eq. 27a have some robustness, are easy to analyze and can be used to illustrate several important points. They have the virtue of being free of ISI but the disadvantage of not being fully connected. In principle, the disadvantage can be overcome by overlaying four such networks each rotated a multiple of 90° from the others.

The node-to-node response, $H_{mn}(f)$, of this network is most easily determined by determining the $N_{mn}(k)$ in Eq. 28 rather than by performing the matrix inversion in Eq. 30. To that end we write m and n in the form $c + (r-1)N_c$ where N_c is the number of columns in the network and c and r are the column and row in which the node in question is located. Note that $1 \leq c \leq N_c$ and $1 \leq r \leq N_r$, where N_r is the number of rows in the network . For the top rightmost node in Fig VI-3a, and VI-3b c equals 8 and r equals 1. For the bottom leftmost node c equals 1 and r equals 6.

Referring to Fig. VI-3a, since signals flow only to the right and down, $H_{mn}(f)$ will equal zero unless the row and column indices, c_n and r_n, of node n equal or exceed the corresponding indices, c_m and r_m, of node m. When the row and column indices of node n do equal or exceed the corresponding indices of node m each path connecting the nodes will consist of $c_n - c_m$ horizontal links and $r_n - r_m$ vertical links. Since the total number of links in each such path is $c_n - c_m + r_n - r_m$ the number of paths, $N_{mn}(k)$, is given by a binomial coefficient. Specifically

EQ. 31a

$$N_{mn}(k) = \binom{k}{c_n - c_m}$$

when

EQ. 31b

$$c_n \geq c_m$$

and

EQ. 31c

$$r_n \geq r_m$$

where

EQ. 31d

$$k = c_n - c_m + r_n - r_m$$

When Eqs. 31b and c are not satisfied $N_{mn}(k)$ is zero.

Equations 28 and 31, combined with the fact that all paths connecting nodes m and n contain $c_n - c_m + r_n - r_m$ links, imply that

EQ. 32

$$H_{mn}(f) = \mu \binom{k}{c_n - c_m} \mu^\kappa \exp(-j2\pi fL)$$

when $c_n - c_m$ and $r_n - r_m$ are non negative. The absence of ISI in this network is evident from Eq. 32 which depends upon frequency only through a linear phase factor.

It is instructive to note the variation of $|H_{mn}(f)|$ with the relative position of the two user nodes. For simplicity, the discussion will be limited to square meshes for which N_c and N_r are equal. Without loss of generality, the transmitter will be assumed to be connected to the upper leftmost node of the network. For receiving nodes reached by paths containing K links the minimum value of $|H_{mn}(f)|$ occurs at receivers located in the same row or column as the transmitter. The maximum value occurs on, or adjacent to, the diagonal emanating from the upper leftmost node. The minimum is

EQ. 33

$$\min|H_{mn}(f)| = \mu^{k+1}$$

where k is given by Eq. 31d. The maximum value is

EQ. 34a

$$\max|H_{mn}(f)| = \mu^{\kappa+1} \frac{k!}{\left[(k/2)!\right]^2}$$

if k is even and by

102

EQ. 34b

$$\max|H_{mn}(f)| = \mu^{k+1} \frac{k!}{\left\{\left[\left(k+1\right)/2\right]!\right\}^2}$$

if k is odd. By Sterling's approximation, when k is large these maxima can be approximated by

EQ. 34c

$$\max|H_{mn}(f)| = (2\mu)^k \sqrt{\frac{2}{\pi k}}$$

when k is even and by

EQ. 34d

$$\max|H_{mn}(f)| = \left(\frac{2}{k}\right)(2\mu)^k \sqrt{\frac{2}{\pi k}}$$

when k is odd.

For values of μ less than one half the minimum and maximum values decrease as k, the number of links in the path, increases but the minimum decreases much more rapidly than the maximum. This is because a receiver connected to a node on the edge of the network can be reached by only one path whereas one connected to a node on the diagonal can be reached by many paths. Clearly, more paths to users on the edge of the network must be introduced if the network is to be made robust. That is, the connectivity must be increased.

4.4 CIRCULANT CONNECTION MATRICES

Valuable insight into the consequences of adding more connectivity to the network can be obtained by considering connection matrices that are circulants. Such matrices have the property that every row of the matrix is a cyclical shift of the preceding row. The connection matrix of Eq. 27b is a circulant.

4.4.1 Node-to-Node Frequency Response

A circulant matrix is completely specified by the elements of its first row which will be denoted by c_i, i equal 1, ...N for an N by N connection matrix $\underline{C}$. For the circulant connection matrix of Eq. 27b the elements are

EQ. 35

$$c_k = \begin{cases} 1 & k=2,5 \\ 0 & \textit{otherwise} \end{cases}$$

Circulant connection matrices have two properties that are very helpful in our analysis of robust networks. First, their eigenvalues, λ_k, and elements, c_i, are related by the expressions

EQ. 36a

$$\lambda_k = \sum_{i=1}^{N} c_i \exp\left[\frac{j2\pi(i-1)(k-1)}{N}\right]$$

and

EQ. 36b

$$c_k = \frac{1}{N}\sum_{i=1}^{N} \lambda_i \exp\left[\frac{-j2\pi(i-1)(k-1)}{N}\right]$$

Second, the mode-to-mode frequency response matrix, $H(f)$, is a circulant.

The fact that $H(f)$ is circulant matrix, combined with Eq. 36, implies that the elements, $H_{1k}(f)$, of the first row of $H(f)$ are related to the eigenvalues, v_i, of $H(f)$ by

EQ. 37

$$H_{1k}(f) = \frac{1}{N}\sum_{i=1}^{N} v_i \exp\left[\frac{1 j2\pi(i-1)(k-1)}{N}\right]$$

The eigenvalues, v_i, are, in turn, related to the λ_k by the expression

EQ. 38

$$v_i = \frac{\mu}{1-\mu\lambda_i \exp(-j2\pi fL)}$$

Therefore,

EQ. 39

$$H_{1k}(f) = \frac{\mu}{N}\sum_{i=1}^{N} \frac{\exp\left[-j2\pi(i-1)(k-1)\right]}{1-\mu\lambda_i \exp(-j2\pi fL)}$$

where the λ_k are related to the elements of the connection matrix by Eq. 36a.

104

As written, Eq. 39 gives the node-to-node frequency responses from a transmitter located at node 1 to a receiver located at node k. For other locations k is the receiver node number minus the transmitter node number, modulo N, plus one. For example, k equals 6 from node 3 to node 8, mod N, plus 1, and equals -4 from node 8 to node 3, mod N, plus 1.

4.4.2 Application to a Circulant Network

Equation 39 now will be used to determine an expression for the node-to-node frequency responses of the network whose circulant connection matrix has the first row.

EQ. 40

$$c_k = \begin{cases} 1 & k=2, \sqrt{N}+1, N-\sqrt{N}+1, N \\ 0 & otherwise \end{cases}$$

The topology of the network is illustrated in Fig. VI-4a and b for N equal to 36. Figure VI-4a shows the detailed connections between a node, i.e. a coupler, and its four nearest neighbors. The figure can be simplified by visualizing each pair of unidirectional fiber links between the nodes as a single bi-directional link. This has been done in Fig. VI-4b which shows the topology of the entire network in a compact form. Note that the number of rows, and also the number of columns, in the network is $\sqrt{N}$. The numbering of the nodes indicated in Fig. VI-4b yields a connection matrix of the form given in Eq. 40

There are two primary differences of form between the circulant network of Fig. VI-4 and the simple rectangular mesh of Fig. VI-3a. First, each unidirectional link in Fig. VI-3a has been replaced by a bi-directional link in Fig. VI-4. This change significantly increases the connectivity within the network. Second, the edges of the mesh have been connected, or wrapped around, in a way that makes the connection matrix a circulant.

By virtue of Eq. 36a, the eigenvalues of the connection matrix defined by Eq. 40 are given by

EQ. 41

$$\lambda_i = 2\cos\frac{2\pi(i-1)}{N} + 2\cos\frac{2\pi(i-1)}{\sqrt{N}}$$

Before introducing this expression into Eq. 39 it is helpful to specify the position of the transmitter and receiver nodes by the rows and columns in which they are located. That is, we express the location of the receiver as $c_r + (r_r 1)\sqrt{N}$ and the location of the transmitter as $c_t + (r_t -1)\sqrt{N}$ where r and c denote the row and column in which the equipment is located and the

subscripts r and t denote whether it is a transmitter or receiver. With this notation k, as defined following Eq. 39, may be written as

EQ.42a

$$k = \Delta c + \Delta r \sqrt{N} + 1$$

where

EQ.42b

$$\Delta_r = r_r - r_t$$

and

EQ.42c

$$\Delta_c = c_r - c_t$$

The modulo N operation has been omitted from Eq. 42a since the value of Eq. 39 is not affected by it.

It also is helpful to express the summation index, i, in Eq. 39 in the form

EQ. 43

$$i = l + 1 + m\sqrt{N}$$

and replace the summation on i with summations on l and m from zero to $\sqrt{N}$ - 1. With these changes Eq. 39 can be written as

EQ. 44a

$$H_{1k}(f) = \frac{\mu}{N} \sum_{l,m=0}^{\sqrt{N}-1} \frac{\exp\left\{-j\frac{2\pi l}{N}\left(\Delta c + \Delta r\sqrt{N}\right) - j\frac{2\pi m\Delta c}{\sqrt{N}}\right\}}{1 - \beta\left\{\cos\frac{2\pi\left(l + m\sqrt{N}\right)}{N} + \cos\frac{2\pi l}{\sqrt{N}}\right\}}$$

where

EQ. 44b

$$B = 2\mu \exp(-j2\pi fl)$$

To gain insight into the behavior of large networks it is helpful to let N become large In Eq. 44a. Then the summation on m converges to an integral and, after a change of variable, $H_{1k}(f)$ can be expressed in the form

106

EQ. 45

$$H_{1k}(f) = \frac{\mu}{2\pi\sqrt{N}} \sum_{l=0}^{\sqrt{N}-1} \int_0^{2\pi} \frac{d\theta \exp\left\{-j\Delta c\theta - j\frac{2\pi l}{\sqrt{N}}\Delta r\right\}}{1 - \beta\left[\cos\theta + \cos\frac{2\pi l}{\sqrt{N}}\right]}$$

Examination of this equation indicates that the sum on l also converges to an integral as N increases. In particular,

EQ. 46

$$H_{1k}(f) = \mu \int_0^{2\pi}\!\!\int \frac{d\theta d\phi}{(2\pi)^2} \frac{\exp[-j(\phi\Delta r + \theta\Delta c)]}{1 - \beta(\cos\phi + \cos\theta)}$$

4.4.3 Evaluation of $H_{1k}(f)$ in Two Situations of Interest

Equation 46 cannot be expressed in closed form but it can be usefully approximated in several situations of interest. One situation arises when Δc, or Δr, equals one, i.e. when the receiver in question is in the same column, or row, as the transmitter. Then it is expeditious to perform the integral on ø in Eq. 46 which leads to the following expression for $H_{1k}(f)$

EQ. 47a

$$H_{1k}(f) = \frac{\mu}{\beta} \int_0^{2\pi} \frac{d\theta}{2\pi} \frac{\left[\sqrt{\upsilon^2 - 1} - \upsilon\right]^{\nabla r}}{\sqrt{\upsilon^2 - 1}} \exp(-j\Delta c\theta)$$

where

EQ. 47b

$$\upsilon = \beta^{-1} - \cos\theta$$

Equation 47a can be cast in a more useful form with the change of variable

EQ. 48

$$z = \exp(-j\theta)$$

which yields a contour integration around the unit circle of the z plane as is illustrated in Fig. VI-5. Specifically,

107

EQ. 49a

$$H_{1k}(f) = \frac{j\mu}{2\pi\beta}\left(\frac{1}{2}\right)^{\Delta r-1} \oint dz F_+(z)$$

where the integration is in a clockwise direction and

EQ. 49b

$$F_+(z) = \frac{\left\{\sqrt{\left(z^2 - 2\beta^{-1}z + 1\right)^2 - 4z} + \left(z^2 - 2\beta^{-1}z + 1\right)\right\}^{\Delta r} z^{\Delta_c - \Delta_r}}{\sqrt{\left(z^2 - 2\beta^{-1}z + 1\right)^2 - 4z^2}}$$

Examination of Eq. 49b shows that $F_+(z)$ is an analytic function of z with isolated singularities. The singularities within the unit circle are two branch points X_1 and X_2 given by

EQ. 50a

$$X_1 = \beta^{-1} + 1 - \sqrt{\left(\beta^{-1} + 1\right)^2 - 1}$$

and

EQ. 50b

$$X_2 = \beta^{-1} - 1 - \sqrt{\left(\beta^{-1} + 1\right)^2 - 1}$$

For Δc less than Δr, F(z) also has a pole of order c-r at the origin. However, this situation need not be considered since, by virtue of Eq. 46, $H_{1k}(f)$ is a symmetric function of Δc and Δr when N is large. Therefore, in Eq. 49 Δc always can be taken to the larger of Δc and Δr. Then F(z) will have no poles in the unit circle.

We next explore the benefit of the added connectivity in the network of Fig. VI-4, as contrasted with the simple mesh network of Fig. 3VI-a. To that end, we suppose the equalizer discussed in Section 2 is effective in eliminating intersymbol interference so that the error probability is dependent upon the received signal only through the total energy received, i.e. only through $H_{1k}(0)$. We ask how $H_{1k}(0)$ for receivers in the same column or row as the transmitter, but far from it, compare for the two networks of interest. The answer can be obtained from Eq. 49 with Δr set equal to zero. Accordingly, we take Δr to be zero and Δc to be large in that equation. Then ß is real and the branch points X_1 and X_2 are real and positive with X_1 less than X_2.

108

By the properties of analytic functions the clockwise contour integral around the unit circle shown in Fig. VI-5 equals the counter clockwise contour integral around the "cut" joining the two branch points. The latter integral can be expressed as

EQ. 51a

$$H_{1k}(0) = \frac{j\mu}{\pi\beta}\left\{\int_{x_1}^{x_2} dzF_-(z) + \int_{x_2}^{x_1} dzF_+(z)\right\}$$

where

EQ. 51b

$$F_-(z) = -F_+(z)$$

Upon combining the equations and integrals one obtains

EQ. 52a

$$H_{1k}(0) = \frac{j}{\pi}\int_{x_1}^{x_2}\frac{dxx^{\Delta c}}{\sqrt{(x-X_1)(x-X_1^{-1})(x-X_2)(x-X_2^{-1})}}$$

where X_1 and X_2 are given by Eq. 50. Note that, since f equals zero, ß is now given by

EQ. 52b

$$\beta = 2\mu$$

Since Δc is large, the integral in Eq. 52a is dominated by values of the integrand for which x is approximately X_2. Then the integral can be approximated by

EQ. 53a

$$H_{1k}(0) = K_1\int_{x_1}^{x_2}\frac{dxx^{\Delta c}}{\sqrt{X_2 - x}}$$

where

EQ. 53b

$$K_1 = \frac{1}{\pi\sqrt{(X_2 - X_1)(X_2^{-1} - X_2)(X_1^{-1} - X_2)}}$$

This integral can be evaluated to obtain

109

EQ. 54a

$$H_{1k}(f) = g_1 K_1 X_2^{\Delta c}$$

where

EQ. 54b

$$g_1 = 2\sqrt{X_2 - X_1} \sum_{i=0}^{\Delta c} \frac{\binom{\Delta c}{i}(-1^i)\left(1 - \frac{X_1}{X_2}\right)^i}{2i + 1}$$

When the couplers have very little excess loss and transceivers are not attached directly to them, i.e. when μ_c and β are nearly 0.25 and 0.5, respectively, g_1 is very weakly dependent upon Δc. Then $H_{1k}(0)$ is approximately proportional to

EQ. 55a

$$(2\mu_c)^{-1} - 1 - \sqrt{\left[(2\mu_c)^{-1} - 1\right]^2 - 1}$$

where the subscript c has been added to indicate that this expression applies to a large circulant network of the form shown in Fig. VI-4. This is in contrast to the simple mesh network of Fig. VI-3a for which $H_{1k}(0)$ equals

EQ. 55b

$$\mu_m^{\Delta c}$$

where the subscript m denotes that this expression is for the mesh network structure. For the mesh network $H_{1k}(0)$ always decreases exponentially with Δc but for the circulant network with μ equal to 0.25 there is no exponential decrease. Clearly, the additional connectivity of the circulant reduces the propagation loss for receivers in the same row or column as the transmitter.

As μ_c decreases from 0.25, either as a result of excess loss or of increasing the coupler size to allow transceivers to be connected directly to them, $H_{1k}(0)$ will decrease exponentially with Δc. Table I shows the values of Eq. 55a and b, expressed in dB. per row, or column, of separation between the transmitter and receiver in four situations.

TABLE I

EXCESS LOSS	TRANSCEIVER COUPLING	EXPONENTIAL PART OF $H_{1k}(0)$, dB per row or column of separation	
		MESH	CIRCULANT
0.0 dB	No	3.0	0.0
0.3 dB	No	3.3	2.3
0.0 dB	Yes	4.8	4.2
0.3 dB	Yes	5.1	4.8

The first row of the table presents the values for couplers that have no excess loss nor any provision for the direct attachment of transceivers, i.e. μ_c and μ_m equal 0.25 and 0.5 respectively. The second row is for couplers that have an excess loss of 0.3 dB. with no provision for transceiver coupling. Rows three and four differ from rows one and two in that the couplers have additional terminals to allow transceivers to be connected to the network through them, rather than by severing links as discussed earlier.

By way of example, for couplers with an excess loss of 0.3 dB and no provision for connecting transceivers to them the exponential part of the propagation loss at a receiver in the same column (or row) as the transmitter but twenty rows (or columns) away from it will be 66 dB for the mesh and 46 dB for the circulant.

For small enough values of μ_c, g_1 will become more strongly dependent upon Δc. That dependence can be evaluated numerically with modest effort but we shall not do so here.

Having determined that, for a receiver located in the same row or column as the transmitter, $H_{1k}(0)$ is exponentially less for the simple mesh network than it is for the circulant network we now consider a receiver for which Δr equals Δc, i.e. one located on a diagonal through the transmitter. For the simple mesh network, $H_{1k}(0)$ did not decrease exponentially with distance from the transmitter for such a receiver. The question is whether it does for the circulant network of Fig. VI-4.

It is expeditious to start the analysis from Eq. 46. With a change of variable and a translation of the integration interval that equation becomes

EQ. 56

$$H_{1k}(f) = \mu \int\limits_{0}^{2\pi}\int \frac{d\theta d\phi}{(2\pi)^2} \frac{\exp(-j\Delta c\theta)}{1 - \beta[\cos(\theta - \phi) + \cos\phi]}$$

which also can be written as

EQ. 57a

$$H_{1k}(f) = \mu \int\limits_0^{2\pi}\int \frac{d\theta d\phi}{(2\pi)^2} \frac{\exp(-j\Delta c\theta)}{1 - \beta v \cos(\phi - \varphi)}$$

where

EQ. 57b

$$v = \sqrt{2(1 + \cos\theta)} \qquad \text{and}$$

EQ. 57c

$$\varphi = \tan^{-1} \frac{\sin\theta}{1 + \cos\theta}$$

The integral on ø can be evaluated to yield

EQ. 58

$$H_{1k}(f) = \mu \int\limits_0^{2\pi} \frac{d\theta}{2\pi} \frac{\exp(-j\Delta c\theta)}{\sqrt{1 - 2\beta^2(1 + \cos\theta)}}$$

Following the same avenue taken earlier to Eq. 52 from Eq. 49 for f equal to zero, Eq. 58 can be transformed into a clockwise contour around the unit circle in the complex z plane. Choosing z to be given by Eq. 48 yields

EQ. 59

$$H_{1k}(0) = \frac{-\mu}{2\pi\beta} \oint \frac{dz z^{\Delta c}}{\sqrt{z}\sqrt{z^2 - (\beta^{-2} - 2)z + 1}}$$

The integrand is an analytic function with branch points at z equal zero, X3 and 1/X3 where

EQ. 60

$$X_3 = \frac{\beta^{-2}}{2} - 1 - \sqrt{\left(\frac{\beta^{-2}}{2} - 1\right)^2 - 1}$$

is one of the two branch points within the unit circle. By the properties of analytic functions, the clockwise integral around the unit circle of the z plane equals the counter clockwise contour integral around the cut between the branch points z=0 and z= X3. Therefore,

112

EQ. 61

$$H_{1k}(0) = \frac{1}{2\pi} \int_0^{x_3} \frac{dx\, x^{\Delta c}}{\sqrt{x}\sqrt{x^2 - (\beta^{-2} - 2)x + 1}}$$

When Δc is large the value of the integral is dominated by values of the integrand for which x is approximately equal to X3. Then the integral can be approximated by

EQ. 62a

$$H_{1k}(0) = K_2 \int \frac{dx\, x^{\Delta c}}{\sqrt{X_3 - x}}$$

where

EQ. 62b

$$K_2 = \frac{1}{2\pi\sqrt{X_3^2 - 1}}$$

This integral can be evaluated to obtain

EQ. 63a

$$H_{1k}(0) = g_2 K_2 X_3^{\Delta c}$$

where

EQ. 63b

$$g_2 = 2\sqrt{X_3} \sum_{i=0}^{\Delta c} \frac{\binom{\Delta c}{i}(-1)^i}{2i + 1}$$

When the couplers have very little excess loss and transceivers are not attached directly to them, i.e. when μ_c and β are nearly 0.25 and 0.5, respectively, g_2 is very weakly dependent upon Δc. Then $H_{1k}(0)$ does not decrease exponentially with increasing Dc. Thus the change from the simple mesh network to the circulant network of Fig. VI-4 has not penalized receivers on the diagonal from a transmitter.

For smaller values of μ_c and μ_m $H_{1k}(0)$ will decrease as $X_3^{\Delta c}$ for the circulant network and as $(2\mu_m)^{2\Delta c}$ for the mesh network. The values, expressed in units of dB per row (or column) of separation, are given in Table II for the same four situations that were considered in Table I.

113

TABLE II

EXCESS LOSS	TRANSCEIVER COUPLING	EXPONENTIAL PART OF $H_{1k}(0)$, dB per row or column of separation	
		MESH	CIRCULANT
0.0 dB	No	0.0	0.0
0.3 dB	No	3.3	0.6
0.0 dB	Yes	6.0	9.5
0.3 dB	Yes	7.0	10.1

More work is needed to determine the range of values of μ_c for which the above approximations are valid but the approximations do suffice to show that the connectivity typified by the circulant network of Fig. VI-4 can increase the value of $H_{1k}(0)$ significantly. However, at least for receivers in the same row (or column) as the transmitter, the values are still rather small for users separated from the transmitter by many columns (or rows).

One means of alleviating this diminution is to employ optical amplifiers in the network. That serves to increase the effective value of μ at the expense of introducing optical noise. The noise model of Section 2.2 provides a framework for evaluating the impact of this noise but the evaluation has not yet been undertaken. In addition, it remains to evaluate the degradation associated with intersymbol interference. The framework for that evaluation is provided in Section 3. These, and the other tasks discussed in the next section are subjects for further investigation

5. FUTURE WORK

When the investigation of robust networks was initiated the very limited ability to implement optical filtering led us to limit our attention to receiver structures that employed either direct, or heterodyne, detection followed by electronic signal processing. As a result of that investigation several severe limitations on the performance of networks using such structures have been identified. Preliminary analysis indicates that the use of predetection optical filtering will ameliorate those limitations and the recent advances in the implementation of optical filters suggests that their use will become realistic.

The advances in filtering are typified by the availability of an optical transversal filter for use at RL-Hanscom. The importance of such filters in robust networks stems from the following conclusions that are contained in Sections 1 through 4 above.

First, in large robust networks, very small variations in the propagation delays of the many different propagation paths results in unacceptable phase interference between the signals arriving at a receiver if narrow band transmitter lasers are employed. No means of ameliorating this effect has been found when such lasers are employed. Consequently, it is necessary to use wide band lasers, or LEDs, for which the signals arriving on the different propagation paths will combine incoherently. The use of these wide band sources dictates that direct detection, rather than heterodyne detection, be employed.

Second, the desired presence of many propagation paths combined with the excess loss of realistic fiber couplers leads to a need for optical amplifiers within the network. Of course, optical noise also is introduced into the network by these amplifiers.

Third, without predetection optical filtering, the full bandwidth of the optical noise will affect the performance that can be achieved by a network user. Since the underlying network access method is frequency division multiplexing, that noise bandwidth will be orders of magnitude greater than the bandwidth of a single user and will sorely limit the performance of the network. With optical filtering, the amplifier noise affecting a receiver can be limited to that contained within the bandwidth of the signal intended for that user which will significantly improve the network's performance.

It follows from the above that future work on robust networks should focus upon the benefits to be derived from the use of optical gain within the network and the use of optical filtering prior to direct detection. That work will involve the theoretical and experimental components described below.

5.1. THEORETICAL INVESTIGATION

Drawing upon the knowledge base already established, the following additional tasks will be undertaken.

1. Combine the results of Section 2 on the propagation of signals and amplifier noise through robust network topologies to determine the performance expressions for robust networks containing optical amplifiers when predetection filtering, matched to the optical signal, is used. This will provide a performance benchmark that cannot be surpassed.

2. Apply the results of 1) to the network used in the experimental testbed and to representative robust networks such as the circulant network discussed in Section 4.

3. Using the results of 2), determine the distribution of optical gain within the network that maximizes the network's performance.

4. Using the results of 2), determine the performance loss that results from suboptimum, but more realistic, distributions of gain within the network.

5. Repeat 1 through 4 when the optical filter bandwidth exceeds that of the matched filter by realistic amounts.

5.2. EXPERIMENTAL INVESTIGATION

The goal of the experimental work will be to guide, correct and validate the theoretical work. It will utilize a small nine node testbed network, an available optical amplifier and a 16 tap optical transversal filter for predetection filtering. The amplifier and filter will operate at a wavelength of 1.5 nm. In order to fully utilize the filter's capability, the length of the links between couplers will be on the order of one meter long, corresponding to a propagation delay of 5 ns.

For initial testing purposes, the network will be configured as a nine node simple square mesh network of the form shown in Fig. VI-3a. Subsequently, it will be reconfigured to have additional connectivity, perhaps as illustrated in Fig. VI-1. The following specific tasks are to be completed during the experimental phase of the investigation.

1. Complete the preliminary design of the testbed.

2. Construct the testbed in a form that allows for testing with a single user pair at a variety of its nodes.

3. Conduct performance measurements on the testbed to validate, guide and correct the performance analysis. Initial measurements will be on a simple square mesh.

REFERENCES:

1. J. G. Proakis, *Digital Communications*, McGraw-Hill Book Company, USA, 1983

2. O. J. Wasem, "Robust Topologies for Passive, Fiber Optic Local Communication Networks", MIT Ph. D. thesis submitted to Dept of Electrical Engineering and Computer Science, MIT, June 1989. Also Available as Technical Report LIDS-TH-1898, August 1989 from MIT's Laboratory for Information and Decision Systems. Work partially supported by RADC Grand SU3531241.

3. L. A. Alterman, " Performance of Fiber Optic Networks with Multiple Paths", MIT S.M.. thesis submitted to Dept of Electrical Engineering and Computer Science, MIT, November 1988. Work partially supported by RADC Grand SU3531241.

UNIDIRECTIONAL FIBER LINK   PASSIVE COUPLER   OPTICAL AMPLIFIER   TRANSCEIVER
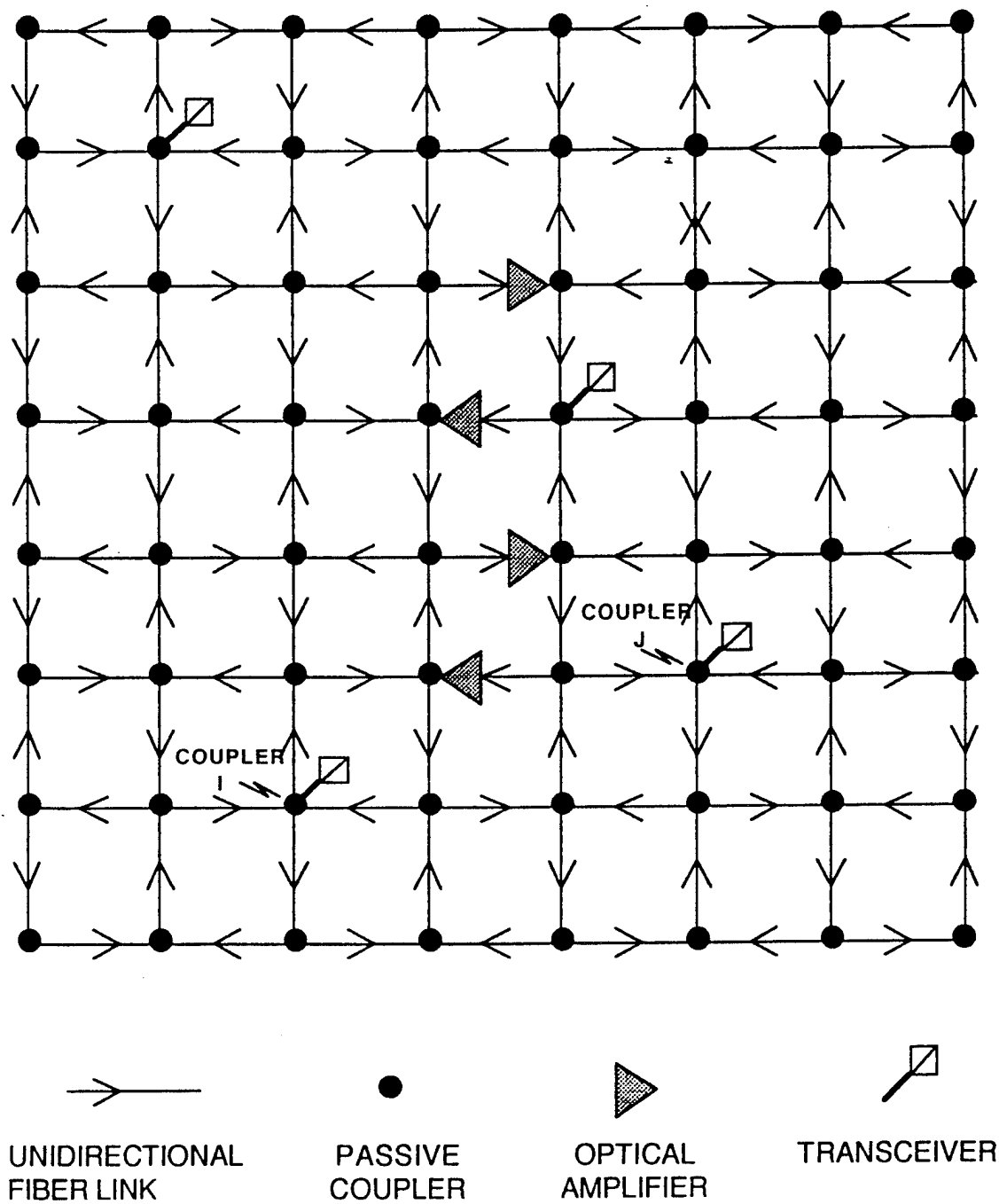
EXAMPLE OF A ROBUST NETWORK

FIGURE VI-1

$$\sum_i \left| A_{k_i} \; p(t - iT) \right|^2$$

$$Sn(f) = \frac{No}{2}$$
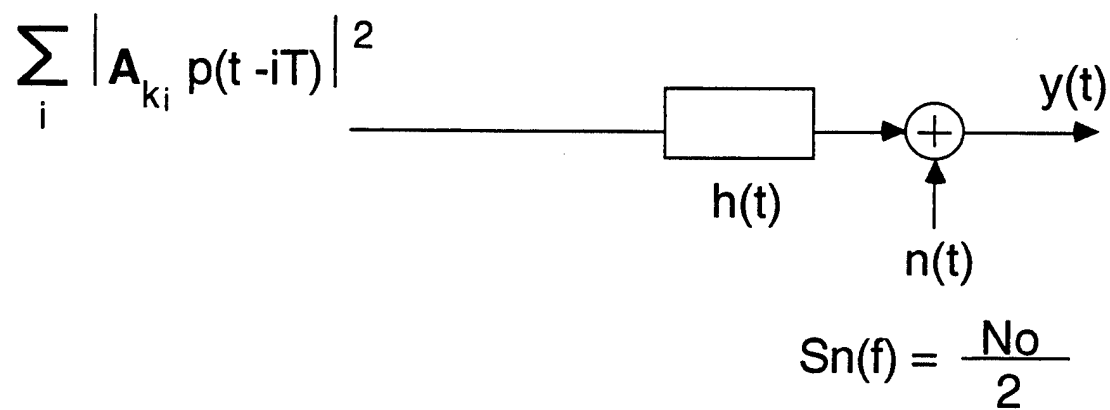
MODEL FOR DIRECT DETECTION

FIGURE VI-2
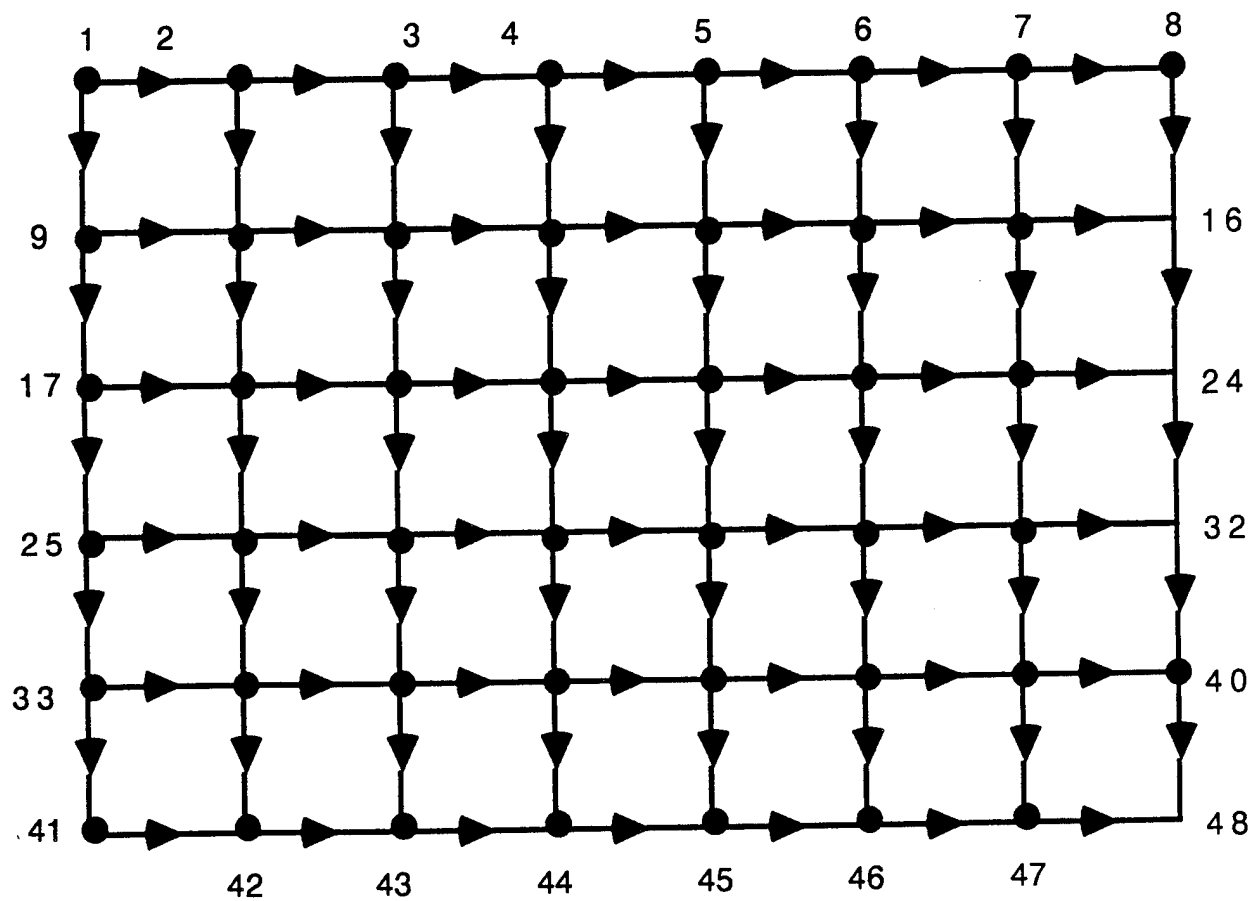
Simple Mesh Network of Eight Rows
and Six Columns

FIGURE VI-3a

"Wrapped Around" Mesh Network of Eight Rows and Six Columns.
This Network is a Circulant

FIGURE VI-3b

$$
C = \begin{bmatrix}
0 & 1 & 0 & 0 & 1 & 0 & 0 & 0 & 0 & 0 & 0 & 0 \\
0 & 0 & 1 & 0 & 0 & 1 & 0 & 0 & 0 & 0 & 0 & 0 \\
0 & 0 & 0 & 1 & 0 & 0 & 1 & 0 & 0 & 0 & 0 & 0 \\
0 & 0 & 0 & 0 & 0 & 0 & 0 & 1 & 0 & 0 & 0 & 0 \\
0 & 0 & 0 & 0 & 0 & 1 & 0 & 0 & 1 & 0 & 0 & 0 \\
0 & 0 & 0 & 0 & 0 & 0 & 1 & 0 & 0 & 1 & 0 & 0 \\
0 & 0 & 0 & 0 & 0 & 0 & 0 & 1 & 0 & 0 & 1 & 0 \\
0 & 0 & 0 & 0 & 0 & 0 & 0 & 0 & 0 & 0 & 0 & 1 \\
0 & 0 & 0 & 0 & 0 & 0 & 0 & 0 & 0 & 1 & 0 & 0 \\
0 & 0 & 0 & 0 & 0 & 0 & 0 & 0 & 0 & 0 & 1 & 0 \\
0 & 0 & 0 & 0 & 0 & 0 & 0 & 0 & 0 & 0 & 0 & 1 \\
0 & 0 & 0 & 0 & 0 & 0 & 0 & 0 & 0 & 0 & 0 & 0
\end{bmatrix}
$$

Eq. 27a for Network Fig. 3a

FIGURE VI-3c

$$
C = \begin{bmatrix}
0 & 1 & 0 & 0 & 1 & 0 & 0 & 0 & 0 & 0 & 0 & 0 \\
0 & 0 & 1 & 0 & 0 & 1 & 0 & 0 & 0 & 0 & 0 & 0 \\
0 & 0 & 0 & 1 & 0 & 0 & 1 & 0 & 0 & 0 & 0 & 0 \\
0 & 0 & 0 & 0 & 1 & 0 & 0 & 1 & 0 & 0 & 0 & 0 \\
0 & 0 & 0 & 0 & 0 & 1 & 0 & 0 & 1 & 0 & 0 & 0 \\
0 & 0 & 0 & 0 & 0 & 0 & 1 & 0 & 0 & 1 & 0 & 0 \\
0 & 0 & 0 & 0 & 0 & 0 & 0 & 1 & 0 & 0 & 1 & 0 \\
0 & 0 & 0 & 0 & 0 & 0 & 0 & 0 & 1 & 0 & 0 & 1 \\
1 & 0 & 0 & 0 & 0 & 0 & 0 & 0 & 0 & 1 & 0 & 0 \\
0 & 1 & 0 & 0 & 0 & 0 & 0 & 0 & 0 & 0 & 1 & 0 \\
0 & 0 & 1 & 0 & 0 & 0 & 0 & 0 & 0 & 0 & 0 & 1 \\
1 & 0 & 0 & 1 & 0 & 0 & 0 & 0 & 0 & 0 & 0 & 0
\end{bmatrix}
$$

Eq. 27b for Network Fig. VI-3b

(a) Details of Connections between Couplers

(b) Network Topology for N Equal to 36.
Each Link Represents a Pair of Fibers

Structure of Network Described by the Circulant Connection Matrix of Eq. 40

FIGURE VI-4
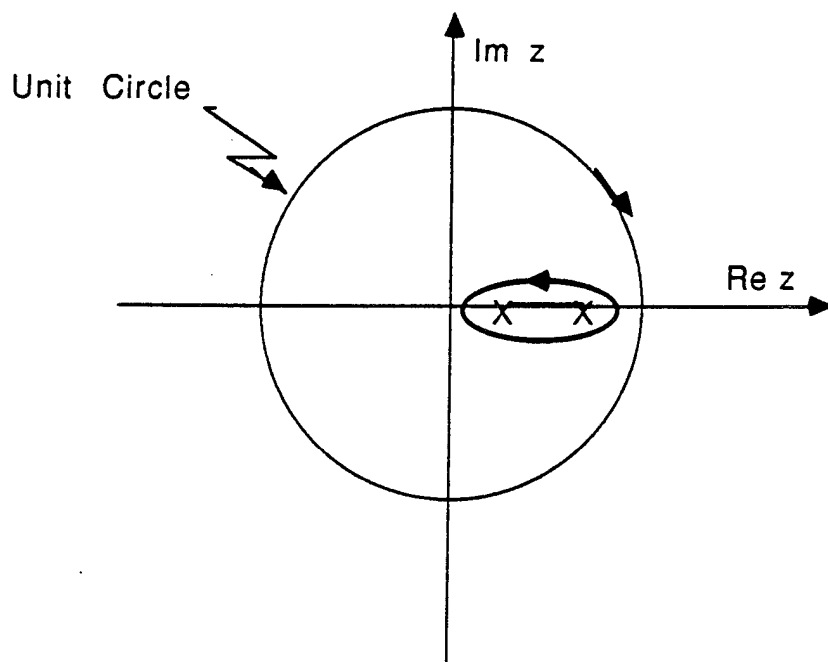
Contour Integral for Evaluating Eq. 47

FIGURE VI-5

INTRODUCTION

The Air Force has a high interest in nonlinear optical materials and devices. Research at the Solid State Division is centered around the development of efficient, high speed nonlinear optical materials that operate at relatively low laser intensities. Both photorefractive and resonant nonlinear optical interactions are being studied. Resonant interactions are the most promising, but have not yet realized their full potential because of the presence of broadening mechanisms that are present in most materials: for example, crystal fields in solids, and collisions in vapors. To eliminate these complications, the nonlinear optical properties of an atomic beam are being studied. This will enable a systematic investigation, both experimental and theoretical, of the physics of resonant nonlinear optical interactions. Such studies are ultimately expected to result in the development of greatly improved low power nonlinear optical materials and devices, which will have applications in optical computing and optical signal processing.

Consulting efforts have concentrated on solving the numerous problems that have arisen in the development of a supersonic atomic beam for nonlinear optical interactions. In particular, frequent oven failure and low Mach number were the major problems addressed.

EXTERNALLY HEATED SUPERSONIC OVEN

The two most common failure modes of the supersonic oven were breaks in the heater wire and destruction of the nozzles by electrical arcing. Both of these failure modes necessitated complete disassembly and rebuilding of the oven which translated into unacceptably long periods of down time. To greatly reduce this down time, it was decided to redesign the oven so that it could be heated by elements located external to the vacuum system. This new oven design, to be described below, completely eliminated the electrical arcing problem and greatly reduced the down time related to heater element breakage.

A photograph of the new supersonic oven assembly appears in Figure VII-1. This assembly consists of a nozzle section (top) and an oven section (long tube). The nozzle section consists of a replaceable nozzle screwed into the innermost recess of a conically tapered vacuum flange, as shown. This conical taper (about 20°) was necessary so that the nozzle could be heated to 1000° C while the nozzle flange was bolted to a water cooled adapter flange on the vacuum system. The oven section consisted simply of a hollow tube containing sodium.

Separate heater elements were wound on the nozzle and oven sections so that the nozzle could always be kept 100°C hotter than the oven. This was necessary to prevent condensation of sodium in the nozzle which would plug it. In addition, crumbled nickel foil was inserted behind the nozzle to prevent the nozzle being plugged with liquid sodium splattered from the oven section.

Figure VII-2 shows the completely assembled supersonic beam mounted on a glass tee. The glass tee was used instead of the observation region of the previous design so that the dynamics of the atomic beam could be monitored closer to the nozzle.

INVERTED SUPERSONIC NOZZLE ASSEMBLY

The inability to achieve higher Mach numbers in the supersonic beam apparatus is most likely caused by the presence of background vapor in the vacuum system. To eliminate this vapor as much as possible, the nozzle section of the atomic beam apparatus was inverted so that the nozzle projects into the vacuum system. This inverted nozzle design is shown in Figure VII-3. By projecting the nozzle into the vacuum system, it is possible to place vapor gettering cold traps much closer to the atomic beam source. In addition, this design also allows observation regions to be placed much closer to the source, thereby greatly increasing the atomic density and, therefore, the optical absorption.

To avoid the use of heating elements inside the vacuum system, the inward projecting nozzle section consists of two concentric cylinders. This is shown in Figure VII-3(b). With this design, heating elements located outside the vacuum can be placed as close as 1 cm to the nozzle.

SUPERSONIC ATOMIC BEAM RESULTS

So far, using the improved atomic beam oven design, we have experimentally observed resonant laser beam absorption as high as 80%, with no Doppler compensation, at a distance of 15 cm from the nozzle. This is close to that required for nonlinear optics studies. In addition, a Mach number approaching 5 was observed, which indicates that an absorption approaching 100% should be achievable with Doppler compensation. The system is now ready for preliminary nonlinear optical measurements.

CONSTRUCTION OF HEAT PIPE CELL

In order to permit direct comparison between the atomic beam studies and previous vapor experiments, several heat pipe sodium vapor cells were also constructed. Heat pipe cells are preferred over sealed cells because the sodium vapor does not come into direct contact with the cell windows. This prevents sodium attack of the cell windows and permits anti-reflection window coatings to be used. One of the heat pipe cells was fitted with side viewports to allow observation of the fluorescence induced by laser excitation. A picture of the cell is shown in Figure VII-4. Observation of the cell is easily achieved as shown in Figure VII-5. This has allowed for greater understanding of some of the mechanisms occurring inside the sodium cell.

ELECTRO-OPTIC MODULATORS

One method of testing the nonlinear material is by the generation of optical sidebands by mixing both optical and radio frequencies in the nonlinear crystal. In order to initiate wave mixing, optical modulators have been specially designed, fabricated and evaluated.

The crystal material chosen for these modulators was lithium tantalate $LiTaO_3$. An updated, oriented crystal of lithium tantalate was obtained and is shown in Figure VII-6. The crystal measurements were 22mm long, 20mm wide and 1mm thick. The crystal was cut on a semiconductor slicing machine into pieces 1mm x 1.5mm x 10mm long. Only a few pieces were obtained because the original crystal partially shattered during the cutting process. The remaining pieces were then mounted, ground and polished using the mount shown in Figure VII-7.

A prototype modulator was designed, fabricated and tested. In order to test these units a Fabry-Perot interferometer (Figure VII-8) had to be assembled. Preliminary measurements were made with and without modulation to determine operating efficiency (Figure VII-9). Modulation efficiency on the first model was found to be quite low. As a first attempt, an unplated $LiTaO_3$ crystal was placed in the gap of the resonant ring modulator. Efficiency was approximately 5%. It was apparent that the electric fields were not completely penetrating the high dielectric crystal (e=43). In order to improve the electric field penetration is was decided to put a metal coating on the crystal. A coating of chromium was first deposited on the crystal "Z" faces, followed by a coating of gold. The next problem to be solved was mounting the crystal in the resonator gap. Two approaches were tried. The first attempt made was to indium solder the plated crystal to the copper ring. This proved to be very difficult as the indium refused to flow very smoothly, although a working model was finally achieved. Another approach was to use silver paint. With a great deal of care, two resonators were constructed with the crystals cemented in place using silver paint. The conductive paint has the advantage of being able to easily flow and fill the voids between the crystal and the copper ring. All three resonators have been tested and have shown efficiencies of 100%, total carrier suppression (Figures VII-10a, VII-10b).

Projected atomic beam experiments using sodium suggested a need for a single sideband electro-optic modulator at 1770 Mhz. All previous experimentation was directed to developing devices in the 850 Mhz region. Devices in this region were fabricated routinely with total suppression of the fundamental.

The first attempts to raise the operating frequency of the modulator involved reducing the cavity dimensions. This approach was taken since the operating frequency is determined by the shunt capacity of the crystal and the inductance of the ring. The ring diameter was reduced to the smallest practical size, but the operating frequency of the modulator refused to go above 1500 Mhz. Following this, it was decided to reduce the dimensions of the crystal as well, from 0.040" x 0.040" x 0.40" to 0.20" x 0.20" x 0.40". Unfortunately, the saw cut crystals proved to be too damaging to

127

the beam quality to be used effectively in the experiment. Thus, we chose to grind the crystals down to the appropriate size instead of sawing in order to minimize crystal damage. Crystals were successfully ground down to the desired dimensions. These crystals were end polished, chromium plated, then followed by copper. These devices were assembled and tested. Performance was checked at 1770 Mhz and found to have 100% carrier suppression.

All previous electro-optic modulator designs had been at higher frequencies (850-1700 Mhz). Construction had been mainly single turn loops. Operation in the 150 Mhz region necessitated the use of a multi-turn coil to resonate the crystal capacity at the desired frequency. A piece of $LiTaO_3$ was cut and the end faces polished to dimensions of 0.04" high x 0.070" wide x 0.4" long. Both broad faces were sputtered first with chromium then with gold. Crystal capacity was measured at approximately 7 pf and an appropriate coil was wound to resonate the crystal at the operating frequency. Two brass tabs the same size as the crystal were soldered to the ends of the coil Figure VII-11. These two brass pieces form the nest into which the $LiTaO_3$ crystal is fastened with silver paint. Tuning is accomplished by threading a copper rod into the tuning inductor. The complete low frequency modulator is shown in Figure VII-12. The unit is tunable over the frequency range 135-223 Mhz. The coil inductance is 0.15 microhenries. Crystal capacitance was approximately 7 pf and the "Q" of the system is approximately 100. Complete carrier suppression is obtained with 1 watt of drive.

An effort was made toward the development of a waveguide version of an electro-optic modulator, in the hope of extending the operating frequency of these modulators to approximately 10 Ghz. All previous modulators have been constructed using lumped circuitry. This is the first attempt using a waveguide structure.

A ridged waveguide cavity structure (Figure VII-13) has been proposed as a means of concentrating the electric field across the electro-optic modulating crystal. Figure VII-14 shows the cavity and impedance matching section. Optical access to the crystal is provided by holes drilled on the sides of the cavity. Microwave coupling into the cavity is accomplished by means of a longitudinal slot milled into the narrow face of the cavity. Preliminary microwave measurements had been made to determine frequency shift of the cavity vs. ridge separation.

The necessary test equipment and waveguide components were obtained and measurements were made on a number of different microwave cavities. Figure VII-15 shows a microwave test setup consisting of a Hewlett Packard sweep oscillator model 8350B a coaxial to waveguide crystal detector. The detected output was displayed on an oscilloscope. An empty X-band cavity was constructed with dimensions 0.5" x 1.0" x 1.3". A slot was cut into the side and coupling was optimized. The operating frequency was measured to be 10,100 Mhz. Ridges were now placed inside the cavity to determine their effect on the frequency shift of the cavity, which turned out to be approximately 1,500 Mhz. As soon as the crystal was inserted into the cavity it

became immediately obvious that the frequency shift was so great to a lower frequency that we would have to start at a much higher operating frequency in order to end up with an operating frequency of 10 Ghz.

Another cavity was fabricated with a frequency of 18,600 Mhz. The suggestion was made to install two ridges of various separations (Figure VII-16) simulating the tuning effect of crystal capacitance. This would enable the cavity operating frequency to be tracked more easily to its final value. Measurements were made at various separations and the final conclusion reached was that the natural capacitance of the crystal would drive the operating frequency of the cavity much lower than the desired 10 Ghz, thereby making this design unusable at higher frequencies.

In the past we had constructed ring resonators in the 1770 Mhz region with dimensions 0.020" long x 0.281" diameter. It was decided to fabricate smaller versions of this structure to see what would be the highest possible operating frequency that could be obtained. The cylindrical geometry has many advantages. The machining is straight forward, the electric field is concentrated mainly in the gap, and the structure is ideal for loop coupling the electromagnetic energy into the resonator.

A series of cavities was constructed with diameters ranging from 0.25" to 0.10" (Figure VII-17). A suitable piece of lithium tantalate was found and cemented into the cavity with silver paint. A test set-up (Figure VII-18) consisting of a HP sweep generator, model 8350B, a coaxial crystal detector and an oscilloscope, was used to determine the resonant frequencies of the cavities. The measurements were simplified by observing the cavity in transmission instead of reflection, thereby eliminating the need for a directional coupler to monitor the reflected signal. The results are shown in Table 1. We have looked into the possibility of electronically tuning a ring resonator. Varactor tuning will be used in order to compensate for the frequency shift caused by the change of dielectric constant of the lithium tantalate material. This change is due to the increased temperature caused by the heating from the incident laser beam and the r.f. energy supplied to drive the modulator. In order to make a modulator of this type, a practical operating device, it will be necessary to correct the frequency shift that is inherent in its operation. The loss mechanisms both optical and radio frequency in the lithium tantalate are responsible for a temperature increase and a corresponding change in dielectric constant, hence a frequency shift which in this case amounts to approximately 2% or 35 Mhz at the operating frequency of 1772 Mhz. Since these devices are relatively narrow band with "Q's" of approximately 150 (band with 12 Mhz), this heating, detuning frequency shift makes it difficult to maintain resonance conditions for optimum carrier suppression.

Varactor diodes (voltage variable capacitors) offer a unique means of controlling the resonant frequency of a tuned circuit by the application of a variable d.c. voltage applied in the reverse direction to the varactor diode. Junction capacity varies with the applied d.c., thereby controlling the frequency of the tuned circuit.

Typical varactor diode performance is shown in Figure VII-19. A varactor diode has been mounted on a ring resonator (Figure VII-20), and measurements will be made. It will be necessary to evaluate the tuning range, effect of Q of the circuit, and breakdown voltage of the diode with combined d.c. bias and r.f. drive. A few varactor diode samples were obtained, and one of the diodes was mounted across the lithium tantalate crystal. It was necessary to include a chip capacitor in series with the varactor diode so that reverse bias voltage could be applied to the diode (Figure VII-21). Cavity measurements with and without the diode were made in order to check what effect the diode had on the cavity "Q". The "Q" or the figure of merit of the cavity being defined as the operating frequency divided by the full height, half maximum. There was no serious degradation of "Q", so the next step was to apply reverse bias to the diode and check the tuning range. The following results were obtained:

Reverse Bias Voltage	Frequency	"Q"
- 18.6 V	1670 Mhz	92
- 1.1 V	1575 Mhz	120
Frequency Shift - 95 Mhz		

This tuning range was more than necessary to compensate for the 35 Mhz thermal drift. At this point, it was decided to check the optical carrier suppression by applying more drive power to the device. Unfortunately, at higher r.f. drive power, the voltage across the varactor diode exceeded the breakdown voltage thereby limiting its usefulness.

A voltage tunable electrooptic modulator with varactor diodes having breakdown voltages of approximately 30 volts was fabricated and tested. Performance was improved but not to the point of 100 percent carrier suppression before breakdown. In an attempt to improve the performance, we decided to place the tuning diode across a portion of the cavity so that the diode was affected by part of the r.f. field. A copper cavity was constructed for this purpose, having posts around its circumference, in order to allow the diodes to be placed across different amounts of the r.f. field. However, even with this addition, we were still unable to achieve both suppression and tunability.

A measurement was made of the dielectric constant as a function of temperature on a piece of lithium tantalate 0.40" x 0.40" x 0.750". This measurement was made to determine the capacitance/temperature change necessary to explain the 35 Mhz shift we have observed during operation. The measurement was made by placing the sample on a hot plate with suitable electrodes and then connected to a "Q" meter. Tuning of the vernier capacitance control in order to compensate for the capacitance change of the sample when heated produced $\Delta C/\Delta T$ (.04pf/$^\circ$C) 35 Mhz shift at 1770 Mhz (within 2%), which corresponds to a 0.32 pf capacitance change or a temperature rise of 8°C.

We have been taking a closer look at the persistent problem of the thermal detuning of the resonator frequency. Previous measurements have shown a capacitance change of .04pf/^{O}C inherent in the lithium tantalate crystal. At the present time the resonator is mounted in a Teflon cylinder inside a copper tube. The main consideration for this was minimizing the radio frequency loss so that we could obtain the highest "Q" possible. Unfortunately, this structure did not allow any thermal sink for heat generated in the crystal. The problem is to try and remove the heat generated in the lithium tantalate crystal in such a way as not to drastically degrade the r.f. performance of the resonator. We have decided to try replacing the Teflon support ring with one made from boron nitride, a material with comparable dissipation factor and appreciably greater thermal conductivity. A cylinder of boron nitride 1.5" long was machined to replace the Teflon support. Radio frequency measurements made on this structure produced the following results.

	Q
TEFLON	123
BORON NITRIDE	100

Frequency measurements were made with both Teflon and boron nitride. The frequency drift with Teflon was approximately 30 Mhz after 2 minutes. Another measurement was made after boron nitride substitution. At the end of a 10 minute period, the frequency had shifted 10 Mhz.

SUMMARY

In this report we have discussed the work completed during the term of the contract. We have completed the design, construction and testing of a new supersonic beam that solves many of the recurring problems with the older models, such as electrical arcing. In addition, we have discussed the design, construction and testing of several electro-optical modulators for use with the nonlinear optical experiments. Specifically, we are able to modulate laser beams at very high frequencies (1770 Mhz) and are currently attempting higher frequencies.

TABLE 1

DIAMETER	RESONANT FREQUENCY (Mhz)
0.250	3,061
0.200	3,700
0.175	4,100
0.150	5,496
0.125	6,300
0.100	7,093

FIGURES

Photograph of supersonic oven assembly.

FIGURE VII-1
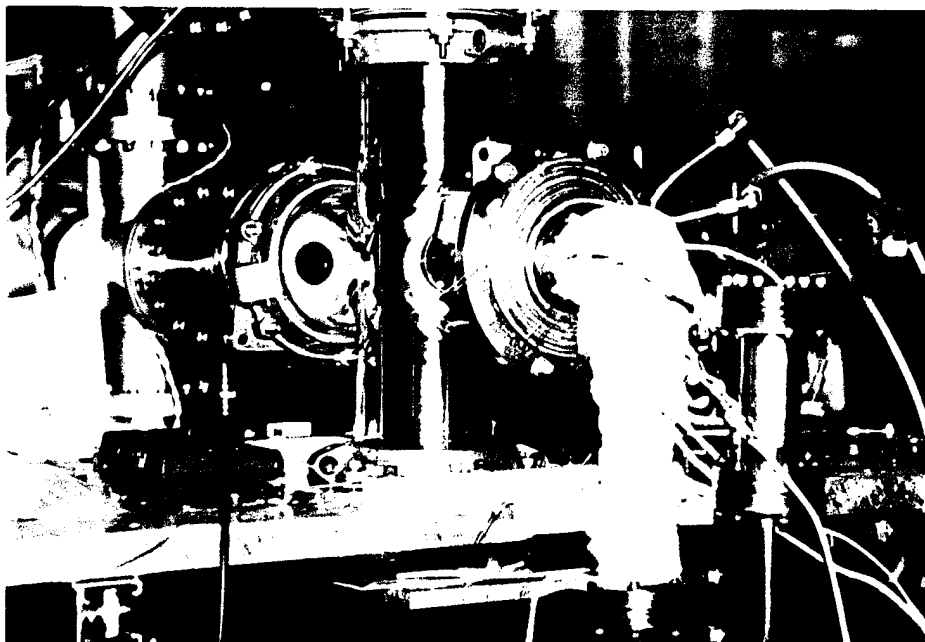
Photograph of supersonic oven wound with heater wire and bolted to observation tee.

FIGURE VII-2

(A)
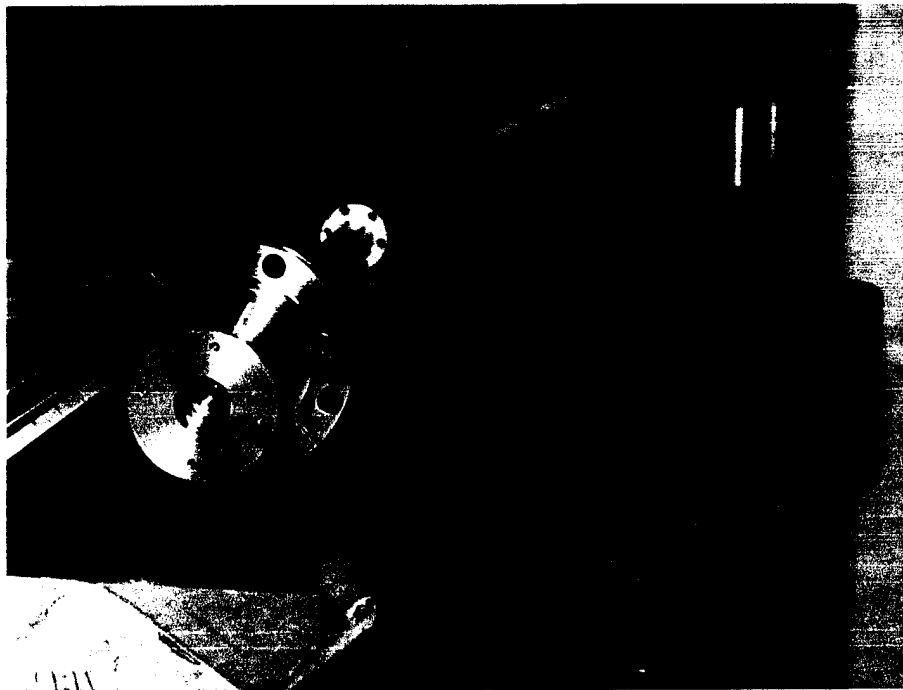
(B)
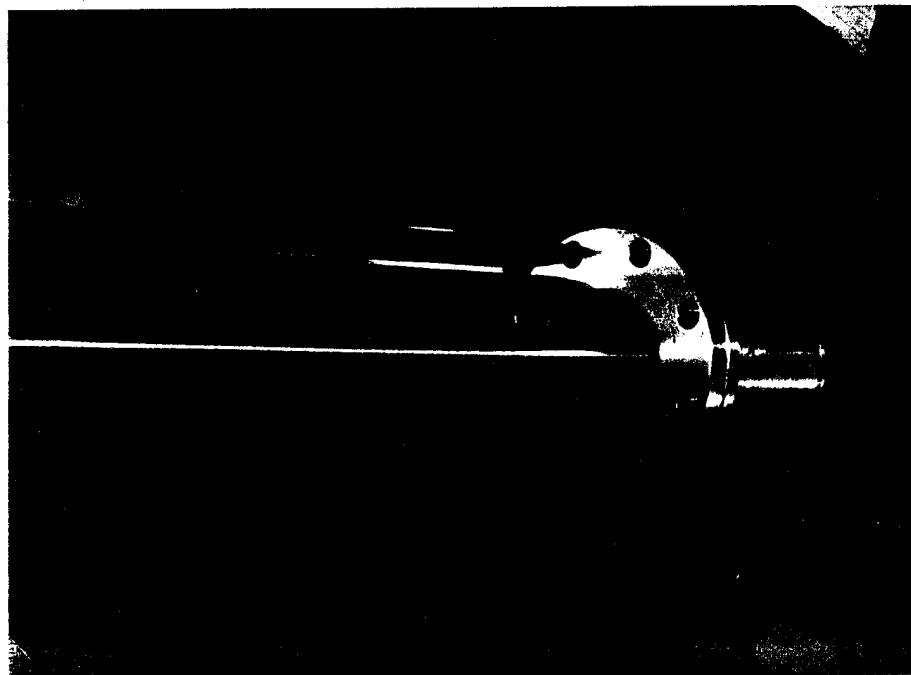
Photograph of inverted supersonic nozzle/oven assembly
a) Vacuum side view.   b) Atmosphere side view.

FIGURE VII-3

136
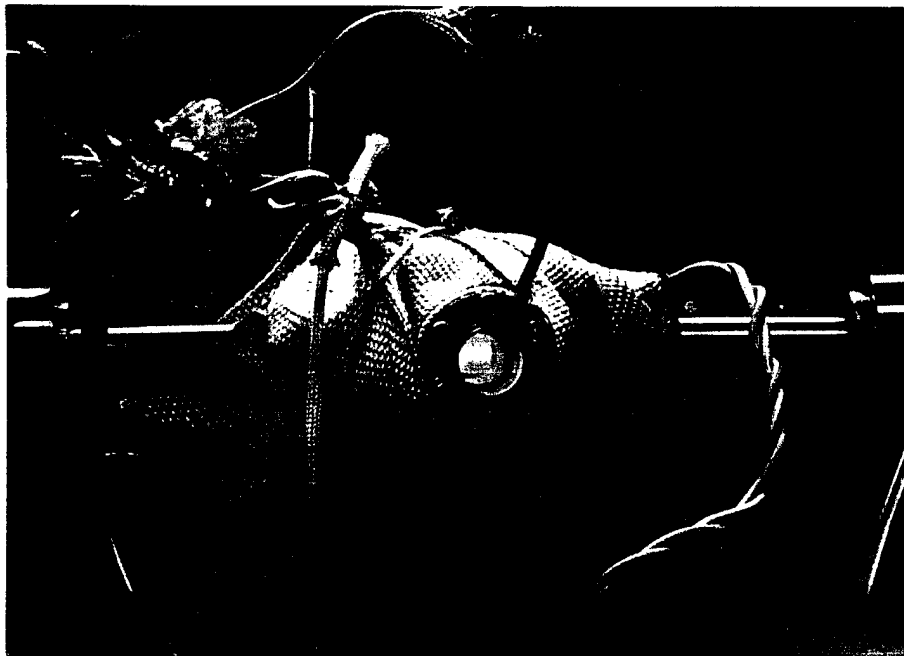
Photograph of heat-pipe cell with viewing port.

FIGURE VII-4
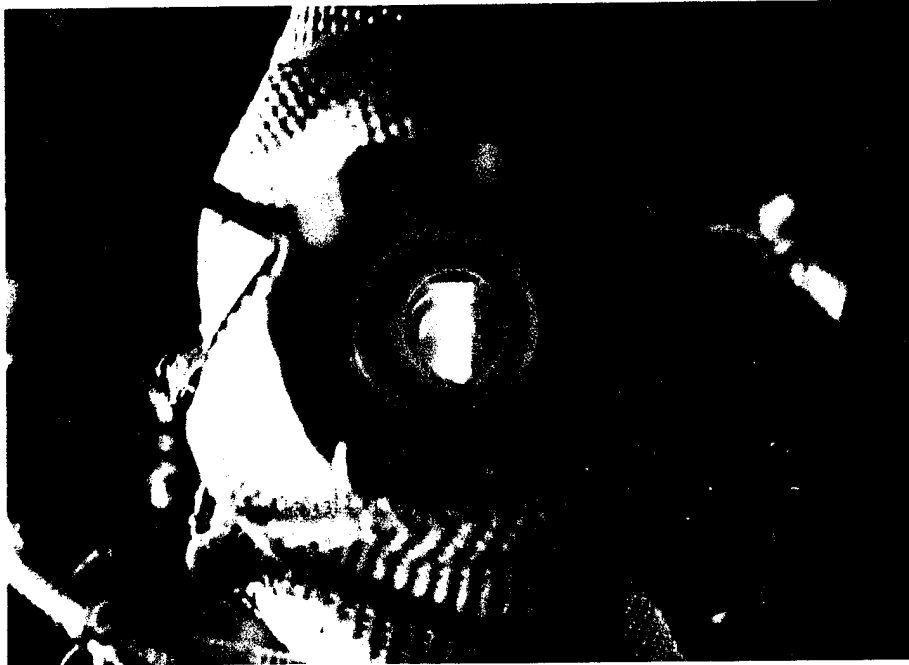
Closeup of laser beam passing through heat-pipe cell.

FIGURE VII-5
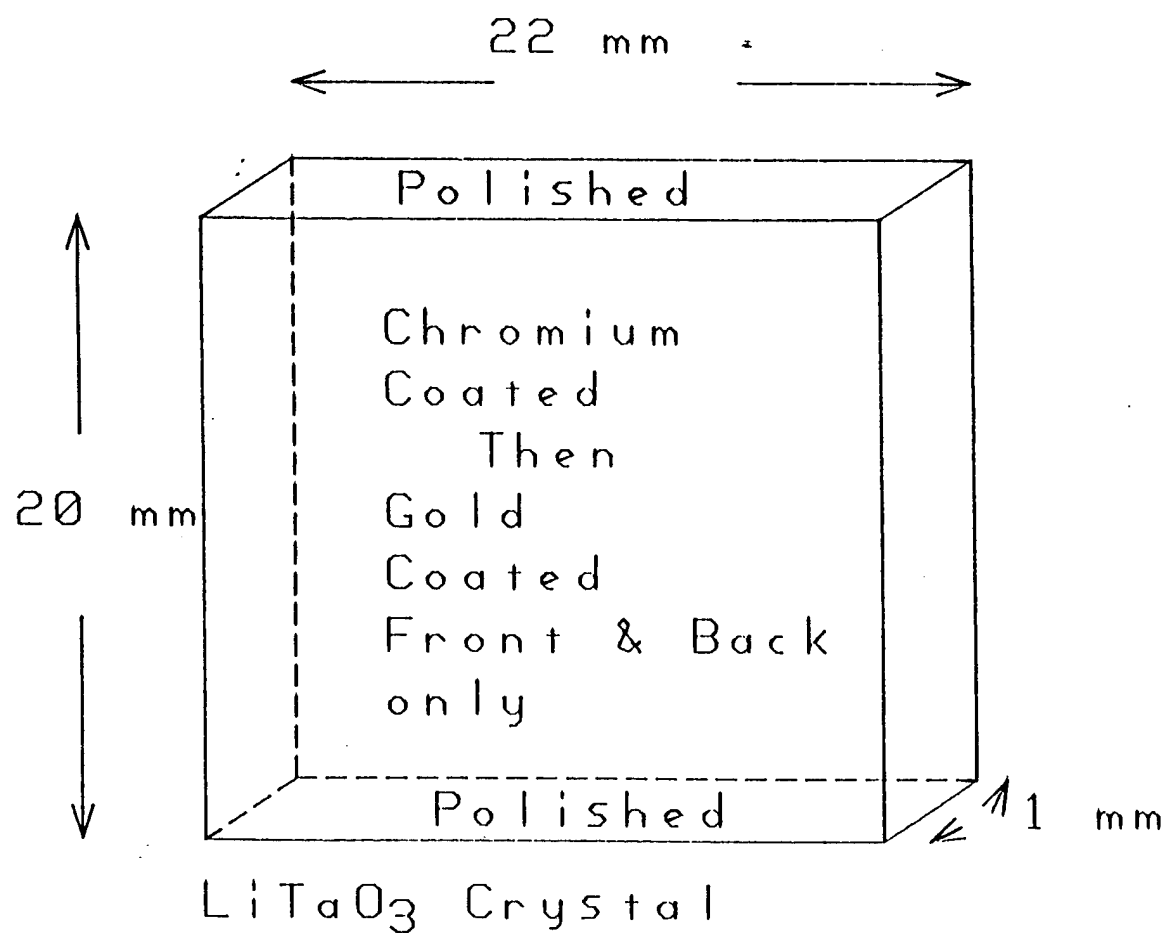
FIGURE VII-6
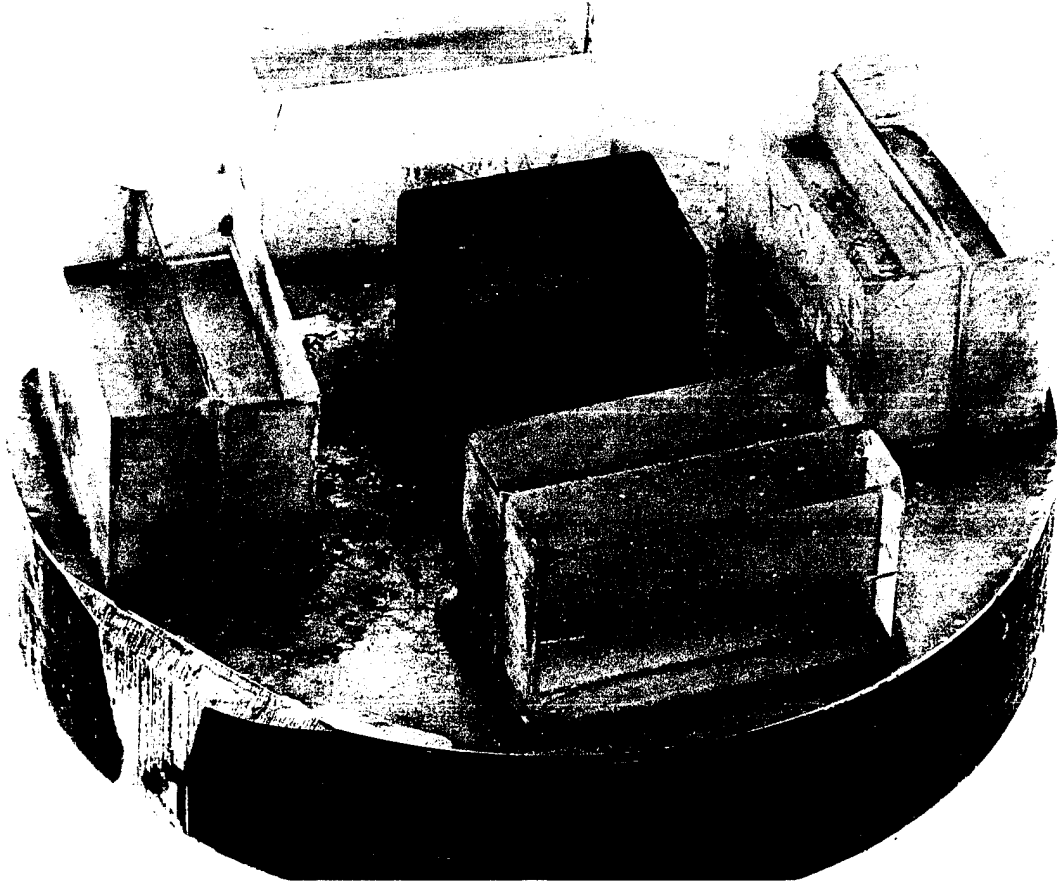
Polishing fixture for 1mm x 20mm x 22mm LiTaO$_3$ Crystals.

FIGURE VII-7
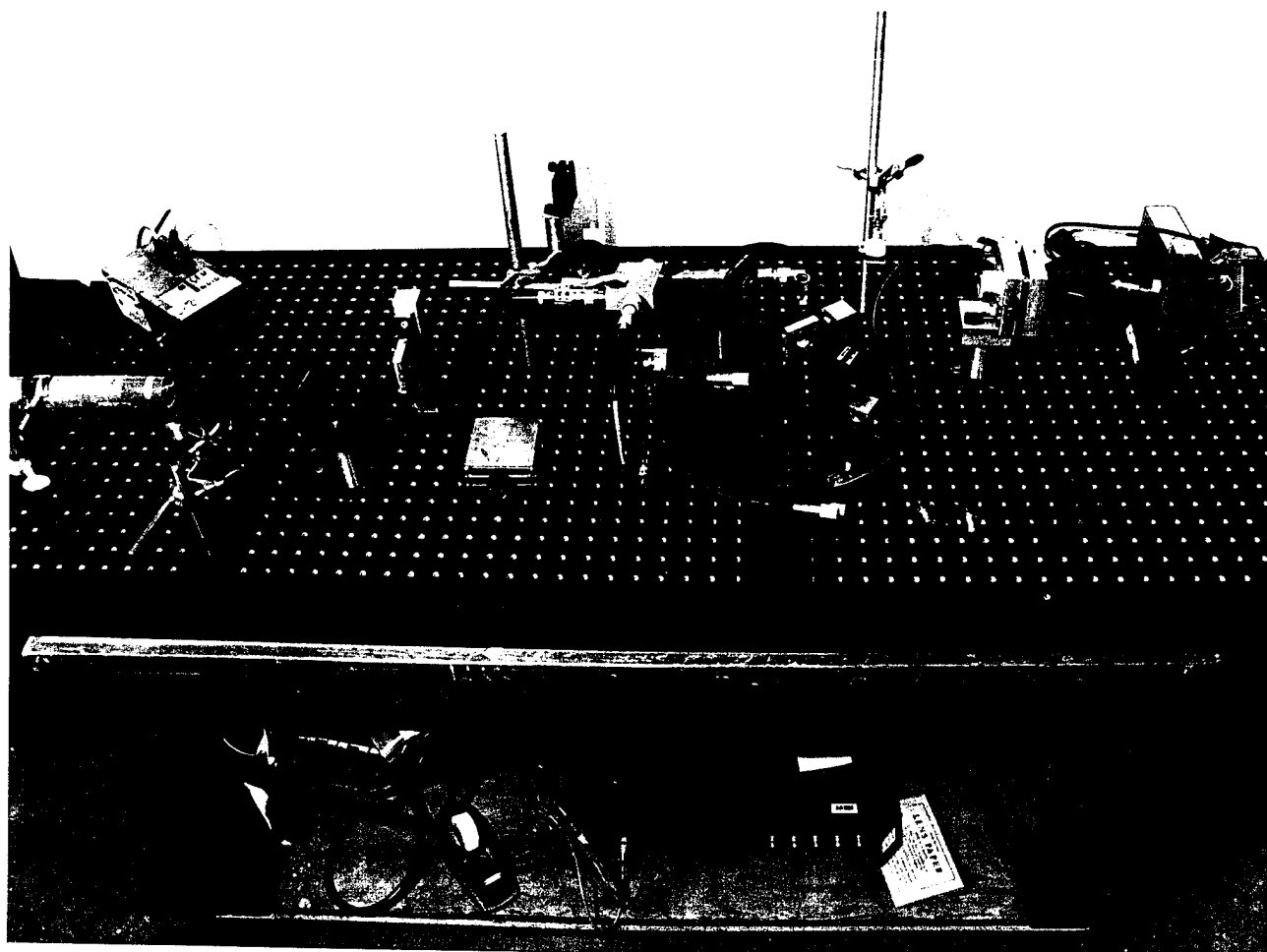
FIGURE VII-8
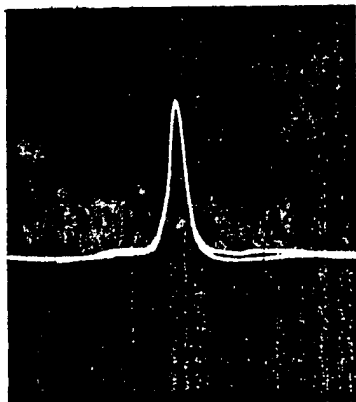
UNMODULATED CARRIER 6328 nm
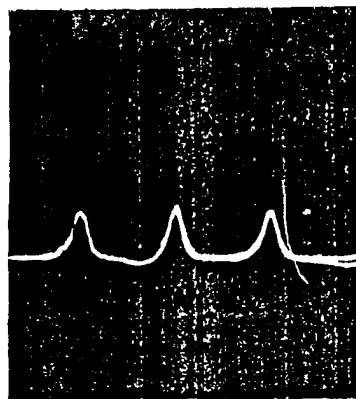
MODULATED CARRIER WITH SIDEBANDS. MODULATION FREQUENCY 880 MHz

FIGURE VII-9

142
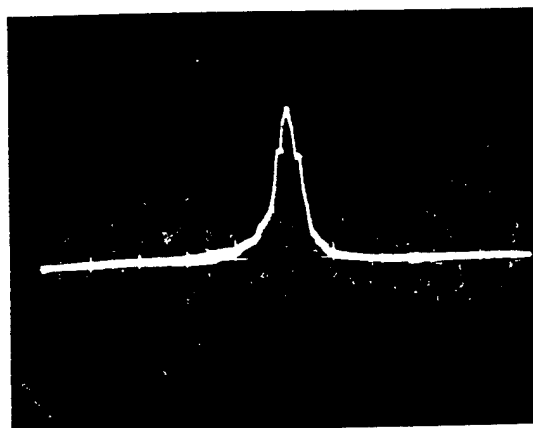
0% CARRIER SUPPRESSION
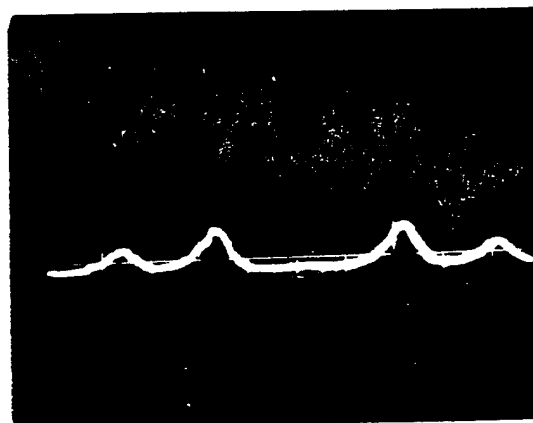
100% CARRIER SUPPRESSION

FIGURE VII-10

143
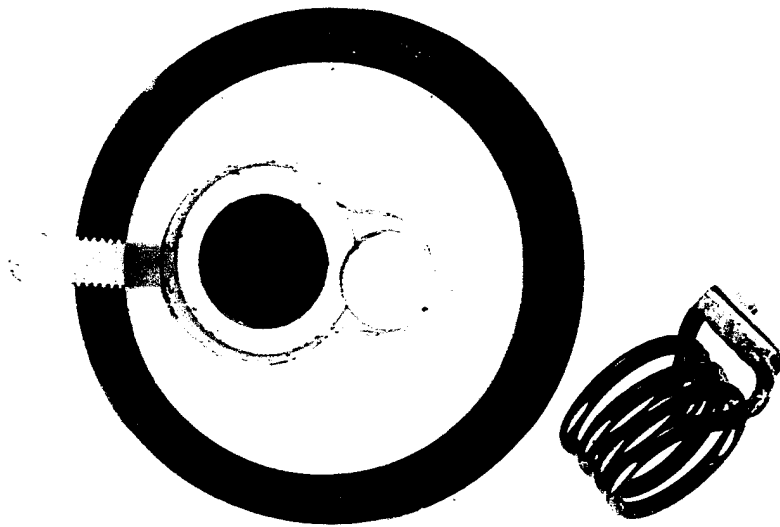
FIGURE VII-11

FIGURE VII-12

END VIEW OPEN CAVITY
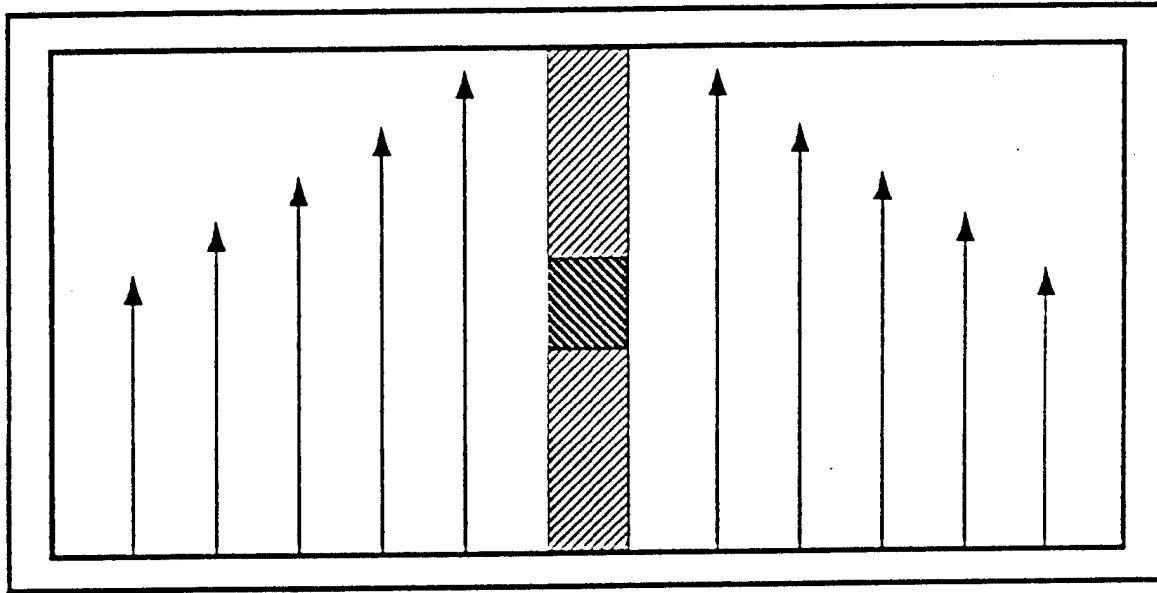
▨ LiTaO CRYSTAL

↑ ELECTRIC FIELD

FIGURE VII-13
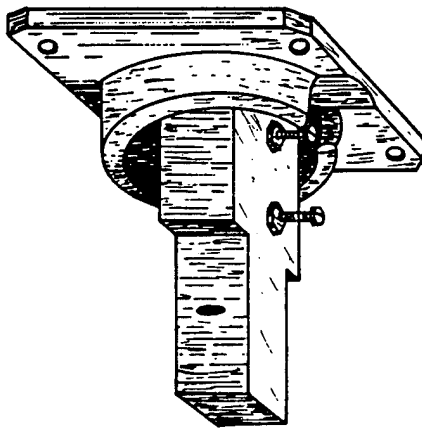
FIGURE VII-14
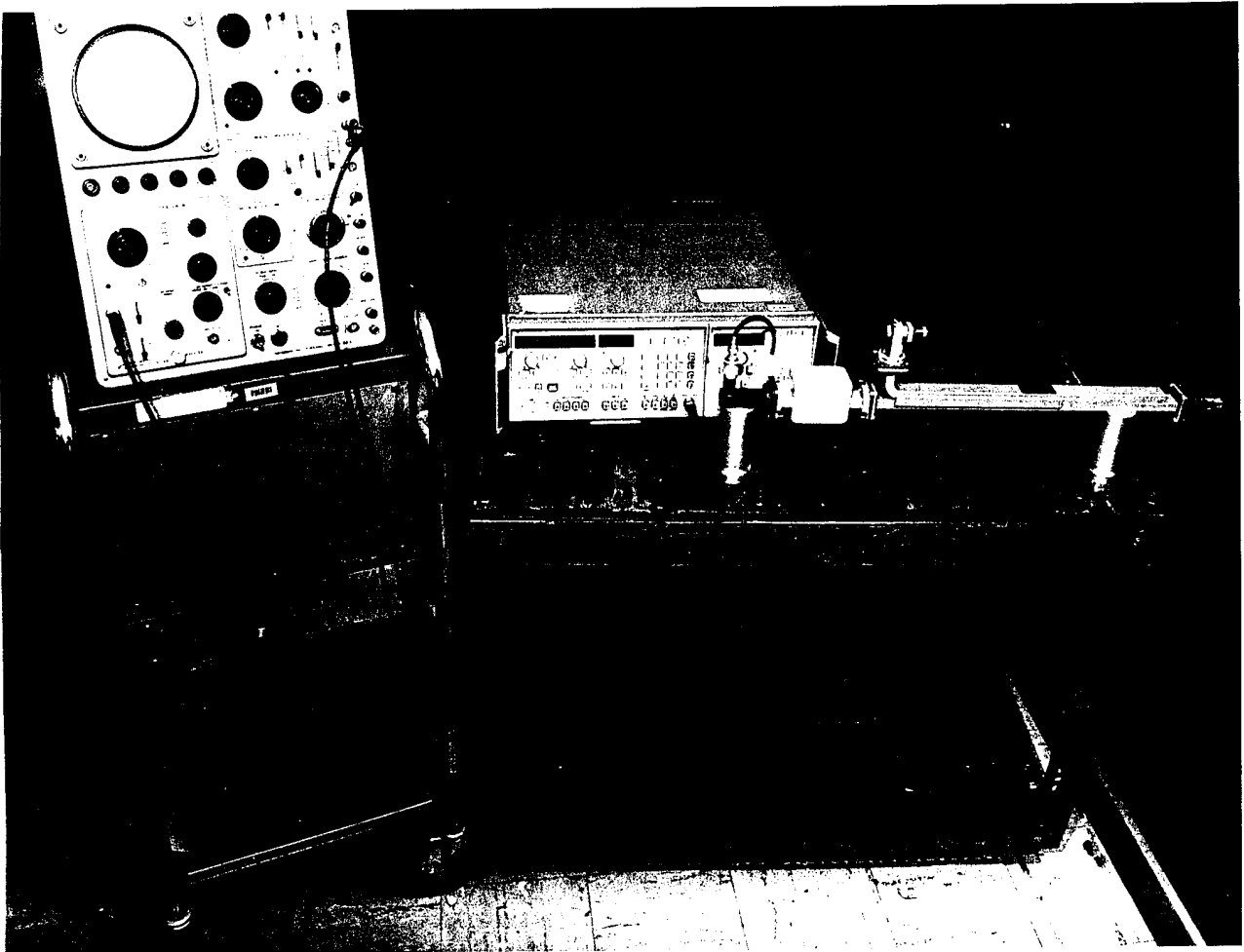
FIGURE VII-15

VARIABLE SEPARATION TEST PIECE
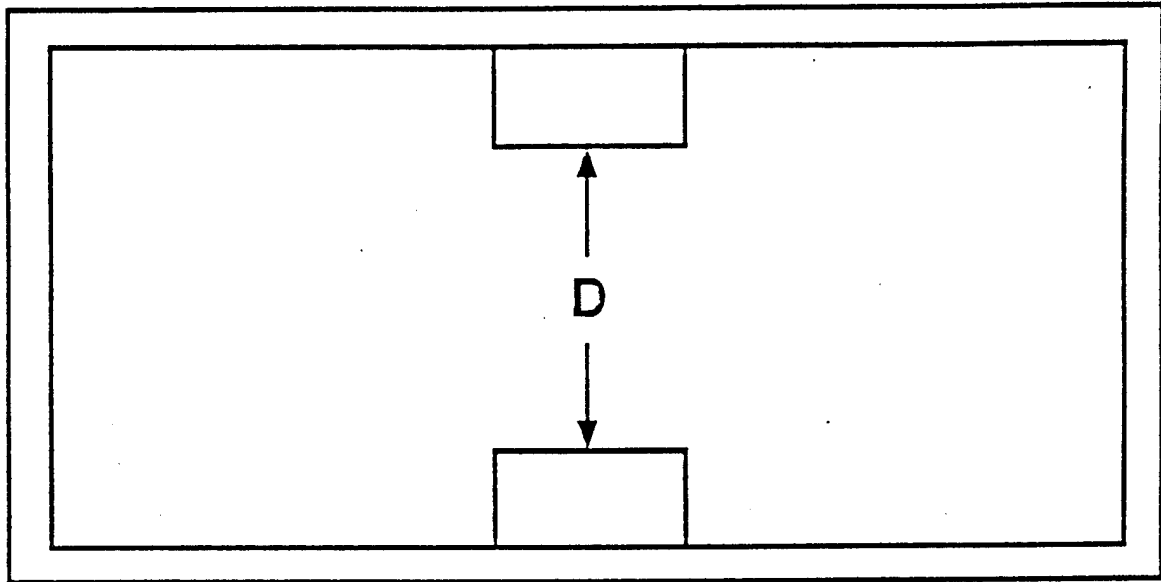
FIGURE VII-16

FIGURE VII-17

150
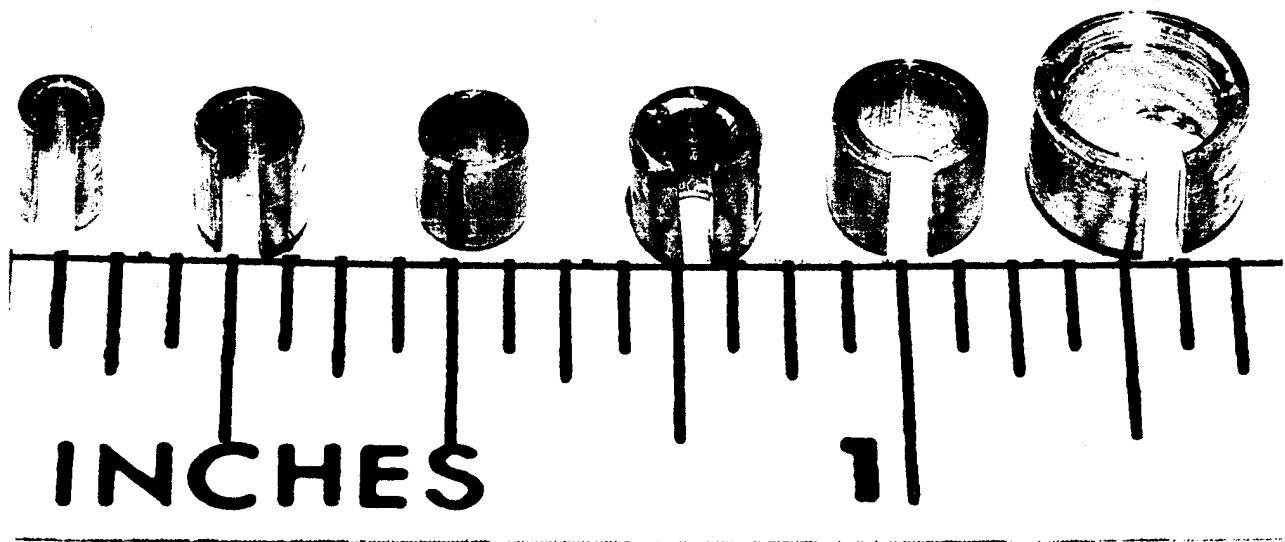
MICROWAVE TEST SET-UP
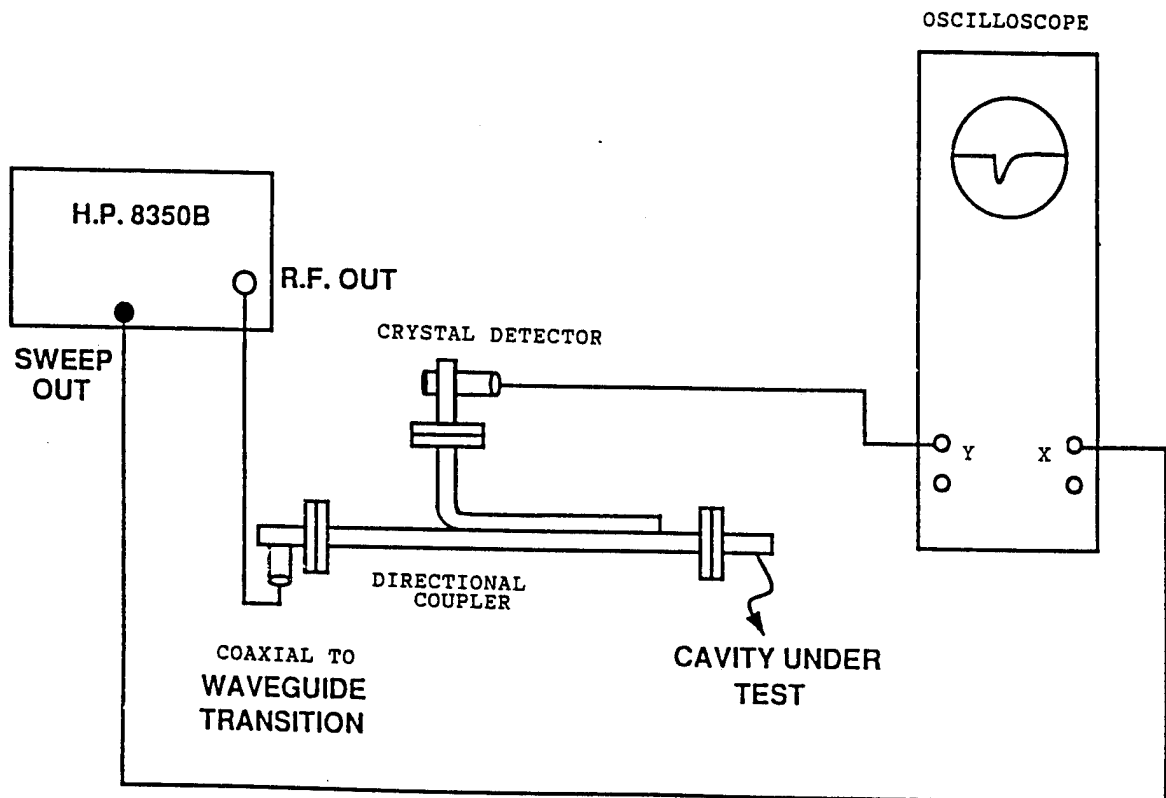
FIGURE VII-18
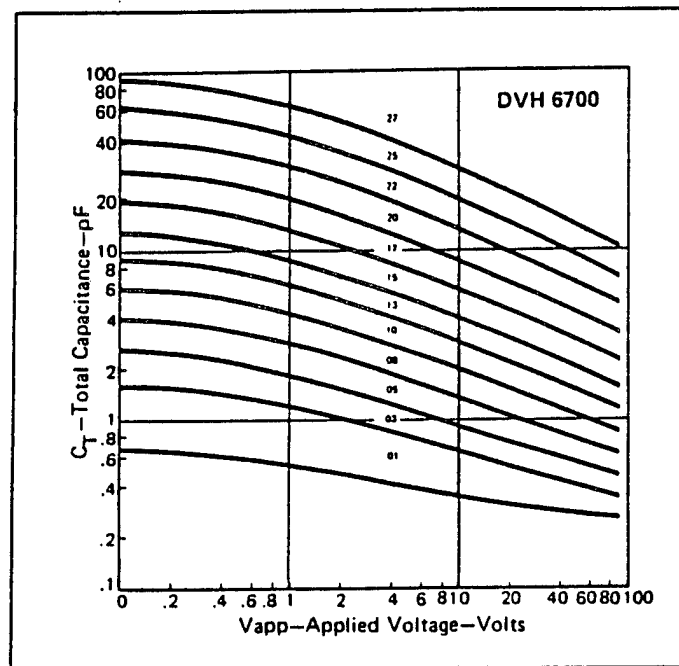
Total Capacitance vs. Applied Voltage

FIGURE VII-19

152

FIGURE VII-20

COPPER RING

CHIPCAPACITOR

LiTaO$_3$ XTAL ⟶

TO BIAS VOLTAGE

FIGURE VII-21

153-A
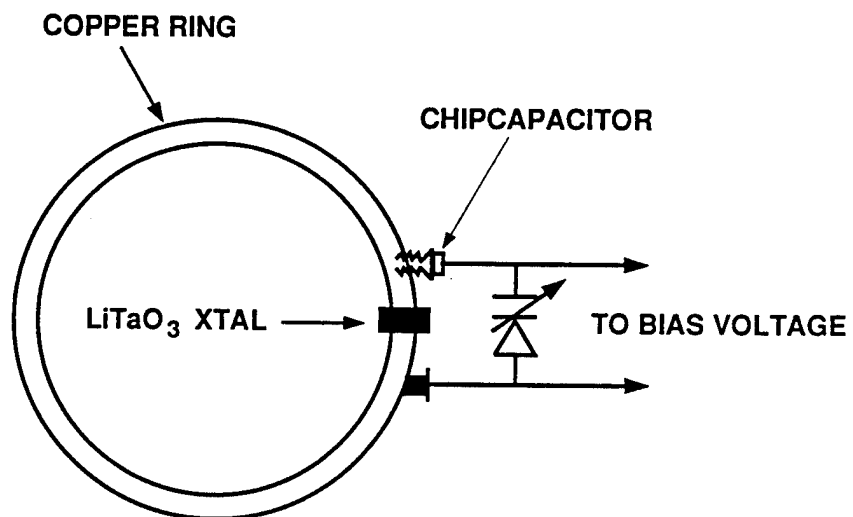
Efforts were devoted to the redesign of the B52 IR Camera video board. The redesign was planned as part of the next phase of the B52 FLIR camera project which is essentially a system shrink of the entire electronics package. The video board has been redesigned to utilize fewer components to improve performance and simplify packaging the board into a smaller space with a new form factor. A special effort was made to have a working prototype completed by the beginning of December (1990) using the current board dimensions (form factor) for implementation in the existing prototype camera. This objective was met, allowing the new video board design to undergo limited environmental testing known as "shake and bake" testing of the entire camera. This testing was to ascertain flight acceptability of the prototype camera and was not the performance environmental testing that will occur in the next phase of the project. The video board successfully completed shake and bake testing. Parts lists were generated and provided to Air Force personnel for the purposes of performing reliability studies where the components on the board are each assigned an estimated reliability based on the rather extensive Air Force database in order to come up with an estimated MTBF (mean time between failure) for the board. Additional support was provided for such parts as were not in the database in order to estimate their reliability.

Involvement with RADC was minimal for a short time which consisted mainly of visiting the facility at Hanscom AFB on a regular basis in order to be available to answer inquiries and solve any problems arising from the operation of the B52 IR Camera video card. Only a few problems arose such as determining the correct gain for the video board in the manual mode of operation. The other problem was related to the video board's interface to another board and turned out to be a problem with the other board.

Other activities included straightening up the laboratory area including bookshelves, and identifying and ordering materials necessary to the next phase of the project.

The period ending June 30, 1991 featured intense activity for RADC. The B52 camera flew successfully although not without some problems. The video board required some component adjustment to optimize the operator control ranges. These adjustments were implemented before the actual flights so that both manual mode and automatic mode for the camera were fully functional at flight time.

Most of the effort was concentrated in the design of a new video board that was all digital with the exception of the output DAC (digital to analog converter). The new board was conceived as a means of facilitating new camera design as well as reducing the size and complexity of camera electronics. The new design consists of a video board and a control box. The video board communicates with the control box via a RS232 (a simple 3-wire serial data link). The control box has the normal camera video controls as well as all the other controls necessary for camera operation. Thus, it can potentially replace the front panel and control board of the camera. This would allow future cameras to consist of one unit containing the sensor array and all other

electronics with camera control performed by the external control box. One nice feature about the design is that the control box function can be replaced by a computer with a serial interface if desired since the interface linking the video board and the control box conforms to a subset of the industry standard (RS232).

An existing camera was selected for modification to incorporate the new design. At this point, usable video is available from the camera. The range and ease of adjustment of the video gain and offset is impressive. Some bugs exist in the operation and should be ironed out with a combination of hardware and software changes.

INTRODUCTION

The thrust of this research effort is the upgrading of electronic devices by changing the basic characteristics of a device in order that it performs in a superior manner. The change made to any device must be easily carried out and the change, whatever it may be, must be such that it can be repeated with little or no variation by qualified laboratory personnel. Otherwise, the program would not be practical, procedurally or scientifically. These changes or upgrading of devices are a prerequisite to the Air Force's requirement of the use of high speed communication.

Initially, the program was based on the deposition of anti-reflective films on side emitting laser diodes, in order to transform it into a superluminescent diode or an optical amplifier. We were attempting to carry out this change by depositing a thin film of silicon dioxide, thereby reducing the reflectance of the emitting facet of the diode to zero and achieving our desired results. There had been quite a bit of basic research carried out in this field of endeavor, and our goal has been to optimize the processes described in the literature.

Scientific papers showed that silicon dioxide was an excellent film to work with, and this film, placed on a laser diode did, in some cases, improve the functioning of the diode. The effort initially was to improve and to standardize the many parameters that are used in the processes of laying down the film, and to establish a scientific procedure that would allow the effective changes required to be carried out in an efficacious manner. All procedures necessary for bringing about the change must be straight forward and easily repeatable with guaranteed results. That is to say, that once a methodology had been established, a competent laboratory worker could carry out the work required with facility and in every case achieve the same results with very slight or no differences.

As regards the equipment used in the procedures, we used equipment that was readily available in the laboratory: an MCR Model SEM 8620 RF Sputter/Etch System (see Figure IX-1) was used to lay down the film on the diode surface. An Alpha Step Model 200 profilometer was used to monitor the consistency of the rate of deposition in conjunction with a Gaertner Elipsometer model L116B, which measured the index of refraction and thickness of the deposited material (see Figure IX-2).

Several factors quickly became clear:

1.   The surface of the diode or surface on which the AR coating was to be deposited had to be very carefully cleaned. (A procedure was established and recorded.)

2.   The chamber pressure before deposition could not exceed 1×10^{-5} Torr.

3.   The chamber pressure during deposition had to be held to a very close tolerance (3 microns). Slight variations (as little as 2 microns) caused unacceptable variations in results (thickness and index of refraction).

4.   The power at which the system was run was crucial, since high power (over 200 watts) overheated the diode and caused it to malfunction. On the other hand, power below 150 watts resulted in poor surface consistency, and erratic refractive indices.

5.   The device on which the deposition was carried out had to be cooled. The emitting surface of the diode in the first few attempts appeared to have received a perfect coating, but the diode itself was rendered useless because of internal structural damage caused by overheating.

6.   In all cases, each step of the final procedure must be carried out precisely as written down.

Once a strict procedure had been settled on, a Hitachi side emitting laser diode, type HLP 1400 was placed into the system and a predetermined coating of silicon dioxide was deposited on the emitting surface. The diode was removed from the system and a measurement made of the coating on the surface. The results seemed to be perfect. However, it was difficult to get a good measurement of the upgraded diode output.

It was finally determined that to make a proper determination of its output, it would have to be placed into a laser diode mount, and using simple optical components a frequency-selective self aligning optical feedback technique has been devised which will allow the diode to be tuned to and scanned about any optical frequency within the laser gain curve. The technique employs a graded-index rod lens cat's eye and an intracavity etalon.

The laser diode mount has been designed and an initial unit has been fabricated (see Figures IX-3 thru IX-15). The measuring system is now in the process of being set up. When completed, it will be used to measure the wideband tuning of modified and unmodified semiconductor lasers.

FIGURE IX-1

FIGURE IX-2

ASSEMBLY DRAWING LASER DIODE MOUNT

COVER PLATE BEAM SPLITTER
HOLDER

BEAM SPLITTER HOLDER

BEAM SPLITTER HOLDER
SPACER

GRIN ROD LENS HOLDER

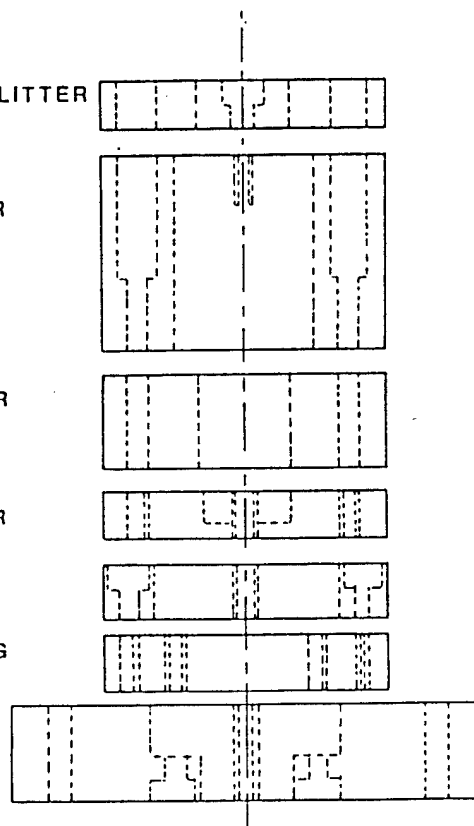SPACER RING

LASER DIODE MOUNTING
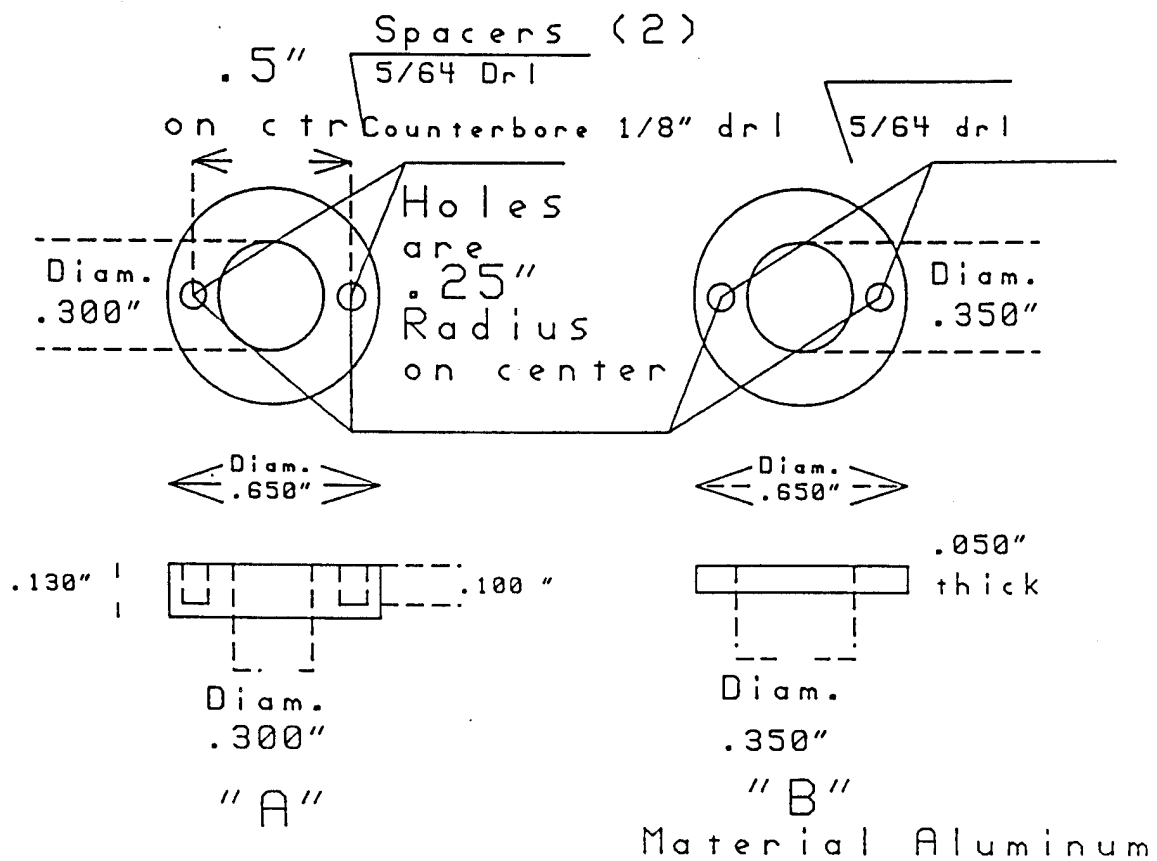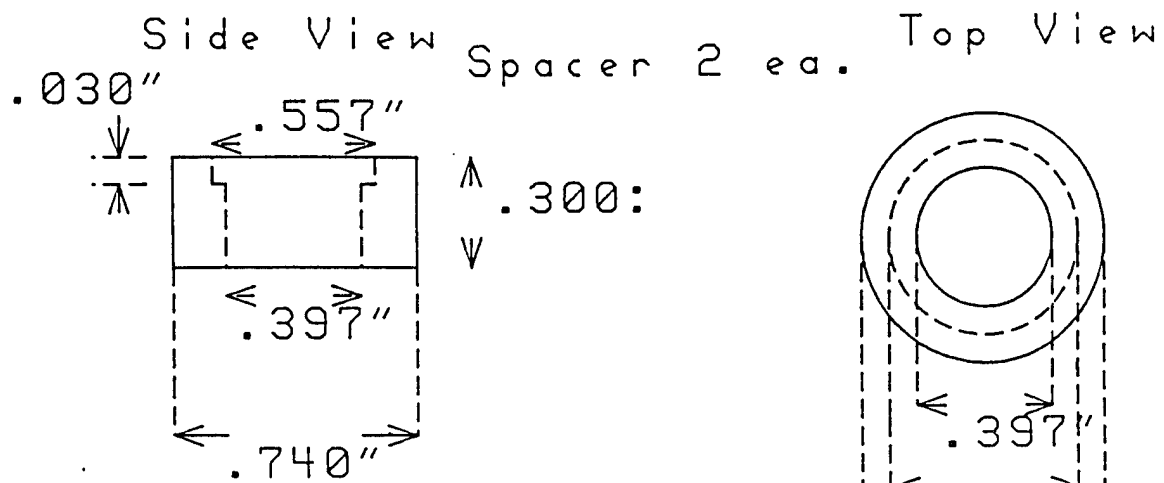PLATE

HEAT SINK

FIGURE IX-3

Spacers (2)

.5"

5/64 Drl

on ctr Counterbore 1/8" drl   5/64 drl

Diam.
.300"

Holes
are
.25"
Radius
on center

Diam.
.350"

Diam.
.650"

Diam.
.650"

.130"

.100"

.050"
thick

Diam.
.300"

Diam.
.350"

"A"

"B"
Material Aluminum

FIGURE IX-4

Side View Spacer 2 ea. Top View

.030"

.557"

.300:

.397"

.740"

Beam Splitter Insert
(2 each)

.397"

.557"

.740"

Material
Aluminum

FIGURE IX-5

162

1.50"

.Cover Plate
 Beam Splitter
 Holder
Holes marked #2
31 CI—counterbore
for #4 Skt Hd Screw

Holes marked #1
use a # 7 drill

1 1/8"

.25"

1 1/8"

All 4 outside holes
are 1 1/8th inch diam.
on center.

1.50"

.25"

Disc = .25 thick

Material
Aluminum

FIGURE IX-6

Beam Splitter Holder

D/T #44 for 4/40 screws

31 Drill

All four
holes are
9/16 " rad.
on center

.563 radius

.750 Dia.

7 Drill

.563 radius

1.5"

Material Aluminum

0.50"

.5"

FIGURE IX-7

Beam Splitter Holder Spacer   Material
Plexiglass

Diam = 1.45"   Diam = 1.45"

.5"   .5"

Holes marked
#1 = .125" diam.

Holes marked #2
= .125" diam. CB .25" for
4/40
Skt
Hd.

1 1/8"

R = .25"

Top View

R = .25"

1 1/8"

Bottom View

FIGURE IX-8

165

Grid Rod Lens Holder   Aluminum
Top View   Bottom View

FIGURE IX-9

Spacer Ring

A

1.50"

D&T 4/40

.625"

counterbore
4-40

1.0"

45

1/8"

D & T 10/32

7/16"

Material
Aluminum

FIGURE IX-10

Spacer Ring

Enlarged View of Outer Flat Section

FIGURE IX-11

Disc is .300" thick

Laser Diode Mounting Plate
Material Aluminum
D&T 2/56"
.8125" on center

.25"
.5"

①

○

③ ○ ③

1 1/8"
on
cntr.

① ○ ② ○ ①

③ ○ ③

○

①

Diam.=1/2" on ctr
center
D&T 2/56"

Disc Diam.=1.5"

Top View

1=D&T 4/40(1 1/8" on
center
2=.25" diam.
3=D&T 4-40(.8125" on
center)

FIGURE IX-12

Heatsink

←——— 2.5 " ———→

All holes are
except center
are drilled
with a #20
drill

1.0 "

.5"

Inner holes
are
3/8" radius

on center
Material
Aluminum

Top View

Outer holes(8) are 1" radius on center

FIGURE IX-13

Heatsink

Outer holes (8) are 1" radius on center.

2.5"

Inner Holes (4) are counterbored bored for 4/40 skt hd screw

.500"

Bottom View

Material Aluminum

FIGURE IX-14

Heat Sink

<1">

All outer holes (8) drl with a # 20 drl.

.5 " thick

.5"

<--- 2.5 "--->

Enlarged
View
Center
Section

Side View

Drl & CB for
4/40 skt hd screw

1.0"

.25"

.25"

<.5" >

Material
Aluminum

FIGURE IX-15

172

Considerable progress was made in streamlining the device fabrication process in the area of semiconductor processing (Si and SiGe) to fabricate infrared detectors using Schottky and HIP technologies. New substrate holders and spin-drying chucks for 2", 3", and 4" wafers were designed and fabricated by the RL machine shop. Use of these new substrate holders, and the spin-drying chuck in the wafer cleaning process resulted in reducing the consumption of chemicals as well as making the process cleaner and faster.

Effort was made to standardize most of the oxidation steps, and to reduce the operating temperature of the furnaces. The furnace idling temperature was reduced to 500°C, and the temperature of most oxidation steps was reduced to 950°C. Lower oxidation temperatures are better for bigger size wafers as well as having less wear and tear on the furnace hardware.

Initially, devices were fabricated on 2" wafers using the "CLD" process and mask sets. In about two years, for the first time a working device (CLD 456) was fabricated on a wafer which was processed in the RL/ERED clean rooms.

A new process using the Reticon mask set was designed. This process was based on the true and proven "CLD" process but with some changes. This new process was designed with three goals in mind. First, it would use the Reticon mask set which was better suited for 3" and 4" wafers. The goal was to eventually change over to the bigger wafers. Second, the new process would do away with the Aluminum Sintering step for contact, but would involve boron implantation for low resistance substrate contact. After the success of this step, a new step would be introduced which would be to have a boron implant in the field areas of high resistivity substrates. A new mask, compatible with the Reticon mask set, for fabricating IrSi diodes was made in-house.

Experiments were also designed to eliminate the first high temperature denuding oxidation step. This was, again, in line with reducing operating temperatures and streamlining the fabrication process. Parallel to the fabrication sequence, collaboration was started with Mr. Leahy who was bringing up the in-house ion implantation machine. Earlier ion implantation was carried out at Spire Corp., but with this thrust, the implantation could be performed in-house, and the ion implanter would be used in future device fabrication. The first success of this collaboration was a successful fabrication of a pn junction on a 2" wafer.

A new set of experiments were designed at this time to study the effect of surface roughness on device properties. KOH solutions were used to roughen the backside of 2" wafers. Both patterned and unpatterned wafers were processed and submitted for Platinum deposition. Preliminary results of these experiments were promising. This work is now being persued by Mr. James Bockman.

173

A major area of thrust at this time was in a joint project between RL/ERE, NRL, and the David Sarnoff Research Center (DSRC). This project involved the development of HIP devices for LWIR detectors. 4" silicon wafers processed (in the front end) by Reticon were used to fabricate the HIP devices. The oxidation area of the clean rooms was not operable at this time because of construction. 3" and 4" wafers which were partially fabricated in RL/ERE clean rooms before the construction had begun, were used for control purposes. Surface preparation and deposition of $Si_{1-x} Ge_x$ layers by MBE was done at NRL. Subsequent processing steps were carried out at RL/ERE.

In order to fabricate these devices, a sputtering process was developed to remove the unwanted $Si_{1-x} Ge_x$ from the non-active areas of the wafer. Argon was used as the sputtering gas. Experiments were designed and carried out to optimize sputtering time, plasma power, and the gas pressure. Particular care had to be taken so that the resist on the wafers (which masks the active areas) was not totally removed during the sputtering step, and secondly, the resist could be removed relatively easily before further processing. It was observed that the sputtering tended to char the resist, and sputtering time/power had to be optimized so that the resist could be easily removed after the sputtering step. These experiments were carried out in close collaboration with Mr. Leahy and Capt. Max Chi.

The final step of this project was to fabricate focal plane arays with HIP devices. 4" wafers with these arrays were processed by the DSRC. Surface preparation and $Si_{1-x} Ge_x$ layer deposition was carried out at NRL. Further sputtering steps were done at RL/ERED. Care had to be taken for the process to be compatible with the further processing steps which would be performed at the DSRC. The project was completed and the wafers were sent to the DSRC for further processing. In the future, an etching process (rather than sputtering) using SF_6 gas will have to be developed for removing unwanted $Si_{1-x} Ge_x$.

The oxidation area of the clean room is now operational. Device fabrication on 2" wafers has been started, and is on-going so as to establish the baseline.

A mask set for device fabrication to be used with a wafer stepper, has also been designed using the Sun Work Stations of RL/ERE.

All of the device measurements were carried out by Ms. Melanie Weeks. Sincere thanks are due to all of the RL/ERE personnel who collaborated in this work.

174

INTRODUCTION

The SiGe alloy system will result in a whole new set of high performance electronic and optoelectronic devices, such as thermoelectric generators, infrared detectors, and high speed optical transmitter recievers. The III-V and II-VI compounds, and silicides have been a major research focus for infrared detectors. A significant shortcoming for III-V and II-VI technologies are the processing and readout interface problems that regularly occur. The silicides such as PtSi and IrSi IR detectors are limited up to 6μm to 12μm wavelength (MWIR). These will not be a problem with SiGe alloys. Si_xGe_{1-x} alloys can be tuned from 2μm to 18μm wavelength (LWIR) depending on the percentage of Ge composition. Their chemical and thermomechanical properties will allow them to be closely compatible with established Si processing technologies, and Si integrated circuits. In the past year, signficant progress was made in fabricating a Heterojunction Internal Photoemission (HIP) Long-Wavelength Infrared (LWIR) detector with 12μm cut-off wavelength. The mask sets were provided by RL/ERE, the $Si_{65}Ge_{35}$ epitaxial layers p+ doped were grown at Naval Research Lab using MBE technique. All other processing steps such as oxidation, photolithography, Plasma sputtering, resist removal, surface cleaning, and Aluminum deposition was done by Parke Mathematical Laboratories' consultants at RL/ERE facilities at Hanscom AFB. The optical testing of the devices was done by Ms Melanie M. Weeks. A focal plane array of $Si_{65}Ge_{35}$ was fabricated in collaboration with the David Sarnoff Research Center and NRL. The results of these focal plane arrays are still not available. In the following sections, the different processing steps are described in detail.

OXIDATION

This critical step was performed by PML's consultants using RL/ERE provided equipment and facilities. The wafers used were 3" diameter Si(10-15 ohms resistivity) purchased from Wacker. A 10,000 $\overset{o}{A}$ thick sacrificial oxide was grown using the "First Dry-Wet-Dry" (FDWD recipe). This oxide layer is etched in 10:1 H_2O:HF solution and wafer is cleaned in RCA 1 (15 minutes) - 50:1, H2O:HF (10 sec.) - RCA 2 (15 minutes) sequence. The wafer is spin dried using a custom designed spinner. A 4,500 $\overset{o}{A}$ thick field oxide was grown using the "Second Dry-Wet-Dry" (SDWD) recipe. This recipe was written by PML consultants. The oxide growth is done at 950°C. The gases used are Hydrogen and Oxygen. Nitrogen gas was used to bring the temperature up from 500°C to 950°C to anneal the field oxide and cool the furnace from 950°C to 500°C. This field oxide acts as a protective insulation as well as an isolation layer. The quality of this oxide will effect the sensitivity and electrical properties of the detector arrays.

PHOTOLITHOGRAPHY

A set of RL/ERE provided masks (RETICON masks) were used to pattern the HIP structure. The guard ring mask was not used due to the fact that the annealing furnace was not available. The active area mask was used to open the active area $(2.56 \times 10^{-3} \, cm^3)$. The $Si_{65}Ge_{35}$ single crystal film is grown on the active area. The metal mask was used to open the area for Al contact deposition. The last mask was used to etch away the excess aluminum.

EPITAXIAL GROWTH OF Si_xGE_{1-x}

The single crystal film of Si_xGe_{1-x} was grown on the active area by the MBE technique. This was done at the Naval Research Laboratory, Washington, DC in collaboration with Dr. Phil Thompson. There were two compositions of Si_xGe_{1-x} layers grown, one with 30% Ge, and the other with 35% Ge. The growth temperature for 35% Ge was 350°C. The layers were doped with 5×10^{19} atoms/cc and 2×10^{20} atom/cc of Boron to make them p^{++} doped. The growth rate of deposition was .3 $\overset{o}{A}$/sec for Si. The thickness of the Si_xGe_{1-x} layer was 100 $\overset{o}{A}$.

PLASMA SPUTTERING

The plasma sputtering of Silicon was devoloped by PML consultants at RL/ERE. The right condition of etching 100 $\overset{o}{A}$ of Si_xGe_{1-x} was developed using Argon plasma and patterned 4"silicon wafers. The etched patterned heights were measured, and it was decided that 150-200W of power for 40 - 80 sec. at 40 - 70 militorr pressure was the most suitable condition. This was done keeping in mind that the resist had to be removed after this step. These conditions were used to pattern the Si_xGe_{1-x} thin films. This area needs to be investigated further, and we propose to use SF_6 reactive ion etch.

PLASMA SPUTTERING

The sputtering process results in hardening of the resist which was difficult to remove in organic solvents. The standard acid removal process (Such as Pirahna clean) was not used since its effect on the Si_xGe_{1-x} layer is not known and needs to be further investigated. The PML consultant developed a tedious process of using Aceton and Proponal in an ultrasound agitator to loosen the resist. This process took a long time to remove the resist. At times, a strong spray of Acetone and Proponal was used to remove hardened resist flakes from the wafer. This area has to be investigated further. The ideal method will be an ashing technique.

METAL DEPOSITION

The Al was deposited using RL/ERE's equipment. A 2,200 $\overset{\circ}{A}$ Al film was deposited.

ACKNOWLEDGEMENT

MISSION

OF

ROME LABORATORY

Mission. The mission of Rome Laboratory is to advance the science and technologies of command, control, communications and intelligence and to transition them into systems to meet customer needs. To achieve this, Rome Lab:

    a. Conducts vigorous research, development and test programs in all applicable technologies;

    b. Transitions technology to current and future systems to improve operational capability, readiness, and supportability;

    c. Provides a full range of technical support to Air Force Materiel Command product centers and other Air Force organizations;

    d. Promotes transfer of technology to the private sector;

    e. Maintains leading edge technological expertise in the areas of surveillance, communications, command and control, intelligence, reliability science, electro-magnetic technology, photonics, signal processing, and computational science.

The thrust areas of technical competence include: Surveillance, Communications, Command and Control, Intelligence, Signal Processing, Computer Science and Technology, Electromagnetic Technology, Photonics and Reliability Sciences.